Analysis and Automation of the crucible-free Floating Zone (FZ) Growth of Silicon Crystals

vorgelegt von
Diplom-Ingenieur
Nico Werner
aus Berlin

der Fakultät III - Prozesswissenschaften -
der Technischen Universität Berlin
zur Erlangung des akademischen Grades

Doktor der Ingenieurwissenschaften
- Dr.-Ing. -

genehmigte Dissertation

Promotionsausschuss:

Vorsitzende: Prof. Dr. Claudia Fleck
Berichter: Prof. Dr. Rudibert King
Berichter: Prof. Dr. Arne Cröll

Tag der wissenschaftlichen Aussprache: 13. Februar 2014

Berlin 2014
D83

Impressum

Verlag: epubli GmbH, Berlin, www.epubli.de
ISBN 978-3-8442-9467-5

Contents

Abstract

Considering the high relevance of electronics in the industrial, technological and business communities, monocrystalline silicon is one of the most important technical materials today and in the near future. To grow the monocrystalline silicon industrially with the required quality, the Czochralski and the crucible-free Floating Zone methods are generally used. The thesis is focused on the model-based automation of the crystal growth of silicon using Floating Zone technique. Automatic growth control is a key issue in production of silicon with respect to yield, quality, and reproducibility. Also, reliability and comparability are enhanced by growth control. In an industrial setting, it is essential to produce crystals with equal properties by keeping identical processing conditions.

In today's industrial production, standard PI or PID controllers are applied to regulate the Floating Zone process. Due to the changing dynamics during the process, the controller parameters are set up separately for every phase of the process. In contrast, a model-based controller gives a widely flexible handling of different machine components, different inductor types and different target diameters. Therefore, a model-based automation concept was developed to regulate the Floating Zone process including the following phases: forming the feed tip, creating the thin neck, making the cone and growing the cylinder. A measurement system was created to obtain the geometrical quantities based on visual image processing. Digital cameras were applied to capture the process. The acquired images were analyzed by gradient-based methods. A model-based state estimation technique, the Extended Kalman filter, and a model predictive controller were implemented to regulate the process without using additional controller components such as a PID controller. To use those methods, a nonlinear low-order model was developed including geometrical and thermodynamical aspects of the process. The mathematical model is based on a system of coupled differential equations and allows the prediction of radii and angles of feed and crystal, upper and lower zone heights, the melt volume, the melt neck, and the rates of melting and growing. A prediction horizon of several minutes is achieved with high accuracy and a calculation time less than one second.

An automation was developed for forming the feed tip to provide reproducible start conditions for the growth of the thin neck. Two regulation strategies were successfully applied for creating the thin neck. The first one used heater power and crystal pull rate, the second one heater power and feed pull rate. The regulated growth beginning from the cone and swinging into the cylindrical phase was realized using references of zone height, diameter and angle of the crystal. Experiments showed a high control precision. With this automation concept, dislocation-free crystals with different diameters were grown on two Floating Zone machines without a renewed parameter identification.

Abstract (in German language)

Angesichts der großen Bedeutung von Elektronik in Industrie-, Technologie- und Wirtschaftsunternehmen, ist einkristallines Silicium eines der wichtigsten technischen Materialien heute und in der nahen Zukunft. In der Regel werden für die industrielle Züchtung von Silicium-Einkristallen zwei Methoden eingesetzt, die Czochralski-Methode und die tiegelfreie Floating-Zone-Methode. Diese Arbeit beschäftigt sich mit der modellbasierten Regelung des Floating-Zone-Verfahrens zur Züchtung von Silicium-Einkristallen. Die geregelte Kristallzüchtung ist ein zentrales Thema in der industriellen Produktion von Silicium in Bezug auf Ertrag, Qualität, Reproduzierbarkeit und Zuverlässigkeit. In der Industrie ist die Gewährleistung von identischen Züchtungsbedingungen endscheidend für die Erzeugung von Kristallen mit gleichen Eigenschaften.

Heutzutage werden in der industriellen Produktion Standard PI- oder PID-Regler eingesetzt, um das Floating-Zone-Verfahren zu regeln. Aufgrund der sich ändernden Dynamik während des Prozesses werden die Reglerparameter für jede Phase separat eingestellt. Eine modellbasierte Regelung ermöglicht u.a. eine weit flexiblere Handhabung der Prozessphasen sowie von unterschiedlichen Maschinenkomponenten und Zieldurchmessern. Daher wurde ein modellbasiertes Regelungskonzept für das Floating-Zone-Verfahren entwickelt. Folgende Phasen wurden dabei berücksichtigt: Formen des Vorlaufs, Ziehen des Dünnhalses, Ausbauen des Kristallkonuses und Ziehen des Zylinders. Ein Messwerterfassungssystem basierend auf einer optischen Bildverarbeitung wurde geschaffen, um die geometrischen Prozessgrößen zu ermitteln. Die von digitalen Kameras bereitgestellten Bilder wurden mittels Gradienten-Methoden ausgewertet. Ein modellbasiertes Verfahren zur Schätzung des Zustands (Extended Kalman-Filter) und eine modell-prädiktive Regelung wurden implementiert. Dabei konnte auf zusätzliche Regelungskomponenten wie beispielsweise PID-Regler verzichtet werden. Um diese Methoden nutzen zu können, war die Entwicklung eines nichtlinearen Modells niedriger Ordnung notwendig, welches die wesentlichen geometrischen und thermodynamischen Aspekte des Prozesses beinhaltet. Das mathematische Modell besteht aus einem System von gekoppelten Differentialgleichungen erster Ordnung und ermöglicht die Vorhersage der Radien und Winkel vom Vorratsstab sowie vom Kristall, der oberen und unteren Zonenhöhen, des Schmelzhalsdurchmessers, des Schmelzvolumens, der Abschmelzrate und der Wachstumsgeschwindigkeit. Ein Prädiktionshorizont von mehreren Minuten mit hoher Genauigkeit konnte erreicht werden mit einer Berechnungszeit von weniger als einer Sekunde.

Eine Regelung zur Erzeugung des Vorlaufs wurde entwickelt. Dadurch könnnen reproduzierbare Startbedingungen für das Ziehen des Dünnhalses realisiert werden. Für die geregelte Züchtung des Dünnhalses wurden zwei Strategien entwickelt und erfolgreich angewendet. Die erste Strategie verwendet

als Stellgrößen die Heizleistung und die Ziehgeschwindigkeit des Kristalls, die zweite, Heizleistung und Ziehgeschwindigkeit des Vorratsstabes. Die geregelte Züchtung des Kristallkonuses und des Einschwingens in die zylindrische Phase wurde durch Vorgaben an Zonenhöhe, Kristallwinkel und -durchmesser realisiert. Durchgeführte Experimente zeigten eine hohe Regelgenauigkeit. Mit dem modellbasierten Regelungskonzept wurden versetzungsfreien Kristalle mit unterschiedlichen Zieldurchmessern auf zwei unterschiedlichen Floating-Zone-Maschinen gezüchtet, ohne erneute Parameteridentifikation.

Nomenclature

List of Symbols - Floating Zone

Symbol	Description
c	Distance between camera and cylinder
D_C	Crystal diameter
D_{cam}	Diameter observed by the camera
D_F	Feed rod diameter
D_N	Melt neck diameter
D_{real}	Real diameter of the cylinder
g	Gravitational acceleration
F_n	Electromagnetic pressure (Laplace-Young equation)
h_m	Melt height
h_C	Lower zone height
h_F	Upper zone height
h_G	Full zone height
h_I	Height of the inductor
H_{bo}	Height of the melt bowl (covered by the crystal surface)
H_C	Distance crystal holder to inductor bottom
H_F	Distance feed holder to inductor top
K	Curvature (Laplace-Young equation)
L_C	Crystal length
L_F	Feed rod length
L_{max}	Maximum zone height
$\dot{m}_F$	Mass change of feed rod with respect to time
$\dot{m}_C$	Mass change of crystal with respect to time
m_{bo}	Mass of the melt bowl (covered by the crystal surface)
m_{fr}	Mass of the visible feed residual
m_{melt}	Mass of the complete melt
m_{vi}	Mass of the visible melt
P_0	Pressure difference (Laplace-Young equation)
P_C	Power introduced in crystal
$P_{C,loss}$	Power dissipation of crystal due to conduction and radiation
$P_{C,crystallize}$	Released power because of crystallization mass flow
P_F	Power introduced in feed rod
$P_{F,loss}$	Power dissipation of feed rod due to conduction and radiation
$P_{F,melting}$	Needed power for melting a feed mass flow
P_{gen}	Generator power

List of Symbols - Floating Zone

Symbol	Description
P_{ind}	Inductor power
$P_{ind,C}$	Inductor power acting on the crystal
$P_{ind,F}$	Inductor power acting on the feed
P_{loss}	Power loss of a solid cylinder due to conduction and radiation
q_0	Latent heat
$Q_{C,crystallize}$	Released heat because of crystallization
$Q_{F,melting}$	Needed heat for melting feed material
R_C	Crystal radius
R_{cam}	Radius observed by the camera
R_F	Feed rod radius
R_N	Melt neck radius
R_{real}	Real radius of the cylinder
T_m	Melting temperature
U_{gen}	Generator voltage
v_C	Crystal pull rate
v_{Cr}	Crystallization rate
$v_{C,max}$	Theoretically maximum of the crystal pull rate
v_F	Feed rod pull rate
v_{Me}	Melting rate
V_{bo}	Volume of the melt bowl (covered by the crystal surface)
V_{fr}	Volume of the visible feed residual
V_{melt}	Volume of the complete melt
V_{vi}	Volume of the visible melt
α	Capillary constant
α_F	Feed rod angle
α_{Si}	Capillary constant of silicon
ϵ	Surface emissivity
κ_C	Reference offset of a diameter
λ_m	Thermal conductivity in the solid at melting temperature
φ_C	Crystal angle
φ_G	Growth angle
φ_M	Melt angle
γ	Surface tension
Ω	Rate of rotation (Laplace-Young equation)

List of Symbols - Floating Zone

Symbol	Description
ρ_M	Melt density
ρ_S	Density of solid material
σ	Stefan-Boltzmann constant
ζ_{lost}	Power loss constant

List of Symbols - Parameter of Floating Zone Model

Symbol	Description
a_0	Polynomial coefficient (V_{bo})
a_1	Polynomial coefficient (V_{bo})
a_2	Polynomial coefficient (V_{bo})
a_3	Polynomial coefficient (V_{bo})
a_{bo}	Fitting factor of $\dot{V}_{bo}$ in derivative of V_{vi}
a_{fr}	Fitting factor of $\dot{V}_{fr}$ in derivative of V_{vi}
a_V	Fitting factor in derivative of melt angle $\dot{\varphi}_M$
a_R	Fitting factor in derivative of melt angle $\dot{\varphi}_M$
a_h	Fitting factor in derivative of melt angle $\dot{\varphi}_M$
a_N	Fitting factor in derivative of melt angle $\dot{\varphi}_M$
b_0	Polynomial coefficient (H_{bo})
b_1	Polynomial coefficient (H_{bo})
c_0	Fitting factor for the power P_C
c_1	Fitting factor for the power P_C
d_0	Polynomial coefficient (V_{fr})
d_1	Polynomial coefficient (V_{fr})
d_2	Polynomial coefficient (V_{fr})
d_3	Polynomial coefficient (V_{fr})
e_F	Fitting factor of the power P_F
e_C	Fitting factor of the power P_C
f_0	Fitting factor of the power P_F
f_1	Fitting factor of the power P_F
K_P	Gain factor of the inductor power P_{ind}
n_h	Fitting factor in derivative of melt neck $\dot{R}_N$
p_F	Fitting factor of the power P_F
p_C	Fitting factor of the power P_C
r_F	Fitting factor of the power P_F
r_C	Fitting factor of the power P_C
τ_P	Time constant of the inductor power P_{ind}

List of Symbols - Control Techniques

Symbol	Description	Dimension
e	Control error	scalar
e_p	Prediction error	scalar
$\underline{f}$	Model function (State Space Model)	n
g_i	Inequality constraint (Optimization)	scalar
h_i	Equality constraint (Optimization)	scalar
$\underline{h}$	Model output function (State Space Model)	q
H_p	Prediction horizon (NMPC)	scalar
H_u	Control horizon (NMPC)	scalar
J	Objective function (Optimization and NMPC)	scalar
J_{QR}	Objective function (Kalman parameter identification)	scalar
J_Θ	Objective function (model parameter identification)	scalar
k	Sample time point	scalar
K_d	Derivative gain (PID)	scalar
K_i	Integral gain (PID)	scalar
K_p	Proportional (PID)	scalar
n	Number of system states	scalar
n_{mp}	Number of model parameter	scalar
n_ϕ	Number of design variables (Optimization)	scalar
p	Number of control inputs	scalar
q	Number of system measurements	scalar
t	Time	scalar
t_c	Control point (NMPC)	scalar
$\underline{u}$	System input vector	p
$\boldsymbol{W_b}$	Weight state boundaries (NMPC)	$n \times n$
$\boldsymbol{W_s}$	Weight final control error (NMPC)	$n \times n$
$\boldsymbol{W_u}$	Weight control input (NMPC)	$p \times p$
$\boldsymbol{W}_{QR}$	Weight (Kalman parameter identification)	$q \times q$
$\boldsymbol{W_x}$	Weight control error (NMPC)	$n \times n$
$\boldsymbol{W}_\Theta$	Weight (model parameter identification)	$q \times q$
$\underline{x}$	System state vector	n
$\underline{y}$	System measurement vector	q
$\underline{\Theta}$	Model parameter vector	n_{mp}
$\underline{\phi}$	Design vector (Optimization)	n_ϕ
$\underline{\phi}_{lb}$	Lower bound of the design vector (Optimization)	n_ϕ
$\underline{\phi}_{ub}$	Upper bound of the design vector (Optimization)	n_ϕ
$\underline{\phi}_{opt}$	Optimal design vector (Optimization)	n_ϕ

List of Abbreviations

Abbreviation	Description
CZ	Czochralski
EKF	Extended Kalman filter
EM	Electromagnetic
FZ	Floating Zone
IGBT	Insulated-Gate Bipolar Transistors
LPS	Lateral-Photovoltage-Scannings
MEMS	Micro Electromechanical Systems
MIMO	Multiple Input Multiple Output
MOSFET	Metal Oxide Semiconductor Field-Effect Transistor
MPC	Model Predictive Control
NMPC	Nonlinear Model Predictive Control
PERL	Passivated Emitter, Rear Locally diffused
PI	Proportional-Integral
PID	Proportional-Integral-Derivative
RF	Radio frequency
SISO	Single Input Single Output
WLS	Weighted-Least-Squares

1. Introduction

Electronic devices such as computers, notebooks and smart phones are integral components of every day life, and a world without electronics is nearly unimaginable. Considering the high relevance of electronics in the industrial, technological and business communities, monocrystalline silicon is one of the most important technical materials today and in the near future. Approximately 99% of all semiconductor devices are made from monocrystalline silicon (see Zulehner [Zul00]).

For the growth of monocrystalline silicon, the polycrystalline raw material is melted first and then crystallized in a monocrystalline structure afterwards. The crystal orientation is determined by the seed monocrystal[1]. To grow the monocrystalline silicon industrially with the required quality, the Czochralski (CZ) and the Floating Zone (FZ) methods are generally used.

Approximately 95% of the monocrystalline silicon manufactured today is obtained using the CZ method (see Zulehner [Zul00]). The crystals are used for manufacturing highly integrated low-power devices in the field of microelectronics such as computer components. For the CZ method, polycrystalline silicon is molten in a crucible. The monocrystalline seed is dipped into the melt and slowly pulled upwards while simultaneously being rotated. The crystallizing material grows in the same structural orientation as preset by the seed crystal. To avoid dislocations (disorders in the monocrystalline structure) the crystal needs to be started with a thin neck in the range of 2-3 millimeters in diameter, where all dislocations generated when dipping the seed into the melt grow out (see Dash [Das59]). After the thin neck is dislocation-free, the crystal can be increased in diameter. The process is primarily controlled by heater power, crystal pull velocity, crucible rotation and crystal rotation. The high melting temperature of silicon (1687 Kelvin) requires a crucible made of an appropriate temperature-resistant material. Usually the crucible is made of silicon dioxide, the so-called quartz. But, because of the high melting temperature, the melt is contaminated by the crucible material, for instance by oxygen. This affects the purity of the crystals (see Duffar [Duf10], chap. 3).

High-power electronics require a high level of material purity, which cannot be obtained by CZ crystals. The crucible-free FZ method was invented to avoid the contamination of the melt. Therefore, the highest purity of silicon crystals grown from the melt can be achieved by the FZ technique. Here, a solid polycrystalline silicon feed rod is the material source which is gradually molten and then crystallized as a monocrystal. The liquid region between the polycrystalline and the monocrystalline part is called the molten zone generated by a contactless heating. In practice, the polycrystalline feed rod

[1] The seed is an approximately 4-7 mm thick and 5-10 cm long monocrystal manufactured from a larger crystal in the desired orientation.

is pulled down and molten by the heater. In industrial production, a radio frequency coil is used for heating and melting the feed material. The FZ process is initiated by forming a molten drop of silicon at the tip of the feed rod. A monocrystalline seed is slowly moved upwards to the drop and dipped into it. As for CZ also in FZ, a thin neck is grown for eliminating dislocations. Below the heater, the melt crystallizes, always having the molten zone on top. A detailed description of the FZ process is found in section 3.1 of this thesis.

FZ silicon is used to produce power devices, photo detectors, digital signal processors, memory chips and solar cells. Examples are Power MOSFETs (Metal Oxide Semiconductor Field-Effect Transistors), IGBTs (Insulated-Gate Bipolar Transistors) in variable frequency drives, MEMS (Micro Electromechanical Systems) and high power thyristors. For solar cells based on monocrystalline silicon, the current record of 24.7% efficiency is held by the PERL (Passivated Emitter, Rear Locally diffused) solar cell, which is made out of FZ wafers. The PERL solar cell was developed at the University of New South Wales (see Zhao et al. [Zha01a] and [Zha01b]). Today, research projects investigate the growth of FZ silicon with quadratic shape, to reduce costs and waste of material while producing solar cells (see Rost et al. [Ros12], Riemann and Lüdge [Rie09]).

Here, a short overview of the advantages and disadvantages of the FZ method is given. The FZ process offers the following advantages over the CZ method:

- FZ crystals have the highest purity. The oxygen concentration of FZ silicon crystals (approximately 10^{16} cm^{-3}) is two orders of magnitude smaller compared to that of CZ material. The content of carbon, heavy metals, alkali and alkaline earth metals is also lower.
- FZ silicon has a better axial homogeneity of the specific resistivity.
- The FZ process has the potential for higher growth rates than CZ due to the relatively high temperature gradient at the crystallization front (typically 2-4 mm/min for FZ, 1-2 mm/min for CZ).

Disadvantages of the FZ process are:

- The maximal achievable crystal diameter in the production is lower (today 200 mm for FZ, 300 mm for CZ).
- The feed material has to be in a cylindrical shape.
- The FZ machine is mechanically sophisticated. To operate it, more experience and skills are needed. Therefore, growing FZ crystals is more expensive compared to growing crystals from a crucible such as for the CZ process.

The FZ process is attempted to be made automatic to reduce the operating requirements and to increase the yield in the industrial production. This finally results in lower production costs for FZ crystals. Standard linear PI (Proportional-Integral) or PID (Proportional-Integral-Derivative) controllers

are applied to regulate the FZ process. However, the linear concept is limited when it is applied to the nonlinear dynamics of the FZ process. To overcome these limits, a nonlinear model can be used to control the process. The development and the implementation of an automation concept based on a nonlinear model is the focus of this thesis.

1.1. Motivation of Process Automation

The main target of the automation is to increase the yield of dislocation-free monocrystals. Nowadays, silicon crystals of up to 200 mm in diameter are grown in the modern industrial FZ production. Growing these crystals is a complex process. Even for experienced operators, it is difficult to keep the small window of suitable growth conditions by manual growth. To obtain the desired crystal properties, the operator has to be supported by automation. It allows for faster and more accurate reaction on changing processing conditions and occurring disturbances, respectively. Automatic growth control is a key issue in production of monocrystalline silicon with respect to yield, quality, and reproducibility. Also, reliability and comparability are enhanced by growth control. In an industrial setting, it is essential to produce crystals with equal properties by keeping identical processing conditions. For research issues, it is necessary to compare growth experiments with different setups (for instance different inductors or reflectors). The automation creates identical process conditions, so that the observed behavior of the modified setup is more precise. A further advantage of an automated process, especially in industrial production, is the possibility of a parallel handling of several FZ-machines by one operator.

In today's industrial production, standard PI or PID controllers are applied to regulate the FZ process. The controller parameters are set up based on empirical data. This has to be done separately for each setup in every phase of the process due to the changing dynamics during the process. Such an automation achieves good results according to the identical processing environment. If the environment of the process is modified (new machine components, new crystal diameter), then the PID controller has to be set up again. This is expensive, especially in research issues, where the environment often changes. To handle these requirements, an automation concept based on a mathematical model yields better results. A model-based controller gives a widely flexible handling of different machine components, different inductor types and different target diameters. Also, the changing dynamics of the process can be directly handled by model-based automation on condition that a suitable mathematical model is available.

1.2. Objective of the Thesis

The main objective of the current work is the development of a model-based automation for the FZ process including the phases - forming the feed tip,

creating the thin neck, making the cone and growing the cylinder (see figure 3.1, page 34). The top priority is the growth of dislocation-free monocrystalline silicon. The regulation concept has to be applicable for different crystal diameters and different FZ machines. The thesis is focused on dynamic process modeling and the identification of suitable trajectories for a stable process control. A model of the complete process is required, that is suitable for controlling in real-time (during the entire growth process). For implementing the control methods, corresponding computer programs were created.

The objectives of the current work include:

- Measurement system:

  It is obvious that measurements are needed for a control system. These measurements are the base for all calculations of the controller. A goal of this thesis is the development of a measurement system based on visual image processing.

- Mathematical model:

  Modeling the process dynamics includes the identification of the relevant process variables, equation formulation and parameter identification. This non-stationary model is the basis for the model-based feedback control and valid for all phases of the process.

- Trajectory planning:

  The detection of reference values is an important task to stabilize the process. Therefore, the processing phases are analyzed with a focus on suitable trajectories and the process limitations.

- Model-based control:

  The implementation of a model-based feedback control requires a state observer, because not all model variables are directly measureable. In this thesis a Kalman filter is used to estimate these variables. The control system - including measurement system, state observer and feedback controller - is installed in different FZ machines and applied for different crystal diameters.

1.3. Related Work

The work of Zulehner [Zul00] gives a historical overview of the evolution of the modern growth techniques for silicon monocrystals, starting from the growth of small germanium crystals in the 1950s to large-diameter silicon crystals today. A detailed description of the inductively heated FZ process can be found in the review by Lüdge et al. [Lüd10].

The first investigations for controlled growth of silicon started at the end of the 1950s for the CZ process. Levinson used a weight measurement of the crucible or the growing crystal to control the heater power (see Levinson [Lev59]).

Current works approach the control task by modern model-based feedback control of the CZ process. A detailed investigation is presented in the works of Winkler and Neubert in the review "Nonlinear Model-Based Control of the Czochralski" (see Winkler et al. [Win10a], [Win10b] and [Neu12]). The idea of that approach is to use a combination of model-based feedforward calculation and conventional linear PI controllers for controlling crystal diameter and growth rate. That method measures the weight of the growing crystal and uses a nonlinear state observer for the reconstruction of crystal diameter, slope angle, and growth rate from the weighing signal.

At the end of the 1980s, Shin-Etu Handotai published patents to grow FZ crystals by standard PI or PID control or a variation of them (see Ikeda et al. [Ike87], Watanabe et al. [Wat88], Taguchi and Watanabe [Tag88]). Reference values are the crystal diameter and the axial height of the molten zone. The process is monitored with an imaging device (for instance a video camera), and geometric quantities (diameter and zone height) are measured from the obtained images.

In the year 1996, the German company Wacker Siltronic AG published an idea to control growth processes, for instance CZ and FZ, by a prediction control method (see Dornberger et al. [Dor96] and [Dor97]). The patents include establishing an on-line simulation software working with a reduced number of variables and the reduction of variables being performed by using a projection algorithm. To speed up the time-consuming on-line simulation, a data bank should be generated, in which values of precalculated variables were stored. A control loop should be established to control the process in real time using the accelerated on-line simulation software as an on-line observer. The patents do not provide a model description, they include only the idea of predictive control by using on-line and off-line simulation.

Satunkin gives an approach to model the CZ and FZ process dynamics in his review [Sat10]. For the CZ process, problems of digital filtering of the measurement noise based on Kalman filters and the determination of mechanical stability limits are considered briefly. The given linear FZ model is developed for growing small-diameter crystals. Due to the complex dynamics, it is necessary to use a nonlinear model for controlling the crystal growth of large-diameter crystals according to industrial-scale production.

2. Control Theory

This chapter gives an overview of methods and techniques applied to control the FZ process. The principle of an important tool, the mathematical optimization, is introduced. Furthermore, the components of a modern feedback control loop such as state estimator and feedback controller are discussed. The components are described according to their general tasks on the one hand and their functionality on the other hand. Descriptions of the primary loop components, the model predictive controller and the Kalman filter are given at the end of this chapter.

2.1. Mathematical Optimization

The mathematical optimization plays a fundamental role in this thesis. It is essential in the calculations within the model predictive controller and it is applied in many fields such as processing of measured data, identification of the model parameters, and the automatic setting of the Kalman filter. It is needed to use numerical optimization algorithms due to the nonlinear structure of the problems.

An optimization problem consists of maximizing or minimizing a criterion by varying values of the input variables based on a mathematical strategy. In other words, optimization is a selection of the "best available" values with regards to a criterion. The criterion is called *objective function* J which is a scalar function depending on the *design vector* $\underline{\phi}$ consisting of n_ϕ components, the so-called *design variables*. The design variables can be directly limited concerning upper and lower bounds. Sophisticated optimization algorithm consider further limitations such as additional equality and inequality constraints involving, for example, the states of the system as well.

The standard form of a (continuous) optimization problem is

$$\begin{aligned}
\underline{\phi}_{opt} = \arg\min_{\underline{\phi}} \; & J(\underline{\phi}) \qquad \text{subject to} \\
& \underline{\phi}_{lb} \leq \underline{\phi} \leq \underline{\phi}_{ub} \\
& g_i(\underline{\phi}) \leq 0, \; i = 1, \ldots, \text{number of additional inequality constraints} \\
& h_i(\underline{\phi}) = 0, \; i = 1, \ldots, \text{number of equality constraints}
\end{aligned}$$

where $\underline{\phi}_{opt}$ is the optimal design vector, J the scalar objective function, $\underline{\phi}_{lb}$ the lower bound of the design vector, $\underline{\phi}_{ub}$ the upper bound of the design vector, g_i an inequality constraint, and h_i an equality constraint. The minimal value of the objective function is $J_{opt} = J(\underline{\phi}_{opt})$.

Figure 2.1 shows the principle of an iterative optimization method. The iteration starts with an initial value of the design vector $\underline{\phi}_0$ and the calculation

of the objective value $J(\underline{\phi}_0)$. If the termination criterion is not fulfilled, the current design vector $\underline{\phi}$ is adjusted by a mathematical strategy, and a new iteration step starts by calculating the corresponding objective value J. The optimization terminates if the convergence criterion is fulfilled.

Within the model predictive controller, the C++ open source package Ipopt (Interior Point OPTimizer) Ver 7 is applied in the control software of the FZ process. Ipopt is usable for large-scale[1] nonlinear optimization and implements an interior-point[2] line-search filter method. The algorithm code was written by Wächter and Biegler and mathematical details can be found in the reviews [Wäc02] and [Wäc06].

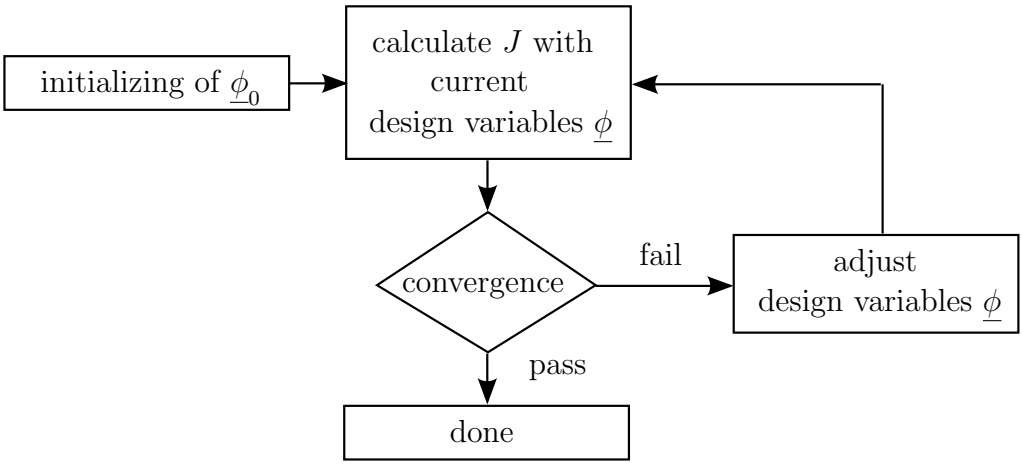

Figure 2.1.: Principle of an iterative optimization method

2.2. Components of the Control System

Figure 2.2 shows a sketch of a modern control system consisting of a generator for reference trajectories, the feedforward and feedback controllers, the regulated plant and the state estimator. The reference values (such as crystal diameter and zone height) are calculated by the trajectory generator depending on time, crystal length and/or estimated process values (such as crystal diameter). The reference trajectories can be constant set points or permanently changing.

In general, the process values consist of measurable and not directly measurable quantities. The state estimator provides a reconstruction of the process values: the estimated system state vector $\underline{\hat{x}}$. That is possible if a suitable system model

[1] large-scale means that the numbers of design variables and/or equality and inequality constraints are large.

[2] interior-point is a method to handle inequality constraints. It is an alternative to active set strategies. A detailed description is given in the review of Wächter and Biegler [Wäc06].

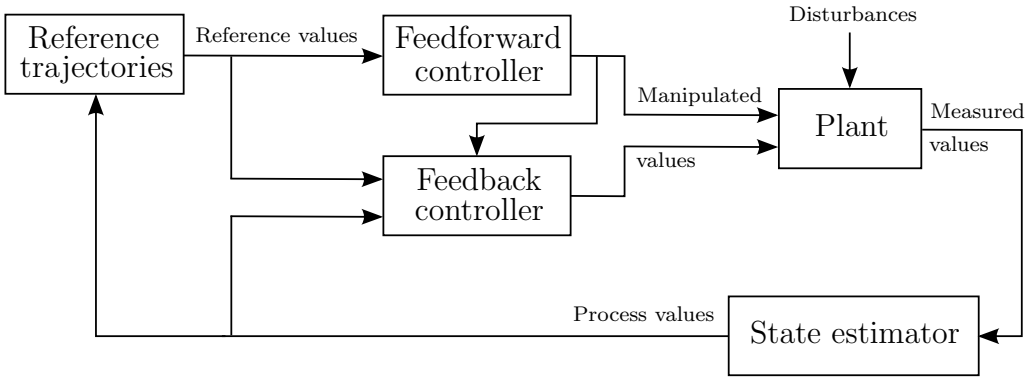

Figure 2.2.: Sketch of a modern feedback control loop consisting of a generator for reference trajectories, feedforward and feedback controllers, regulated plant and state estimator for reconstructing of the process values.

is available and observable[3]. The estimator uses a model-based estimation scheme such as Luenberger observer or Kalman filter technique. In the FZ process the melting rate v_{Me} and the crystallization rate v_{Cr} are not directly measurable, but observable due to a mathematical model describing the system behavior.

The feedforward controller calculates the manipulated values from the reference values provided by the trajectory generator. This can be done empirically (from experience of growth experiments) or by means of a mathematical model (for instance using the equation of the stationary mass balance). Disturbances, acting on the plant, are not considered by the feedforward control. For a stable system and small disturbances, it is possible to steer the system along its reference trajectory by a feedforward control only if the model is accurate enough. Feedforward controlling can include other input quantities (such as rotation and pull rate of the crystal) compared to the feedback controller.

The feedback controller compensates for the control error e, which is the difference between the measured values (or observed process values) and the reference values. This is achieved by a feedback loop of the observed process values. Despite using a feedforward controller, a control difference arises because of model inaccuracies and disturbances. Unstable systems are stabilized by the feedback controller.

Simple systems are often successfully controlled by standard PID controllers. Systems with complex dynamic characteristics, for instance large time delays and high-order dynamics, are difficult to control by PID controllers.

[3] Details of validating the observability of system states are given in the reviews of Simon [Sim06] and Heine [Hei04]

2.3. Feedback Controller: PID

Figure 2.3 shows a sketch of the control loop using a PID controller as feedback component. A PID is the most commonly used feedback controller in industrial control systems. The controller attempts to reduce the control error e by adjusting the manipulated value. The error e is the difference between a measured value (or observed process value) and a desired reference value. The PID controller involves three terms which can be interpreted in terms of time:

- the proportional term (p) depends on the present error,
- the integral term (i) is an accumulation of past errors,
- the derivative term (d) is a prediction of future errors based on the current rate of change.

The weighted sum of these three terms is used to adjust the process. Generally, the sum of feedforward and PID controller is sent out into the plant. A formulation of a PID controller is given by equation 2.1,

$$u(t) = \underbrace{K_p e(t)}_{p} + \underbrace{K_i \int_0^t e(\tau)\,\mathrm{d}\tau}_{i} + \underbrace{K_d \frac{d}{dt} e(t)}_{d} \tag{2.1}$$

with the manipulated variable $u(t)$, the control error $e(t)$ and the gain factors K_p, K_i and K_d.

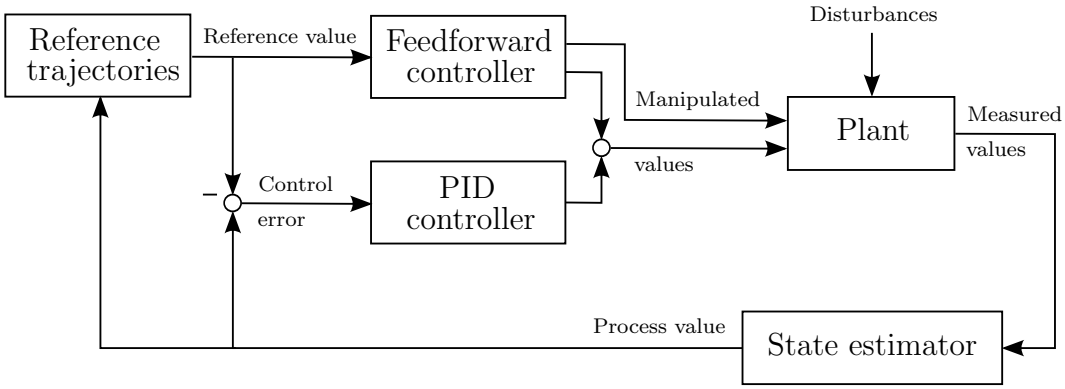

Figure 2.3.: Sketch of a feedback control loop using a PID controller as feedback component

The PID controller is linear and has to be adjusted for a certain operating point of the process. The implementation is easy and can be adjusted using simple rules. For changing operating points (as it is the case for the generator power considering all phases of the FZ process), the parameters may have to be scheduled by tuning rules (for instance empirical methods). Thus, a poor control performance could result from this method.

2.4. Feedback Controller: Model-Based Control

In this thesis, a model-based controller is applied as the feedback component (see figure 2.2, page 20). The controller uses a mathematical model and can reflect the nonlinear system characteristics. Therefore, the controller is suitable for a wide range of operating points and the parametrization effort is reduced compared to PID parameter scheduling.

To regulate the FZ process, the model-based controller uses the observed process values as well as the manipulated values calculated by the feedforward control.

2.4.1. System Model

A model is a representation of fundamental aspects of a system in a mathematical form. Modeling of a system consists of two parts - the identification of the structure and the identification of the unknown parameters. A high model quality is reached if the model is built from physical, chemical or biological fundamental equations, for instance, the balance equations and the conservations laws. If this is too sophisticated or time-consuming, the behavior can be described as a black-box without the knowledge of the physical relations therein. It is necessary to keep the model as simple as possible to be able to use common computer hardware and to ensure robust applicability for multiple plants without recurring parameter identification.

In the model-based control of dynamic systems, a state space model can be used (see figure 2.4). The inputs, outputs and states are expressed as vectors. The system state vector $\underline{x}(t)$ represents the entire state of the system at any given time point. The system output $\underline{y}(t)$ includes the measurable quantities. For a given initial state $\underline{x}_0$ and a given sequence of inputs $\underline{u}(t)$, the future development of the state vector $\underline{x}(t)$ and output vector $\underline{y}(t)$ can be calculated based on the model equations.

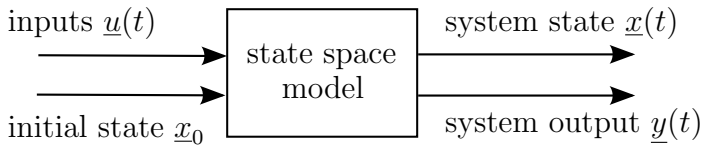

Figure 2.4.: Sketch of a state space model

In this thesis, a nonlinear state space model

$$\dot{\underline{x}}(t) = \underline{f}(t, \underline{x}(t), \underline{u}(t), \underline{\Theta}) \quad \text{with } \underline{x}(0) = \underline{x}_0, \tag{2.2}$$

$$\underline{y}(t) = \underline{h}(t, \underline{x}(t), \underline{u}(t), \underline{\Theta}) \tag{2.3}$$

is used. The model is a system of coupled differential equations of first order. The time derivative $\underline{\dot{x}}(t)$ of the state vector is given by the model function $\underline{f}$. The output function $\underline{h}$ provides equations to calculate the system output $\underline{y}(t)$. The model function $\underline{f}$ and the output function $\underline{h}$ can depend on time t, state vector $\underline{x}(t)$, input vector $\underline{u}(t)$ and model parameter vector $\underline{\Theta}$. The future development of the state vector $\underline{x}(t)$ can be calculated by using a numerical integration method (for instance Runge-Kutta of 4th order).

2.4.2. Designing a Model-Based Feedback Controller

Figure 2.5 shows the working steps to implement a model-based feedback controller. A full model consists of the *model structure* (a set of equations) and the *model parameters* (factors included in the model structure). At first the *model structure* has to be derived to generate a process description in a mathematical way. Algebraic and differential equations can be used for time-discrete or time-continuous systems in linear or nonlinear form. The *model parameters* have to be obtained in a second step. Therefore, available measurements of several experiments are divided into *training data* and *test data*. The training data is used for the direct identification, while the test data allows for a cross-validation of the full model. The number of model parameters defines the degree of freedom for fitting the model to the real process.

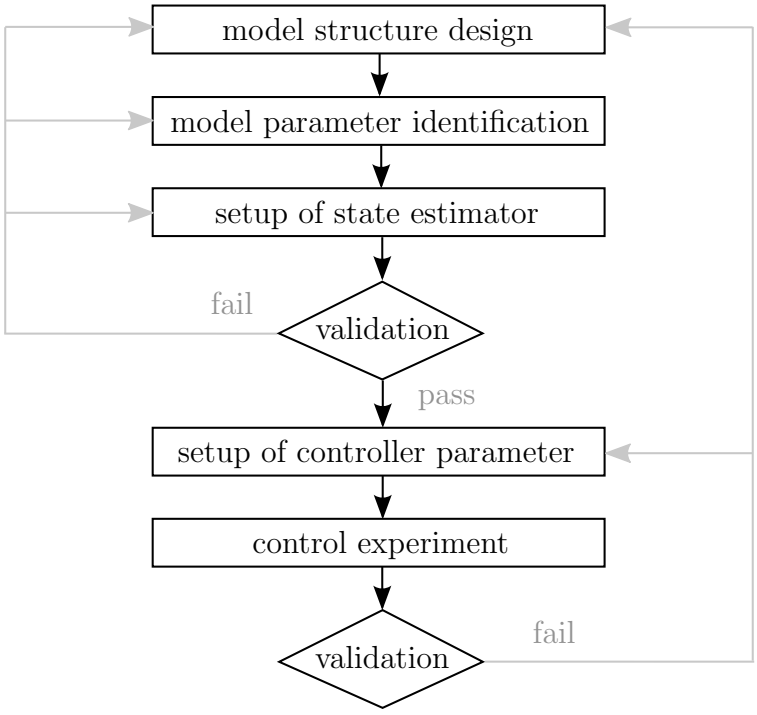

Figure 2.5.: Task sequence to design and apply a model-based feedback controller on a plant

If one or more process values are not directly measurable, a state estimation technique (such as Luenberger observer or Kalman filter) has to be used. The state estimator is configured in the step *setup of state estimator*. In *validation*, the result of the previous steps are experimentally verified by using already recorded measurements. This step is needed to ensure the quality of the full model (including structure and parameters) and the state estimation. After a successful validation, the controller can be configured (*setup of controller parameter*) to run a *control experiment* afterwards. The experimental data is used to re-design the model or controller to improve the control quality.

2.4.3. Parameter Identification

In issues of model-based automation, the control quality is directly coupled to the model quality, especially to the prediction accuracy. To achieve predictions, as precise as possible, complex system descriptions can be used involving complex parameter settings. If a number of model parameter cannot be estimated explicitly using physical laws or relations, a technique based on comparing measurements with model simulation can be used to identify these parameters.

The task of the parameter identification is the estimation of the model parameter $\underline{\Theta}$ to achieve a high conformity between measurements and model predictions. First, it is essential to involve different experiments simultaneously (*training data*) to get a representative prediction of the process. Second, the conformity has to be validated using experiments (*test data*) which are not involved in the identification process.

The weighted-least-squares (WLS) technique is commonly used for parameter identification. The objective function J_Θ

$$J_\Theta(\underline{\Theta}) = \sum_{k=1}^{N} \left[\underline{y}_k^{meas} - \underline{y}(\underline{x}_0, \underline{u}_k, \underline{\Theta}, t_k)\right]^T \boldsymbol{W}_\Theta \left[\underline{y}_k^{meas} - \underline{y}(\underline{x}_0, \underline{u}_k, \underline{\Theta}, t_k)\right] \quad (2.4)$$

is used, where $\underline{y}(\underline{x}_0, \underline{u}_k, \underline{\Theta}, t_k)$ is the calculated model prediction of the system output at time point $t = t_k$. The prediction is characterized by the initial state $\underline{x}_0$ at $t = t_0$, the input values $\underline{u}_k$, and the model parameter $\underline{\Theta}$. The vector $\underline{y}_k^{meas}$ is the measurement vector at $t = t_k$ and N the number of sample points of measurement. $\boldsymbol{W}_\Theta$ is used to weight the influence of the corresponding terms (such as zone height or crystal angle) and to handle the magnitudes due to the different physical units.

An optimization algorithm varies the model parameter $\underline{\Theta}$ starting from the initial value $\underline{\Theta}_0$ to minimize the objective function J_Θ. Section A.4.2 in the appendix gives the used weight matrix $\boldsymbol{W}_\Theta$ for the FZ process and section A.6.1 and A.6.2 the obtained model parameter $\underline{\Theta}$.

2.4.4. Nonlinear Model Predictive Control

Nonlinear Model Predictive Control (NMPC) is a modern method of process control that has been used in industry since the 1980s. The practical interest is driven by increasing requirements of process conditions and performance. At the same time more and more constraints need to be satisfied (see Findeisen and Allgöwer [Fin02]). Today, efficient algorithms and performant computers are available to solve the computational tasks to regulate linear or nonlinear systems by predictive control.

Figure 2.6 shows a scheme of the NMPC. Based on the model the controller predicts the development of the future system state and output involving the control inputs of the future. This sequence of control inputs is calculated to bring or keep system state $\underline{x}(t)$ and/or output $\underline{y}(t)$ close to the references while honoring constraints on system state $\underline{x}(t)$, system output $\underline{y}(t)$, and control inputs $\underline{u}(t)$. Therefore, a numerical method minimizes the scalar *objective function* J (sometimes called cost function) taking into account constraints on $\underline{x}$, $\underline{y}$, and $\underline{u}$. The sequence of control inputs resulting in a minimal objective function represents the optimal solution. The system state at the current time point, the reference trajectories, the process limitations, and the system model are required to calculate the optimal control input.

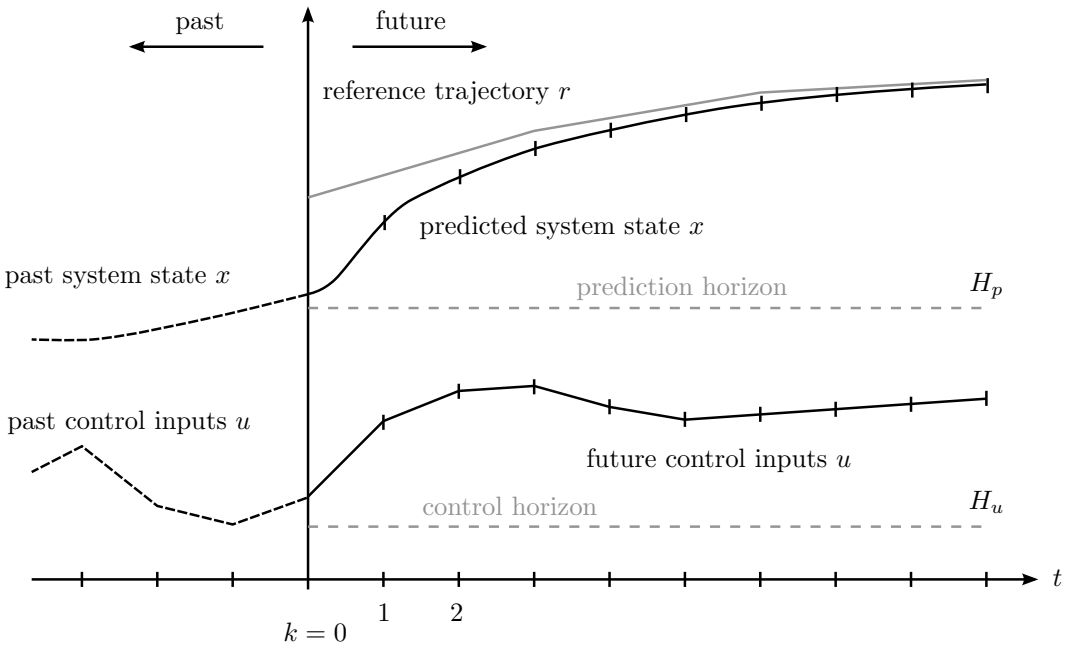

Figure 2.6.: Sketch of Nonlinear Model Predictive Control (NMPC)

The numerical minimizer varies the sequence of control inputs $\underline{u}$ at given sample points within the control horizon H_u. The development between the sample points (also denoted as control points) can be parametrized as piecewise constant (zero-order-hold), piecewise linear (first-order-hold, as shown in figure 2.6) or of higher order (for instance splines). The NMPC, typically, sends

out only the first control input into the plant and repeats the calculation when the next control input is required. The repetition time depends on the calculation time of the optimization. A more detailed description of predictive control working with nonlinear systems is given in the review by Findeisen and Allgöwer [Fin02] and Mahadevan and Doyle [Mah03].

Most of the numerical minimization algorithms handle lower and upper bounds for the input sequence explicitly. Also limitations for the system state can be explicitly considered, in form of inequality constraints. Inequality constraints are hard constraints which set conditions for the future development of the system state that are required to be satisfied. If the minimization algorithm does not support inequality constraints, soft constraints can be included in the objective function J in form of penalty functions f_p. Soft constrains can be also used if the minimization algorithm failed if a part of the prediction (for instance the beginning) always violates the constrains. In this case, a feasible solution does not exist according to hard constraints. In this thesis, equation 2.5 is used as objective function

$$\begin{aligned} J = & \frac{1}{H_p - 2} \sum_{k=2}^{H_p - 1} \underline{e}^T(k) \cdot \boldsymbol{W_x} \cdot \underline{e}(k) \\ & + \underline{e}^T(H_p) \cdot \boldsymbol{W_s} \cdot \underline{e}(H_p) \\ & + \frac{1}{H_u - 1} \sum_{k=2}^{H_u} \Delta \underline{u}^T(k) \cdot \boldsymbol{W_u} \cdot \Delta \underline{u}(k) \\ & + \frac{1}{H_p - 1} \sum_{k=2}^{H_p} \underline{f}_p^T(\underline{x}(k)) \cdot \boldsymbol{W_b} \cdot \underline{f}_p(\underline{x}(k)) \end{aligned} \tag{2.5}$$

to consider the regulation specification:

- control error $\underline{e}(k) = \underline{r}(k) - \underline{x}(k)$:
  Consideration of the difference between the predicted system state $\underline{x}$ and the reference trajectory $\underline{r}$ within the prediction horizon H_p. In the implemented automation of the FZ process, not all states have reference values. Here, the elements of the weight matrix $\boldsymbol{W_x}$ can be set to zero.
- final control error $\underline{e}(H_p)$:
  Consideration of the control error $\underline{e}$ at the end of the prediction horizon H_p to stabilize the process.
- change of input variables $\Delta \underline{u}(k) = \underline{u}(k) - \underline{u}(k-1)$:
  Consideration of the difference between the current control input $\underline{u}(k)$ and the previous control input $\underline{u}(k-1)$ within the control horizon H_u. An alternative is the consideration of the absolute value of the control input using the term $\underline{u}^T(k) \cdot \boldsymbol{W_u} \cdot \underline{u}(k)$.
- limitations for the system state:
  Consideration of process constraints, especially upper $\underline{x}_{ub}$ and lower limit $\underline{x}_{lb}$ of the system state. A penalty function $\underline{f}_p$ is used to take into account

limits for one or more system variables. Figure 2.7 shows the form of the penalty function (presented by Heine [Hei04])

$$\begin{aligned} f_p(x) = &(\frac{\pi}{2} + arctan(k_2(x - x_{ub})))^{k_1} \\ &+ (\frac{\pi}{2} - arctan(k_2(x - x_{lb})))^{k_1} \end{aligned} \tag{2.6}$$

using x_{lb}=-5, x_{ub}=5, k_1=7, and k_2=8.

The matrices $\boldsymbol{W_x}$, $\boldsymbol{W_s}$, $\boldsymbol{W_u}$ and $\boldsymbol{W_b}$ are used in equation 2.5 to weight the influence of the corresponding terms and to handle the magnitudes of the system states due to the different physical units. The summation starts at k=2, because the slope to the input value $\underline{u}(k = 1)$ is already sent out into the plant.

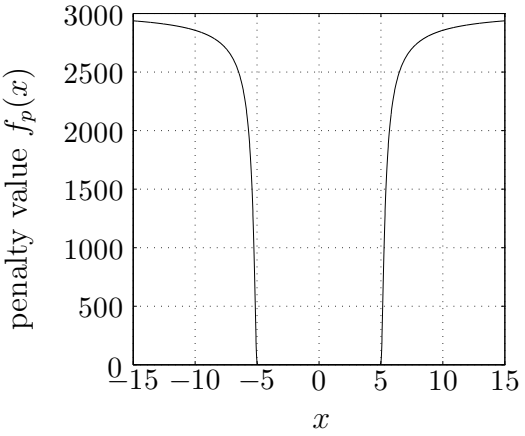

Figure 2.7.: Penalty function for a soft constraint using equation 2.6 with x_{lb} = -5, x_{ub} = 5, k_1 = 7, and k_2 = 8

2.5. State Estimation

2.5.1. Introduction

In control theory, a state observation is a method that produces estimates $\underline{\hat{x}}_k$ of the full state vector $\underline{x}_k$ of a system, generally based on measurements $\underline{y}_k$ and control inputs $\underline{u}_k$. In the following equations, the estimated values are denoted with ˆ on top. The time point of the k-th sample point of measurement is denoted with the index k. An estimation is needed if one or more state variables are not directly measurable. For control tasks, for instance stabilizing a system using state feedback, the full state has to be available. A state estimation also reduces the noise of the measurements. Commonly used estimation techniques are the Luenberger observation [Lue64] and the Kalman filter [Kal60].

In this thesis, the well-known and widely applied Kalman filter technique is used. It was developed around the 1960s and named after its inventor Rudolf

E. Kalman. Originally, it was applied for guidance, navigation and control of vehicles, particularly aircraft and spacecrafts. Today the Kalman filter is established in many other fields of technology. The algorithm consists of two steps: prediction and correction. In the prediction step, the Kalman filter produces estimations $\underline{\hat{x}}$ of the system state based on model equations, current state and control inputs. Once a new measured value is available (including random noise), the system state is updated using a weighted difference between the measurements and the predicted system output. The calculation is formulated in a recursive form using the present measurements, the present manipulated values and the previously estimated state. No additional information is required from the past. Currently, the Kalman filter is applicable in many different variations.

2.5.2. Continuous-Discrete Extended Kalman Filter

In this thesis, the continuous-discrete extended Kalman filter (EKF) is implemented, which works with nonlinear systems. Details are given in the reviews of Simon [Sim06], Heine [Hei04], and Welch and Bishop [Wel97]. The EKF is based on a continuous model and discrete measurements. The continuous model considers random disturbances of system and measurements. The state space model in section 2.4.1 is extended with these disturbances. The system model of the EKF is defined as

$$\dot{\underline{x}}(t) = \underline{f}(t, \underline{x}(t), \underline{u}(t), \underline{\Theta}) + \underline{\xi}(t) \quad , \tag{2.7}$$

$$\underline{y}(t) = \underline{h}(t, \underline{x}(t), \underline{u}(t), \underline{\Theta}) + \underline{\eta}(t) \quad , \tag{2.8}$$

where $\xi(t)$ is the random noise of the system and $\eta(t)$ that of the measurements. It is assumed that the random state $\underline{x}$ of the system can be approximated by a normal distribution. That means that the probability p of the state $\underline{x}_k$ is defined by the first moment $\underline{\hat{x}}_k$ (the mean value) and the second moment $\boldsymbol{P}_k$ (the covariance matrix) at the time point $t = t_k$

$$p(\underline{x}_k) \sim \mathcal{N}(\underline{\hat{x}}_k, \boldsymbol{P}_k) \quad . \tag{2.9}$$

Furthermore, the system and the measurement disturbances are assumed to be Gaussian white noise. That means, the disturbances are uncorrelated random signals with zero mean and normal distribution. The disturbances of the system $\underline{\xi}_k$ and the measurements $\underline{\eta}_k$ are defined as

$$p(\underline{\xi}_k) \sim \mathcal{N}(\underline{0}, \boldsymbol{Q}) \quad , \tag{2.10}$$

$$p(\underline{\eta}_k) \sim \mathcal{N}(\underline{0}, \boldsymbol{R}_k) \quad , \tag{2.11}$$

where $\boldsymbol{Q}$ is the spectral density of the system noise and $\boldsymbol{R}_k$ the covariance of the measurement noise at the time point $t = t_k$.

The EKF adjusts the estimated state $\underline{\hat{x}}_k$ and the covariance matrix $\boldsymbol{P}_k$ in each

iteration step (measurement and time update). The following quantities have to be determined for applying the EKF:

- the initial value of the estimated state $\underline{\hat{x}}_0$,
- the initial value of the covariance matrix $\boldsymbol{P}_0$,
- the spectral density $\boldsymbol{Q}$ of the system noise,
- the covariance matrix $\boldsymbol{R}_k$ of the measurement noise.

The values before the measurement update have the index $(-)$ and after it $(+)$. The known values and the ones to be calculated at the measurement and the time update are listed in table 2.1 and 2.2.

Measurement Update

The goal is to find the state $\underline{\hat{x}}_k^{(+)}$ with the highest probability $p(\underline{\hat{x}}_k|\underline{y}_k)$ considering the current estimation of the state $\underline{\hat{x}}_k^{(-)}$ and the available measurement $\underline{y}_k$,

$$\underline{\hat{x}}_k^{(+)} = \arg\max_{\underline{\hat{x}}_k} \left(p(\underline{\hat{x}}_k|\underline{y}_k)\right) \quad . \tag{2.12}$$

The maximization problem can be transformed into a minimization problem

$$\begin{aligned} \underline{\hat{x}}_k^{(+)} =& \arg\min_{\underline{\hat{x}}_k} \left(J(\underline{\hat{x}}_k)\right) \quad \text{with} \\ J(\underline{\hat{x}}_k) =& \frac{1}{2}(\underline{\hat{x}}_k - \underline{\hat{x}}_k^{(-)})^T (\boldsymbol{P}_k^{(-)})^{-1} (\underline{\hat{x}}_k - \underline{\hat{x}}_k^{(-)}) \\ &+ \frac{1}{2}(\underline{\hat{y}}_k - \underline{y}_k)^T (\boldsymbol{R}_k)^{-1} (\underline{\hat{y}}_k - \underline{y}_k) \end{aligned} \tag{2.13}$$

using the Bayes' law and the formula of the multivariate normal distribution[4]. The new covariance $\boldsymbol{P}_k^{(+)}$ after the measurement update is the inverse of the second derivative of the objective function J,

$$\boldsymbol{P}_k^{(+)} = \left(\frac{d^2 J}{d(\underline{\hat{x}}_k)^2}\bigg|_{\underline{\hat{x}}_k^{(+)}} \right)^{-1} \quad . \tag{2.14}$$

The equation 2.13 can be solved by an optimization algorithm. That is only useful, if the process permits enough calculation time. An analytic solution is found with the minimum condition of the gradient of the objective function J to be zero. Explicit formulas for calculating the estimated state $\underline{\hat{x}}_k^{(+)}$ and the

[4] the multivariate normal distribution is a generalization of the one-dimensional normal distribution for higher dimensions

covariance matrix $\boldsymbol{P}_k^{(+)}$ are

$$\underline{\hat{x}}_k^{(+)} = \underline{\hat{x}}_k^{(-)} + \boldsymbol{K}_k(\underline{y}_k - \underline{\hat{y}}_k^{(-)}) \quad , \tag{2.15}$$

$$\boldsymbol{P}_k^{(+)} = (\boldsymbol{I} - \boldsymbol{K}_k\boldsymbol{C}_k)\boldsymbol{P}_k^{(-)} \quad , \tag{2.16}$$

$$\boldsymbol{K}_k = \boldsymbol{P}_k^{(-)}\boldsymbol{C}_k^T(\boldsymbol{R}_k + \boldsymbol{C}_k\boldsymbol{P}_k^{(-)}\boldsymbol{C}_k^T)^{-1} \quad , \tag{2.17}$$

where $\boldsymbol{K}_k$ is the Kalman gain and $\boldsymbol{C}_k$

$$\boldsymbol{C}_k = \left.\frac{\partial \underline{h}}{\partial \underline{x}}\right|_{\underline{\hat{x}}_k^{(-)}} \tag{2.18}$$

the linearization of the output function $\underline{h}$ using a first-order Taylor approximation.

Time Update

During the time update, only model information is used to adjust the estimated state $\underline{\hat{x}}_{k+1}^{(-)}$ and covariance matrix $\boldsymbol{P}_{k+1}^{(-)}$

$$\underline{\hat{x}}_{k+1}^{(-)} := E\{\underline{x}_{k+1}|\underline{y}_k\} \quad , \tag{2.19}$$

$$\boldsymbol{P}_{k+1}^{(-)} := cov\{\underline{x}_{k+1}|\underline{y}_k\} \quad . \tag{2.20}$$

The model function f (equation 2.7) is used to deduct the following integrals to calculate the needed quantities

$$\underline{\hat{x}}_{k+1}^{(-)} = \int_{t_k}^{t_{k+1}} \underline{f}(\tau, \underline{x}(\tau), \underline{u}(\tau), \underline{\Theta})\,\mathrm{d}\tau \quad \text{with } \underline{x}(t_k) = \underline{\hat{x}}_k^{(+)} \quad , \tag{2.21}$$

$$\boldsymbol{P}_{k+1}^{(-)} = \int_{t_k}^{t_{k+1}} \left(\boldsymbol{A}_\tau\boldsymbol{P}(\tau) + \boldsymbol{P}(\tau)\boldsymbol{A}_\tau^T + \boldsymbol{Q}\right)\mathrm{d}\tau \quad \text{with } \boldsymbol{P}(t_k) = \boldsymbol{P}_k^{(+)} \quad . \tag{2.22}$$

Here, the matrix $\boldsymbol{A}_\tau$

$$\boldsymbol{A}_\tau = \left.\frac{\partial \underline{f}}{\partial \underline{x}}\right|_{\underline{\hat{x}}_\tau} \tag{2.23}$$

is the linearization of the model function $\underline{f}$ at time point τ using a first-order Taylor approximation. The linearization is realized at every time step of the integration to account for a nonlinear model.

Parameter Identification of the Kalman filter

The spectral density $\boldsymbol{Q}$ of the system noise, the covariance matrix $\boldsymbol{R}$ of the measurement noise, and the covariance matrix $\boldsymbol{P}_0$ of the initial state have to be determined for applying the Kalman filter. In this thesis, the matrix

symbol	description
known values at time point $t = t_k$	
$\underline{y}_k$	measurement of the system output
$\underline{\hat{x}}_k^{(-)}$	estimated state before the evaluation of $\underline{y}_k$
$\boldsymbol{P}_k^{(-)}$	covariance matrix of the estimated state $\underline{\hat{x}}_k^{(-)}$ before the evaluation of $\underline{y}_k$
$\boldsymbol{R}_k$	covariance matrix of the random measurement noise
$\underline{\hat{y}}_k = \underline{h}(t_k, \underline{\hat{x}}_k, \underline{u}_k, \underline{\Theta})$	estimation of the system output
calculated values within the measurement update	
$\underline{\hat{x}}_k^{(+)}$	estimated state after the evaluation of the measurement $\underline{y}_k$
$\boldsymbol{P}_k^{(+)}$	covariance matrix of the estimated state $\underline{\hat{x}}_k^{(+)}$ after the evaluation of $\underline{y}_k$

Table 2.1.: Known values and those to be calculated at the measurement update

symbol	description
known values from measurement update at time point $t = t_k$	
$\underline{\hat{x}}_k^{(+)}$	estimated state after the evaluation of the measurement $\underline{y}_k$
$\boldsymbol{P}_k^{(+)}$	covariance matrix of the estimated state $\underline{\hat{x}}_k^{(+)}$ after the evaluation of $\underline{y}_k$
$\boldsymbol{Q}$	spectral density of the system noise
calculated values within the time update	
$\underline{\hat{x}}_{k+1}^{(-)}$	estimated state after the time update at time point $t = t_{k+1}$
$\boldsymbol{P}_{k+1}^{(-)}$	covariance matrix of the estimated state $\underline{\hat{x}}_{k+1}^{(-)}$ after time update

Table 2.2.: Known values and those to be calculated at the time update

$\boldsymbol{P}_0$ is determined manually, based on experience. The matrices $\boldsymbol{Q}$ and $\boldsymbol{R}$ are obtained using numerical optimization. The objective function J_{QR}

$$J_{QR}(\boldsymbol{Q}, \boldsymbol{R}) = \sum_{k=1}^{N} [\underline{x}_k^{meas} - \underline{\hat{x}}_k]^T \, \boldsymbol{W}_{QR} \, [\underline{x}_k^{meas} - \underline{\hat{x}}_k] \tag{2.24}$$

is used, where $\underline{\hat{x}}_k$ is the estimated state using Kalman filter and $\underline{x}_k^{meas}$ the offline calculated state based on measurements. $\underline{x}_k^{meas}$ is the representation of the true state. Fitting the measurements by a piece-wise cubic spline filter can be applied to approximate the true values of the system state. Filtering by splines allows the reduction of measurement noise without introducing time delay (compared to low-pass filtering).

An optimization algorithm varies $\boldsymbol{Q}$ and $\boldsymbol{R}$ starting from the initial values $\boldsymbol{Q}_0$ and $\boldsymbol{R}_0$ to minimize the objective function J_{QR}. $\boldsymbol{W}_{QR}$ is used to weight the states (such as zone height or crystal angle) and to handle the magnitudes due to the different physical units. Section A.4.1 in the appendix gives the used values of the weight matrix $\boldsymbol{W}_{QR}$ for the FZ process and section A.5.1 and A.5.2 the obtained filter parameters.

3. Process Analysis

3.1. Floating Zone Process with RF Heating

The crucible-free FZ method developed by Theuerer (1952), Keck (1953), Golay (1953) and Emeis (1954) aims for growing pure silicon monocrystals. The main principle is based on the prevention of the incorporation of crucible material into the crystal by avoiding any contact of the melt with the crucible. In the FZ method, in contrast to CZ, only a small fraction of the feed rod is molten and than crystallized as a monocrystal. The molten zone between feed rod and growing crystal is established by a contactless heating. Possible methods of contactless heating are: electromagnetic (EM) fields, laser beams, focused lamp radiation, electron bombardment, electric arcs and plasma discharge (see Lüdge et al. [Lüd10]). For silicon crystals an inductive heating by a radio frequency (RF) EM field with a frequency of 2.5-3 MHz is used. The melting temperature of silicon is 1683 K. Today, FZ silicon crystals are grown with a maximum diameter of 200 mm. This is possible with the needle-eye technique, where the molten feed material flows through the inductor hole and crystallizes below in full diameter. The inductor hole is much smaller than the diameters of feed rod and crystal.

FZ is a batch process and consists of six phases - (1) producing the melt drop, (2) forming the feed tip, (3) creating the thin neck, (4) making the cone, (5) growing the cylinder and (6) closing the crystal. All phases are shown in figure 3.1. This process is realized in a growth chamber filled with a protective gas, for instance argon. The seed and the feed rod are attached to vertical spindles, which allow rotation, vertical motions and horizontal displacement.

Silicon as a semiconductor has an insufficient electrical conductivity at room temperature, hence, it is necessary to preheat the feed rod to more than 500 K to enable the coupling with the EM field of the inductor. In the first phase, the preheated feed rod is moved to the inductor and the lower end is molten inductively until a *melt drop* of liquid material hangs above the inductor hole. Figure 3.2 shows a RF induction coil with hole applicable to grow silicon crystals of 100 mm in diameter by the needle-eye FZ technique. The liquid drop of a proper size does not fall down due to the surface tension of the melt acting against gravity. As shown in figure 3.4 (a), the feed rod is shaped at the lower end using one or more segments with different angles.

The monocrystalline seed (of about 4-7 mm in diameter and approximately 50-100 mm in length) is slowly moved upwards to the drop and dipped into it. The solid seed is heated up to melting temperature and its top begins to melt after some minutes. After melting together, the feed rod and the seed are moved upwards to build the solid *feed tip*. Dislocations (disorders in the monocrystalline structure) are generated due to the thermal shock during

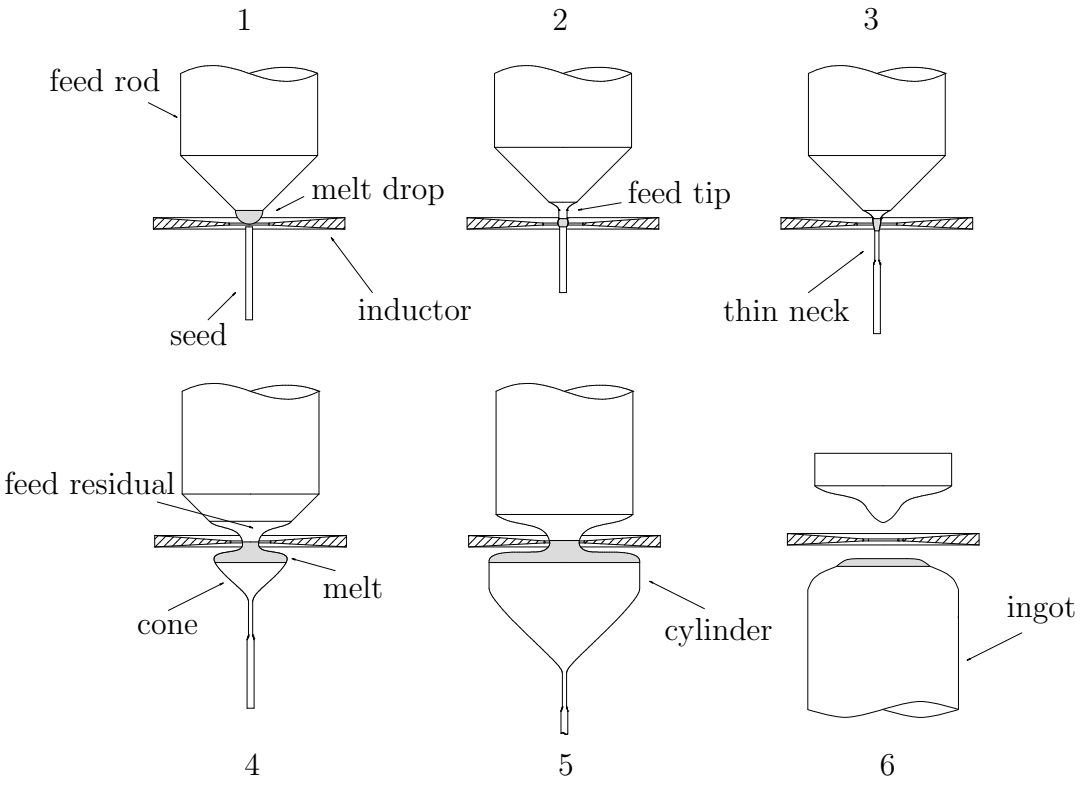

Figure 3.1.: Phases of the Floating Zone process. Producing the melt drop (1), forming the feed tip (2), creating the thin neck (3), making the cone (4), growing the cylinder (5) and closing the crystal (6). Solid material in white, melt in gray.

dipping a relatively cold seed into the melt.

To eliminate these dislocations, the crystal needs to be started with a *thin neck*. For this, seed and feed rod are moved downwards with increased pull rates. That results in a shrinking diameter down to about 2-3 mm. Depending on the orientation of the seed, the dislocations glide on planes which are tilted against the growth direction of the crystal. Existing dislocations grow off when they reach the surface of the thin neck (see Dash [Das59]). New dislocations are not generated because the thermomechanical stress is small at these diameters. After a few centimeters of pull length, all dislocations are grown off the thin neck.

Figure 3.3 shows the X-ray topogram of a silicon thin neck with outgrowing dislocations. The white lines are the dislocations. In the seed, many of them are visible but after a length of about 15 mm the thin neck is dislocation-free. The thin neck has a typical length of 30-50 mm, to make sure that there are no more dislocations. While creating the thin neck, the feed rod and the crystal are horizontally displaced from an axisymmetrical setup closer to the inductor main slit. The higher heater power at this place improves the melting behavior

Figure 3.2.: The RF induction coil with a hole diameter of 28 mm applicable to grow silicon crystals of 100 mm in diameter by the needle-eye FZ technique

of the feed material. In the next phases of the process, the axes of feed rod, crystal, and center of the inductor hole are the same.

The *cone phase* begins when the thin neck has a sufficient length of 30-50 mm. Here, the crystal diameter is increased by creating a melt overhang. This is done by adjusting heater power and feed rod pull rate. The crystal pull rate is constant within a typical range of 2-5 mm/min. Feed rod and crystal are rotated contrarily to stabilize the melt flow and to reduce thermal inhomogeneities caused by induction heating. This results in an approximately circular crystal. The feed rod is moved downwards, molten and the melt flows through the inductor hole. Here, a thin film of melt flows down along the solid *feed residual* into the melt. The cone is enlarged until the final diameter of the crystal is reached.

In the *cylinder phase* the crystal diameter is held constant. This is managed by constant power, constant rotation and constant pull rates of feed rod and crystal. The process is in a stable state within the cylinder phase. Today, crystals with a diameter of up to 200 mm and a length of several meters can be produced. The cylindrical part with constant diameter is called *ingot*. In the industrial application, the ingots are sliced into *wafers* being the substrates for the high-power electronic components.

At the end of the batch process, the crystal has to be separated from the feed rod. This is called *closing the crystal* and managed by moving the feed rod upwards until it divides from the molten zone. Then, the heater power is decreased slowly to control the crystallization of the melt. This has to be done carefully, because the melt volume expands by about 8% while crystallizing.

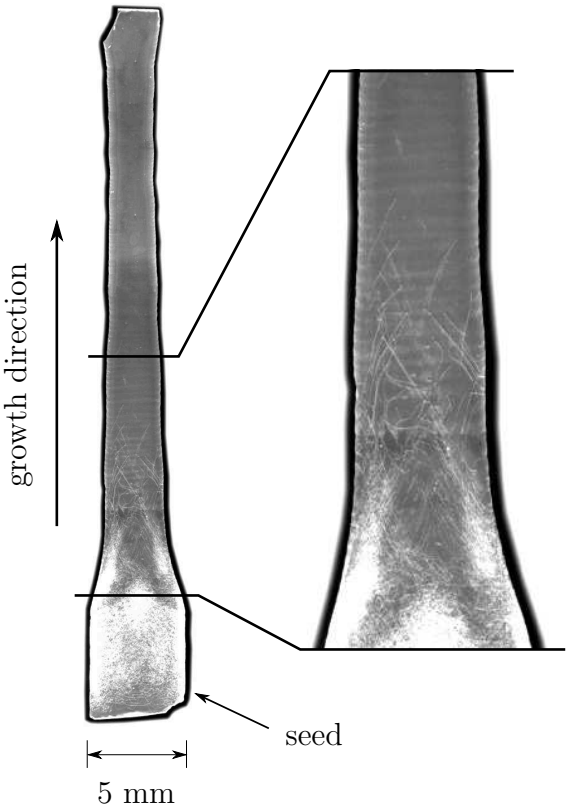

Figure 3.3.: X-ray topogram of a silicon thin neck with dislocations (white lines) at the beginning of the neck (left) and without them at the end (right). The dislocations grow out after 15 mm length of the neck. The image was taken by Alex [Ale75] at the Institute of Crystal Growth.

Therefore, the crystal would break apart if melt was surrounded by already crystallized material. Another important point is that during the separation, dislocations are introduced into the crystal by plastic deformation. The depth of the plastic deformation is directly proportional to the crystal diameter.

Figure 3.4 (a) shows an image of a polycrystalline feed rod with 110 mm diameter. The feed rod has one shaped segment at the lower end and its surface is ground. In an industrial setting, it is common to omit the surface grinding and feed rods with natural surface are used. Feed rods are produced by the *Siemens process* using the chemical vapor deposition (see Zulehner [Zul00]). Figure 3.4 (b) shows the cone of a crystal in the growth chamber. The crystal has a diameter of 125 mm. The seed is fixed in the crystal holder and a support device is used to stabilize the crystal against shaking.

Further details and descriptions of the FZ process are given in the works of Wilke [Wil88], Hurle [Hur94] and Lüdge et al. [Lüd10].

(a) Polycrystalline feed rod (b) Monocrystalline cone of a grown crystal

Figure 3.4.: Images of feed rod (a) and cone of a grown crystal (b). The feed rod is 110 mm and the crystal 125 mm in diameter. The feed rod is shaped before the process and the surface is ground.

3.2. Measurement System

3.2.1. Description of the Measurement System

Obviously measurements are needed for the control system, because they are the basis for all calculations of the controller. The growth chamber has an optical access to the FZ process through a quartz window so that the geometrical quantities of feed rod, molten zone and crystal can be obtained by visual image processing. In this thesis, the following camera system is used to measure the geometrical quantities. Two cameras capture the process: the first one observes the upper part (above the inductor) and the second one the lower part (below the inductor). Digital monochrome cameras, *Sony XCG-U100E* with C-Mount lenses *C2514-M(KP)* of 25 mm focal length are applied. A quick overview of the camera properties is given in table 3.1.

Rate	Picture Size	Image device	Digital interface	Lens mount
15 fps	1600 x 1200 pixel	1/1.8 type	GigE Vision	C mount

Table 3.1.: Properties of the digital camera *Sony XCG-U100E*.

The cameras have gigabit Ethernet interface (*GigE Vision*), which is used to connect them to the image processing computer. The Ethernet connection provides the process images and allows the configuration of the camera. The cameras are positioned so that an image resolution of approximately 9 - 11 pixel per millimeter is provided. Thus, an accurate detection of the geometrical data of small crystals and those of up to 150 mm in diameter by using the same camera is possible. The accuracy of the measurements is investigated in section 3.2.7. During the process, the cameras are operated with a constant exposure time of 100 - 300 µs and a rate of 10 frames per second.

The inductor covers a part of feed residual and molten zone and reduces the visibility of these regions. The cameras have a slight angle of approximately 3 °, downwards and upwards, respectively, to capture the corresponding zone as soon as possible (see figure 3.5 (a)). In the thin neck phase, the height of the molten zone is in a range of 4 - 12 mm. Inductors, capable of growing crystals with more than 150 mm in diameter have heights of approximately 15 - 20 mm. Here, a larger angle is necessary for both cameras to capture the desired parts (see the outer cameras in figure 3.5 (b)).

3.2.2. Visual Image Processing

The images provided by the camera system are analyzed to obtain the geometrical quantities of the process. This is done by a software running on a standard PC with a Windows operating system. The model-based controller and the observer run in parallel on the same computer. The PC has an Intel Core i5 processor (dual core, 4 threads) and 4 GB RAM. A rate of 10 analyzed

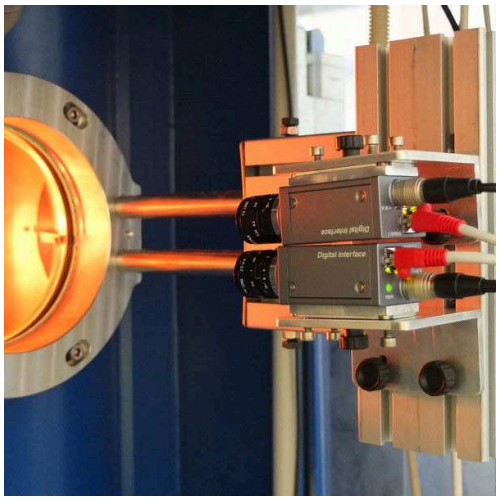

(a) Two camera system usable for cone and cylinder phases

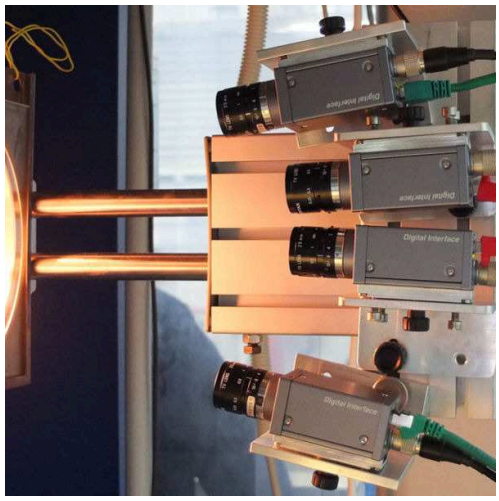

(b) Four camera system: the outer cameras are used during the thin neck phase and the center cameras during cone and cylinder phases

Figure 3.5.: Digital camera systems capture the FZ process

images per second is desired. The computational effort can be reduced by defining the *region of interest*. Then, only that region is analyzed to estimate the needed quantities. Furthermore, the image processing of the two cameras can be done simultaneously by distributing two separate threads. Table 3.2 gives an overview of the geometrical quantities. The camera from which the quantities are estimated is indicated.

Geometrical quantity	Lower camera	Upper camera
Visible melt volume V_{vi}	x	
Crystal radius R_C	x	
Crystal angle φ_C	x	
Feed radius R_F		x
Feed angle α_F		x
Height of the inductor h_I		x
Height of the upper zone h_F		x
Height of the lower zone h_C	x	
Radius of the melt neck R_N	x	

Table 3.2.: Geometrical quantities estimated by the measurement system

Figure 3.6 (a) shows a sketch of the geometrical quantities calculated from measurements in the cone phase. These quantities are obtained by detecting edges in the camera image. An edge is a sharp change in the image brightness and can be found by analyzing the brightness gradient (more details are given

in section 3.2.4). The crystal radius R_C is directly measured at the solid-liquid interface (line of crystallization) as half the distance between the left and right outer contour. The lower zone height h_C is measured as the distance between the lower edge of the inductor and the solid-liquid interface. The line of crystallization can be clearly detected by the sharp contour due to the different emissivities of solid and liquid silicon. The visible melt volume V_{vi} is calculated from the outer contour of the molten zone assuming rotational symmetry according to the vertical axis. Instead of the real melt neck, which is covered by the inductor, an approximated R_N is measured directly below the inductor. Two approaches are available to obtain the height of the upper zone h_F. First, finding the line of melting and second, identifying the melting edges. The line of melting is difficult to identify because it does not have a comparably sharp contour as the outer solid-liquid interface of the crystal does. The distance between the melting edge and the inductor provides more robust measurements and is used as upper zone height h_F. The feed rod is shaped at the lower end using one or more segments with different angles. So, it is required to measure radius R_F and angle α_F of the feed rod. The height of the inductor h_I is known before the growth process, but it is measured to avoid configuration errors.

Figure 3.6 (b) shows a sketch of the geometrical quantities in feed tip and thin neck phase. As already showed in figure 3.5 (b), the outer cameras are aligned to capture the full molten zone.

3.2.3. Correction of the Brightness

The used digital cameras provide a monochrome image with a grayscale range per pixel from 0 (black) to 255 (white). During the process, the brightness of the images changes, because crystals with small diameters produce a lower brightness level as larger ones. Especially in the thin neck phase, the brightness is very low due to the small diameter and the low zone height. To reduce the brightness problem during the process, the brightness can be normalized pixel-wise according to the linear formula

$$I^{new} = (I - min)\Big(\frac{max^{new} - min^{new}}{max - min}\Big) + min^{new} \quad , \tag{3.1}$$

where I^{new} is the new image, I the camera image, $[min,\ max]$ the grayscale range of the camera image and $[min^{new},\ max^{new}]$ the desired range of the new image. It makes sense to normalize the new image to the range between $[0, 255]$ to produce a maximum contrast. The range of the camera image can be determined by time-consuming estimations. Alternatively, constant minimal and maximal gray values can be used. Pixels with gray values outside of the limitations are adjusted to the limitations.

Figure 3.7 shows the original image from the upper camera (a), the applied

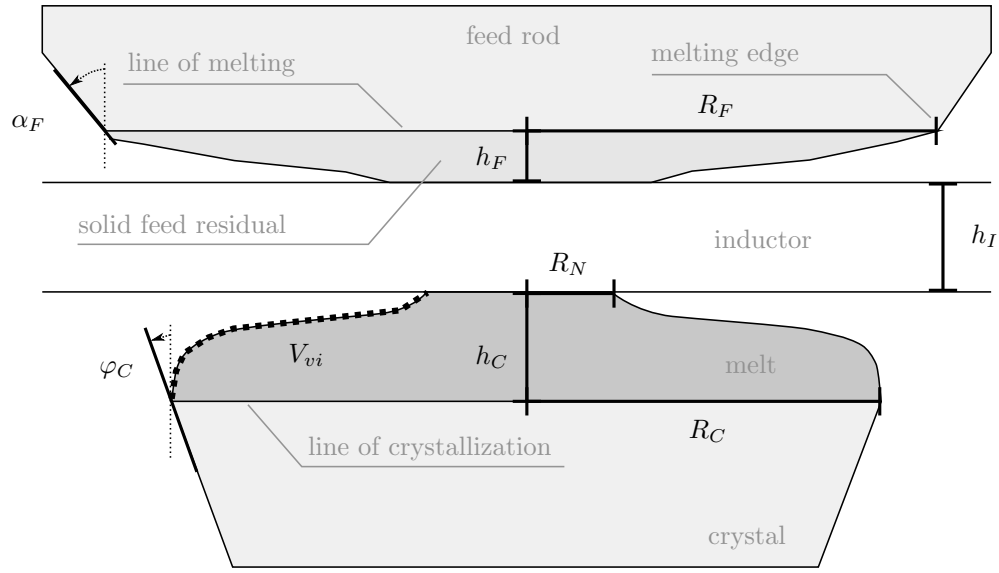

(a) Cone phase

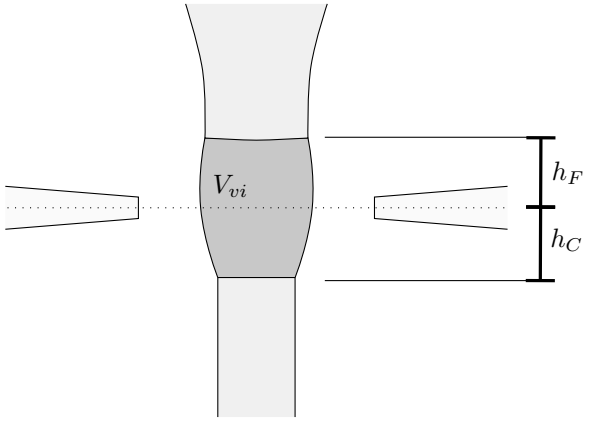

(b) Feed tip phase and thin neck phase

Figure 3.6.: Geometrical quantities calculated from measurements: visible melt volume V_{vi}, crystal radius R_C, crystal angle φ_C, feed radius R_F, feed angle α_F, upper zone height h_F, lower zone height h_C, height of the inductor h_I, radius of the melt neck R_N.

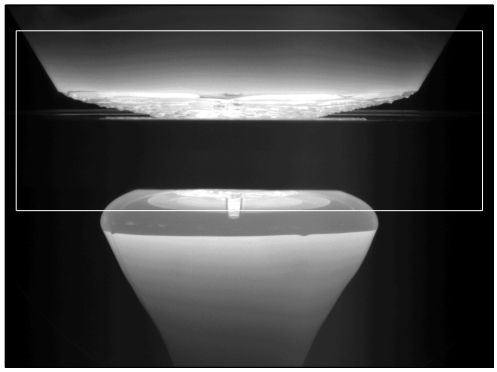

(a) Image of the upper camera: Original

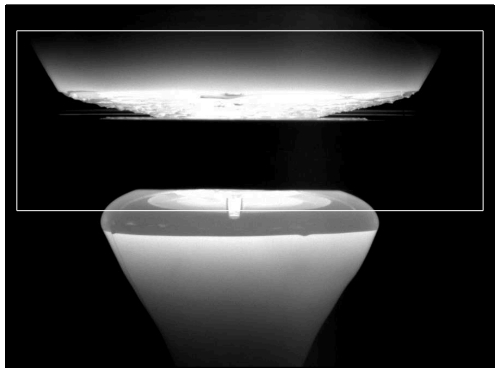

(b) Image of the upper camera: After brightness correction.

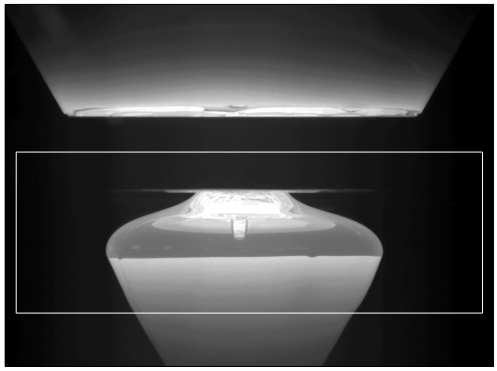

(c) Image of the lower camera: Original

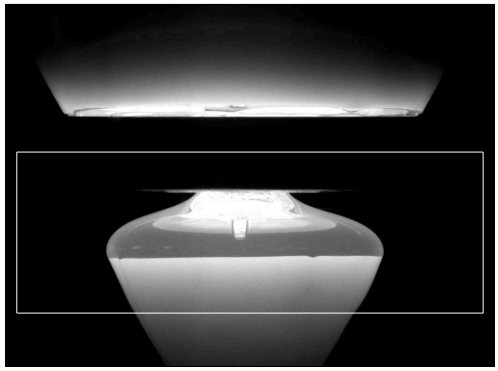

(d) Image of the lower camera: After brightness correction.

Figure 3.7.: Original camera images (a), (c) and correction of the brightness (b), (d) using equation 3.1. Gray values between $[min, max]$ = [50, 230] are normalized to [0, 255]. The white rectangle is the *region of interest*.

correction of brightness (b), the original image from the lower camera (c), and the corresponding correction (d). Upper and lower limitations of 50 and 230 are applied. As shown in figure 3.7 (b) and (d), the full image is corrected. In the running measurement system only the *region of interest* (marked as white rectangle) is considered in order to reduce, among other things, the computational effort.

3.2.4. Finding the Geometrical Quantities by Edge Detection

This paragraph provides details concerning the applied algorithm to find the geometrical quantities such as diameter and zone height. The algorithm is based on the idea of edge detection, a mathematical methods to identify points in a digital image. The points are characterized by a sharp change of the image brightness. Most of the edge detection methods can be assigned into two categories, the search-based and the zero-crossing based approach. The

search-based method calculates a measure of edge strength first, usually a first-order derivative such as a gradient, and then searches a local maximum value of the gradient. The zero-crossing based method uses a second-order derivative in order to find edges as zero crossings. Common second-order derivatives are Laplacian or non-linear differential expressions. A survey of different edge detection methods can be found in the review by Ziou and Tabbone [Zio98].

In this thesis the search-based method is applied. The magnitude of the gradient

$$|grad| = \sqrt{\left(\frac{\partial}{\partial x}\right)^2 + \left(\frac{\partial}{\partial y}\right)^2} \tag{3.2}$$

is estimated using two 3×3 filter masks, which are convolved with the original image - one for horizontal changes S_x, and one for vertical ones S_y. The magnitude of the gradient at (x,y) of the image I is calculated using

$$|grad(x,y)| = \sqrt{\Big(G_x(x,y)\Big)^2 + \Big(G_y(x,y)\Big)^2} \quad , \tag{3.3}$$

where G_x and G_y are the result of the convolution operation

$$G_x(x,y) = S_x * I(x,y) \quad \text{and} \tag{3.4}$$
$$G_y(x,y) = S_y * I(x,y) \quad . \tag{3.5}$$

The terms S_x and S_y are the convolution masks and the operator $*$ denotes the 2-dimensional convolution operation

$$S_x * I(x,y) = \sum_{i=0}^{2}\sum_{j=0}^{2} S_x(i,j) \cdot I(x+i-1, y+j-1) \quad \text{and} \tag{3.6}$$

$$S_y * I(x,y) = \sum_{i=0}^{2}\sum_{j=0}^{2} S_y(i,j) \cdot I(x+i-1, y+j-1) \quad . \tag{3.7}$$

The direction of the gradient can be calculated in terms of the angle α

$$\alpha(x,y) = arctan\Big(\frac{G_y(x,y)}{G_x(x,y)}\Big) \quad , \tag{3.8}$$

but it is not relevant in the identification method of this work.

The search-based methods rely on the computation of image gradients, but they differ in the types of filter masks used for the x- and y-directions of the gradient. Figure 3.8 (a) gives the result of the calculated gradient of the lower camera image already considered in figure 3.7 (d). The image has a resolution of 9.21 pixel per millimeter and a pixel resolution of 1600×1200 pixel. The figure shows the calculated gradients for a wide range. In online use, only the gradients are calculated according to the region of interest.

The gradient calculation uses the filter masks

$$S_x = \frac{1}{8}\begin{pmatrix} -1 & 0 & 1 \\ -2 & 0 & 2 \\ -1 & 0 & 1 \end{pmatrix} \quad \text{and} \quad S_y = \frac{1}{8}\begin{pmatrix} -1 & -2 & -1 \\ 0 & 0 & 0 \\ 1 & 2 & 1 \end{pmatrix}$$

and equation 3.3. The geometrical quantities such as shape of crystal and melt are visualized by bright lines and have to be identified separately. This can be done by searching local maximum values of the gradient, the so-called peaks. Figure 3.8 (b) shows the gradient at the vertical axis $x = 850$ px to provide an example for the identification of the lower zone height. Three peaks are clearly visible in figure 3.8 (b). The left peak at $y = 530$ px represents the upper edge of the inductor, the middle one at $y = 670$ px is the lower edge of the inductor, and the right one at $y = 795$ px the solid-liquid interface. The distance between middle and right peak is the height of the lower zone. The peaks are local maximum values of the gradient. A limit (for instance 25 in figure 3.8 (b)) can be defined to identify the local regions. The values above the limit identify the local regions and the peaks can be located at the maximum gradient within that regions.

Figure 3.9 (a) shows the gradient of the upper camera image. The image has a resolution of 9.17 pixel per millimeter. The line of melting does not have a comparably sharp contour as the solid-liquid interface of the crystal. Figure 3.9 (b) shows the vertical curve of the gradient at $x = 800$ px. The left peak at $y = 285$ px is the line of melting, the peak at $y = 325$ px is the upper edge of the inductor, the peak at $y = 460$ px is the lower edge of the inductor, and the right one at $y = 550$ px is the solid-liquid interface of the crystal.

3.2.5. Correction of the Obtained Diameter

For larger diameters, the observed diameter of the cylinder (crystal or feed rod) differs from the real diameter. The difference depends on the distance c between the camera and the center of the cylinder. Figure 3.10 shows the top view of the cylinder observed by the camera. The distance between the camera and the center of the cylinder is denoted by c. The radius observed by the camera is R_{cam} and the real radius of the cylinder is R_{real}. Thales' theorem can be used to construct the tangent to the cylinder passing the camera position. The right-angled triangles shown in figure 3.10 give the formulations

$$\left(\frac{c}{2}\right)^2 = R_{cam}^2 + q^2 \quad \text{and} \tag{3.9}$$

$$R_{real}^2 = R_{cam}^2 + p^2 \tag{3.10}$$

including the auxilary quantities p, q, and their relation $\frac{c}{2} = p + q$. Based on these equations it is possible to formulate an explicit equation for the real

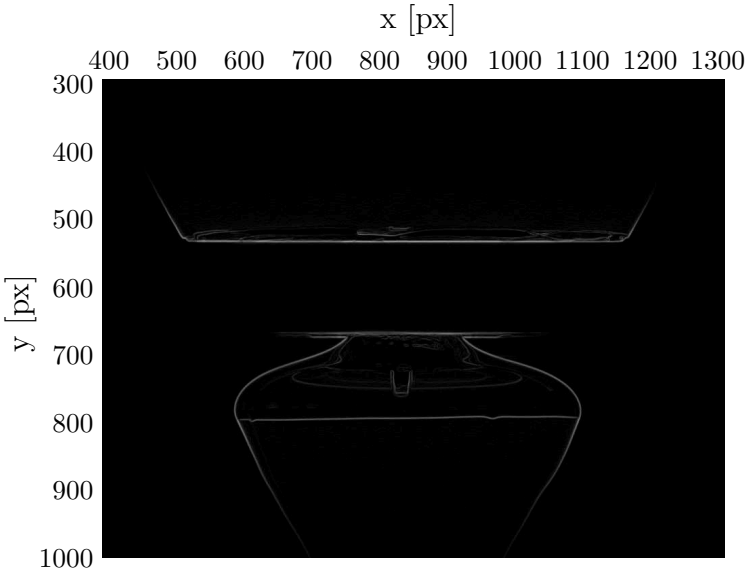

(a) Calculated gradient of the image of the lower camera. The image in figure 3.7 (d) is used after brightness correction. The pixel resolution of the full image is 1600×1200 pixel. In online use, only the gradients are calculated according to the region of interest.

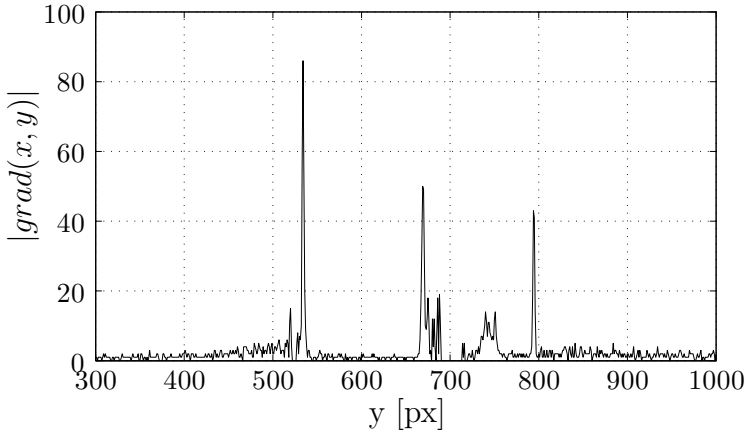

(b) Plot of the gradient at the vertical axis $x = 800$ px. The left peak at $y = 530$ px is the upper edge of the inductor, the middle one at $y = 670$ px is the lower edge of the inductor, and the right one at $y = 795$ px the solid-liquid interface. The distance between middle and right peak is the height of the lower zone.

Figure 3.8.: Example of the gradient of the image of the lower camera. The camera image has a resolution of 9.21 pixel per millimeter. The 2-dimensional gradient field in (a) and the vertical curve (b) of the gradient at $x = 800$ px are shown.

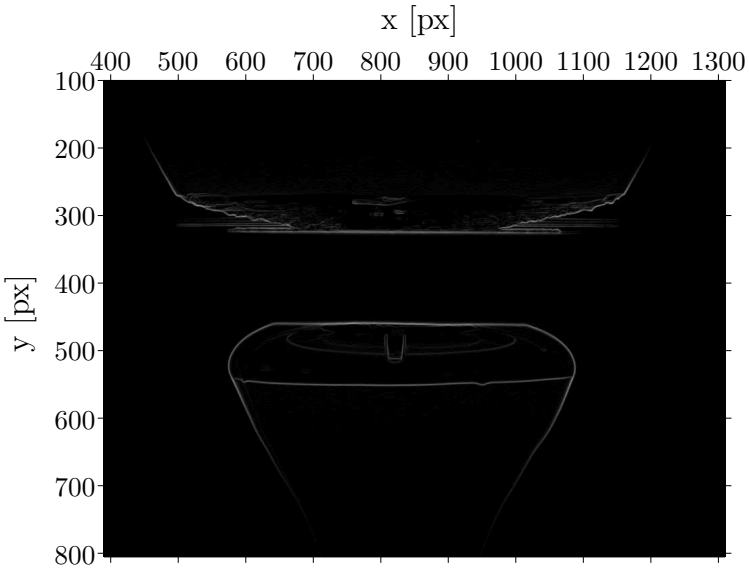

(a) Calculated gradient of the image of the upper camera.

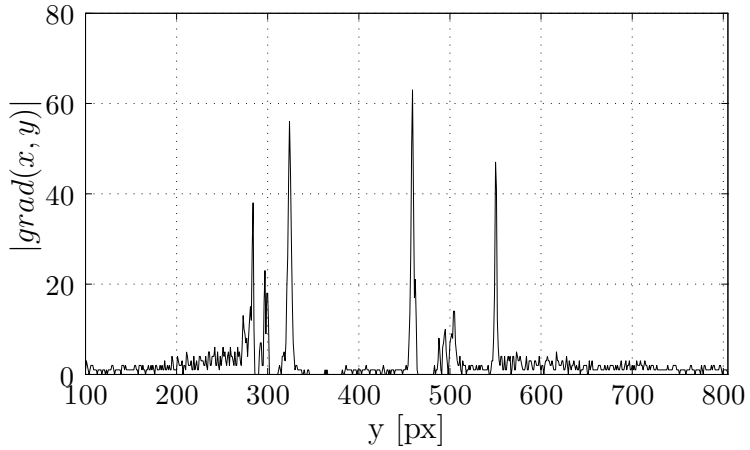

(b) Plot of the gradient at the vertical axis $x = 800$ px. The left peak at $y = 285$ px is the line of melting, the peak at $y = 325$ px is the upper edge of the inductor, the peak at $y = 460$ px is the lower edge of the inductor, and the right one at $y = 550$ px is the solid-liquid interface of the crystal.

Figure 3.9.: Example of the gradient of the image of the upper camera. The camera image has a resolution of 9.17 pixel per millimeter. The 2-dimensional gradient field in (a) and the vertical curve (b) of the gradient at $x = 800$ px are shown.

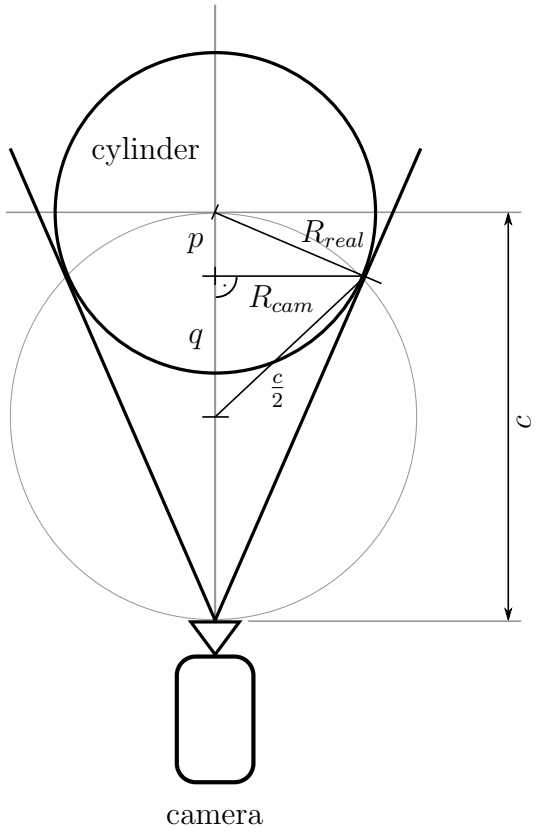

Figure 3.10.: Top view of the cylinder (crystal or feed rod) observed by the camera. Where c is the distance between cylinder and camera, R_{cam} the observed radius and R_{real} the real radius. The auxiliary quantities p and q are involved in the deduction of the correction formula given in equation 3.14.

radius R_{real}:

$$R_{real}^2 = R_{cam}^2 + (\frac{c}{2} - q)^2 \tag{3.11}$$

$$= R_{cam}^2 + \left(\frac{c}{2} - \sqrt{\left(\frac{c}{2}\right)^2 - R_{cam}^2}\right)^2 \tag{3.12}$$

$$= \frac{c^2}{2} - c\sqrt{\left(\frac{c}{2}\right)^2 - R_{cam}^2} \quad . \tag{3.13}$$

Using diameters ($D_{real} = 2R_{real}$ and $D_{cam} = 2R_{cam}$) instead of radii results in the formulation

$$D_{real} = \sqrt{2c^2 - 2c\sqrt{c^2 - D_{cam}^2}} \tag{3.14}$$

to calculate the real diameter D_{real} based on the observed diameter D_{cam} and the camera distance c. Figure 3.11 shows the difference between the real diameter D_{real} and the observed diameter D_{cam} for three camera distances

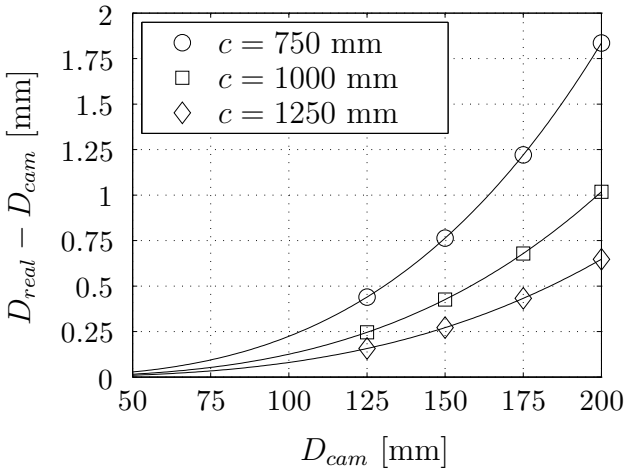

Figure 3.11.: Plot of the difference between the the real diameter D_{real} and the observed diameter D_{cam} for three camera distances $c = 750$ mm, $c = 1000$ mm, and $c = 1250$ mm. The values are calculated by using equation 3.14.

$c = 750$ mm, $c = 1000$ mm, and $c = 1250$ mm. The values are calculated by using equation 3.14. The diameter difference of a cylinder of 150 mm diameter is approximately 0.4 mm using a typical camera distance of 1000 mm.

3.2.6. Improvement of the Accuracy by Sub-Pixel Interpolation

Sub-pixel interpolation is a technique to increase the limited resolution of discrete signals such as digital audio and image signals. The technique provides data of positions between sample points (see figure 3.12). Examples for interpolation methods are bi-linear and bi-cubic interpolation. Applying these methods, artifacts can be created in the signal. Fast Fourier interpolation is commonly used in up-sampling of audio data and digital images to avoid artifacts.

In this work, sub-pixel interpolation based on the Fourier transformation is applied to achieve efficient and high-quality interpolations. A detailed description of the Fourier transformation and its application in image processing is given in the book of Shih [Shi10].

3.2.7. Calibration of the Camera System

This section presents the calibration technique for the digital cameras. The geometrical quantities are initially available as pixel values due to the analysis of digital images. It is needed to convert the pixel information into length values. In other words, it is required to translate what the camera sees in sensor coordinates (pixels) to length units (millimeters). The converting rate is the pixel density PPMM with the unit pixel per millimeter.

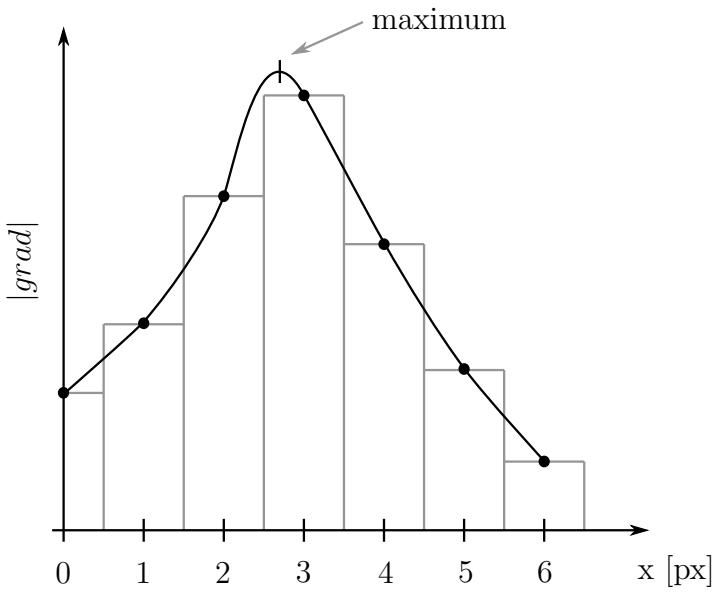

Figure 3.12.: Sketch of sub-pixel interpolation to increase the accuracy of the maximum identification

The diameter D_{mm} in millimeter is calculated by the linear calibration function

$$D_{mm} = D_{px}/PPMM \tag{3.15}$$

involving the diameter D_{px} in pixel. The pixel density, generally, depends on distance and angle of the camera, the used lens and the focus setting. Hence, each camera has to be calibrated separately.

Discs with different diameters ($\varnothing = 25, 50, 75, 100, 125, 150$ mm) are used to obtain the pixel density of the digital camera. First, the disc diameter D_{px} in pixel is measured for each disc by using the identification method (see sections 3.2.4, 3.2.6, and 3.2.5). The discs are rotated with a rate of 6 rotations per minute and the mean value of the diameter D_{px} (according to a measuring time of 2 minutes) is calculated. Then, the pixel density PPMM is estimated by least squares minimization of the disc diameter and the calculated diameter D_{mm} using equation 3.15.

Table 3.3 shows the data of a calibration process including mean value and standard deviation of the measured diameter D_{px} in pixel for each disc (column 2 and 3) and the corresponding values of the PPMM-function (column 3 and 4). The standard deviation of the measured pixel diameter D_{px} is less than 0.1 %. The measurement error of the diameter D_m is between -0.44 mm and +0.53 mm. For crystals of 100 - 125 mm diameter, a measurement precision of ± 0.29 mm can be expected. To reduce the measurement error for a larger range, the calibration function can be extended by additional terms.

disc	meas D_{px}		calibration func.	
diameter	mean	std	D_{mm}	error
[mm]	[px]	[px]	[mm]	[mm]
25	225.76	±0.14	24.65	-0.35
50	453.95	±0.17	49.56	-0.44
75	683.40	±0.14	74.61	-0.39
100	913.32	±0.12	99.71	-0.29
125	1145.56	±0.15	125.06	+0.06
150	1378.81	±0.18	150.53	+0.53

Table 3.3.: Data of a calibration process including mean value and standard deviation of the measured diameter D_{px} in pixels for each disc (column 2 and 3) and the corresponding values of the calibration function (column 3 and 4). The estimated pixel density PPMM is 9.1596 px/mm. The linear calibration function is given in equation 3.15.

3.3. Deflection of the Solid-Liquid Interface

This section gives an approximation of the melt volume V_{bo} that arises due to the deflection of the solid-liquid interface (also known as crystallization interface) in the growing crystal. This approximation is used to model the melt volume in section 4.1.5. An interface deflection occurs because of the radial temperature gradient in the crystal. The temperature at the longitudinal axis is higher than the temperature at the crystal surface. The volume V_{bo} of the *melt bowl* is not measurable during the experiment, because it is covered by the crystal surface. The method Lateral-Photovoltage-Scanning (LPS) visualizes the solid-liquid interface a posteriori. First, a longitudinal section of the crystal is produced. Laser light is focused on this section and generates free electron/hole pairs, which diffuse into the bulk of the crystal. This leads to a small potential difference, which can be measured by phase-sensitive signal processing. The magnitude of this voltage depends on the lateral resistivity gradient. An interface, solidified at the same time, results in the same voltage measurement. In the end, the voltage measurement is converted into a gray value and arranged in a pixel image. To get a better visualization of the solid-liquid interface, the resistivity gradient has to be increased by doping the melt during the growth experiment. A detailed description of the LPS method is given in the publications by Lüdge and Riemann [Lüd97] and Abrosimov et al. [Abr02].

Figure 3.13 (a) shows an image of a silicon crystal cone by LPS visualization, which is used to identify the solid-liquid interface. As shown in figure 3.13 (b), the deflection height $z(r)$ is obtained for the sample points at $r = 0$, $r = 0.25R_C$, $r = 0.5R_C$ and $r = 0.75R_C$. A third-order polynomial is fitted to the sample points. This cubic function is a continuous representation of the

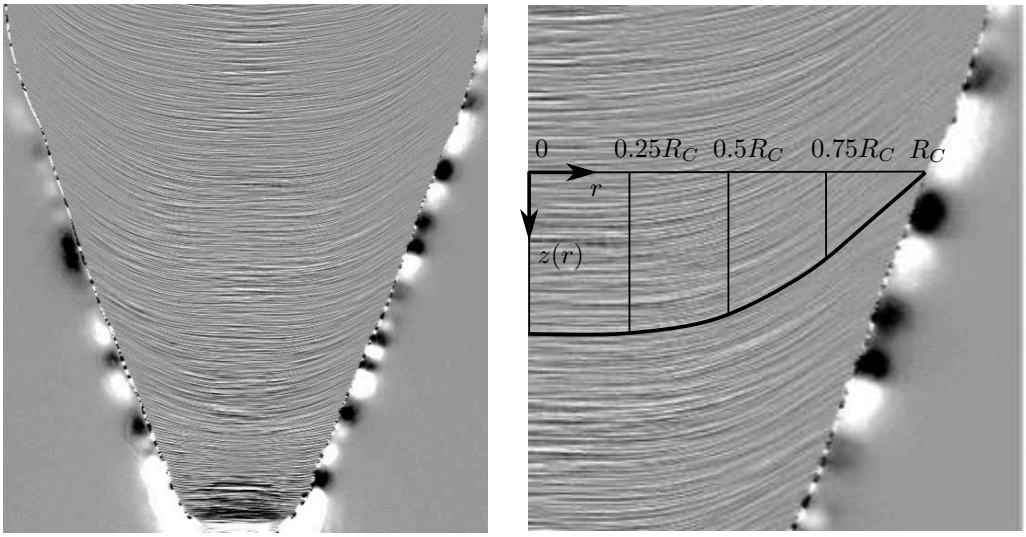

(a) Visualization of the solid-liquid interface on an axial cut of a silicon crystal cone

(b) Identification of the solid-liquid interface by using four sample points and fitting with a third-order polynomial

Figure 3.13.: Visualization (a) and identification (b) of the solid-liquid interface by using the Lateral-Photovoltage-Scanning (LPS) method

deflection line. That is done for several crystal radii R_C. It is assumed that the deflection is rotationally symmetric to the longitudinal axis z. The bowl volume V_{bo} is calculated from the equation

$$V_{bo}(R_C) = 2\pi \int_0^{R_C} r z(r)\,\mathrm{d}r \qquad . \tag{3.16}$$

Figure 3.14 shows the bowl height (a) and the bowl volume (b) for three experiments. The experiments are made with the same inductor at the same FZ machine. In both figures, the evolution of the variables has the same trend, but differs in the absolute values. The reason is that the shape of the solid-liquid interface depends on other parameters such as the lower zone height, which is the distance between the interface and the heater source. Especially, the bowl height shows a large variation between the experiments. The review by Lüdge et al. [Lüd02] shows that the crystal pull rate influences the deflection of the solid-liquid interface as well.

An alternative approach to calculate the solid-liquid interface is a simulation of the temperature field based on heat transfer. The solid-liquid interface is the melting point isotherm. For this purpose, a transient model based on partial differential equations would have to be solved to get representative results for the cone phase. The calculation would be too slow for real-time use during an experiment. A priori calculations and a usage of lookup tables for many machine setups would be too expensive.

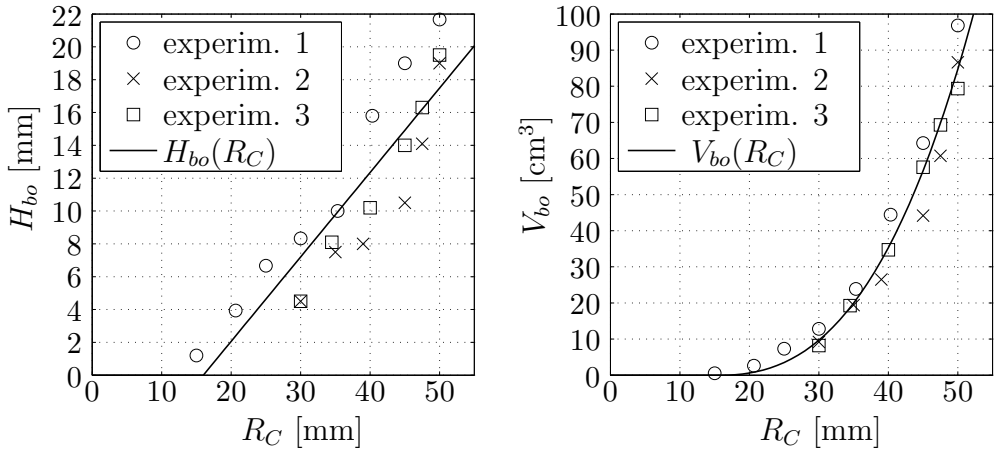

(a) Melt bowl height H_{bo} over crystal radius R_C

(b) Melt bowl volume V_{bo} over crystal radius R_C

Figure 3.14.: Height H_{bo} (a) and volume V_{bo} (b) of the melt bowl over crystal radius R_C for three experiments obtained by Lateral-Photovoltage-Scanning (LPS). Functions $H_{bo}(R_C)$ and $V_{bo}(R_C)$ are plotted to interpolate the values (see equation 3.17 and 3.18).

An interpolating function depending on the crystal radius R_C is used to get a usable equation for the height H_{bo} and the volume V_{bo} of the bowl without time-consuming calculations. The equation for calculating the melt bowl height H_{bo} in mm

$$H_{bo}(R_C) = \begin{cases} 0 & \text{for } R_C \leq b_0 \\ b_1(R_C - b_0) & \text{for } R_C > b_0 \end{cases} \tag{3.17}$$

includes the crystal radius R_C and the model parameters $b_0 = 16$ mm and $b_1 = 0.5143$. The equation for calculating the melt bowl volume V_{bo} in mm^3

$$V_{bo}(R_C) = \begin{cases} 0 & \text{for } R_C \leq a_0 \text{ and } a_0 = b_0 \\ \sum_{i=1}^{3} a_i(R_C - a_0)^i & \text{for } R_C > a_0 \end{cases} \tag{3.18}$$

and the time derivative $\dot{V}_{bo}$

$$\dot{V}_{bo}(R_C, \dot{R}_C) = \begin{cases} 0 & \text{for } R_C \leq a_0 \text{ and } a_0 = b_0 \\ \dot{R}_C \sum_{i=1}^{3} i \cdot a_i(R_C - a_0)^{i-1} & \text{for } R_C > a_0 \end{cases} \tag{3.19}$$

include the crystal radius R_C in mm, the derivative $\dot{R}_C$ in mm/s and the model parameters $a_0 = 16$ mm, $a_1 = 0$ mm^2, $a_2 = 32.48$ mm and $a_3 = 1.2$. The time derivative of the bowl volume $\dot{V}_{bo}$ is used in the volume model to describe the FZ process. A characteristic line in form of a third-order polynomial without

a zero and first order term is used due to:

- the volume of a sphere expands by the third power of the radius,
- deflection and volume of the bowl for radius $R_C < 16$ mm are close to zero and can be neglected ($a_0 = b_0 = 16$ mm),
- the characteristic line for the volume has to be continuous and differentiable at the point $R_C = a_0$.

3.4. Residual of the Feed Rod

In section 4.1.5 the mass balance is used to obtain a model equation for the melt volume. Therefore, it is necessary to identify the mass of the solid feed material. As shown in figure 3.15, the solid feed material consist of two solid parts one above and another below the line of melting. Above this line, the feed is unaffected by the induction heater and directly below, a thin film of melt flows down along the solid front into the molten zone. In this thesis, the solid part below the line of melting is denoted as *feed residual* and its surface as *open melting front*. Menzel [Men12] and Ratnieks [Rat07] calculated the thickness of the melt film depending on diameter, pull rate and rotation rate of the feed rod. They showed that for typical FZ process parameters the melt film has a thickness smaller then 0.2 mm. Therefore, the melt film is neglected during the investigation of the feed residual. The feed residual consist of a visible and a hidden part covered by the inductor. For a diameter of the feed rod smaller than approximately 20 mm, the feed residual is completely covered by the inductor. This depends on the angle of the upper camera. The reflection at the inductor surface, shown in figure 3.15, results from the inclination angle of the camera. The white dashed line indicates the complete feed residual consisting of the visible and the hidden part.

Rough approximations of the volume V_{fr} of the visible part of the feed residual are given in this section. The volume will be described by a function of the feed radius R_F to obtain a simple expression for V_{fr} and $\dot{V}_{fr}$. Images of the upper camera (such as shown in figure 3.15) are analyzed offline to obtain the geometry of the feed residual. The volume V_{fr} of the visible feed residual is calculated based on the manually identified shape and assuming rotational symmetry. It has to be pointed out that this is only a rough approximation due to the following reasons. First, the shape of the feed residual depends on the inductor design and the height of the upper zone. Second, it is difficult to identify the line of melting because it does not have a comparably sharp contour as the outer solid-liquid interface of the crystal. The line connecting the molten edges of both sides is used to determine the melting line. Third, the lower part of the feed residual is covered by the inductor.

Figure 3.16 shows the obtained volume V_{fr} plotted over the feed radius R_F. The images of three experiments are analyzed. The experiments were made

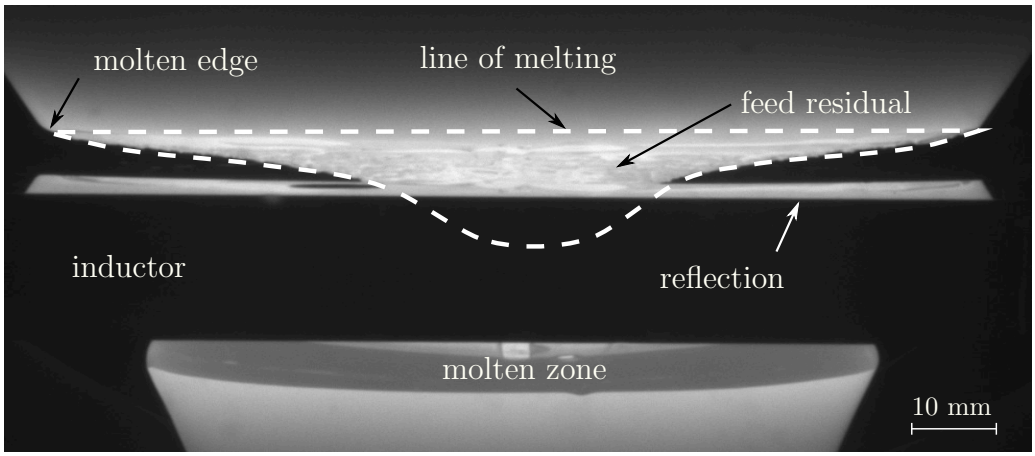

Figure 3.15.: Camera image of the feed material. Above the line of melting the feed rod is unaffected by the induction heater and directly below, a thin film of melt flows down along the solid feed residual into the molten zone. The white dashed line indicates the complete feed residual consisting of visible and hidden part.

with the same inductor at the same FZ machine and identical feed rods. An interpolating function $V_{fr}(R_F)$

$$V_{fr}(R_F) = \begin{cases} 0 & \text{for } R_F \leq d_0 \\ \sum_{i=1}^{3} d_i (R_F - d_0)^i & \text{for } R_F > d_0 \end{cases} \tag{3.20}$$

(model parameters $d_0 = 5$ mm, $d_1 = 0$, $d_2 = 18.07$ mm and $d_3 = -0.087$) based on the average of three experiments is given.

For modeling the melt volume, the derivative $\dot{V}_{fr}$

$$\dot{V}_{fr}(R_F, \dot{R}_F) = \begin{cases} 0 & \text{for } R_F \leq d_0 \\ \dot{R}_F \sum_{i=1}^{3} i \cdot d_i \cdot (R_F - d_0)^{i-1} & \text{for } R_F > d_0 \end{cases} \tag{3.21}$$

is applied.

3.5. Limitations of the FZ Process

This section considers the trajectory limitations of the FZ process. A trajectory is a time-dependent set of process variables of a dynamic system, for instance the curve of the crystal angle or the melt neck. FZ limitations are important for the stability of the process and for growing dislocation-free crystals.

For a dislocation-free growth of a crystal, an upper limit exists for the crystal pull rate. Based on the heat balance, Billig [Bil55] determined the theoretical

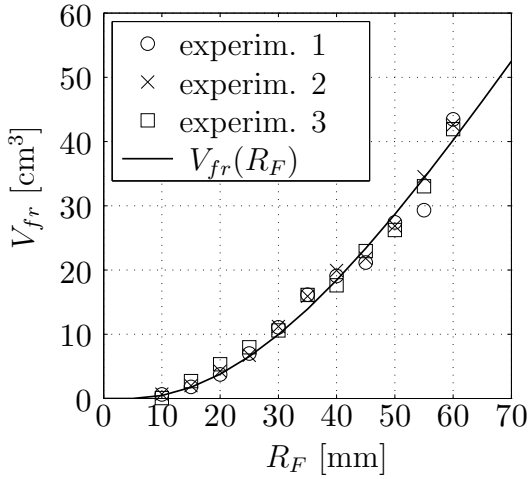

Figure 3.16.: Volume V_{fr} of the feed residual over feed radius R_F for three experiments. A function $V_{fr}(R_F)$ is plotted to interpolate the values (see equation 3.20).

maximum of the crystal pull rate

$$v_{C,max} = \frac{1}{q_0 \rho_S} \sqrt{\frac{2\epsilon\sigma\lambda_m T_m^5}{3R_C}} \tag{3.22}$$

where q_0 is the latent heat, ρ_S the density of the solid, ϵ the emissivity, σ the Stefan-Boltzmann constant, T_m the melting temperature, R_C the crystal radius, and λ_m the thermal conductivity in the solid at melting temperature. In the stationary case, the crystal pull rate v_C and the crystallization rate v_{Cr} are equal. Billig assumed a flat crystallization interface, only radiative heat loss, cold surroundings, and a temperature-independent surface emissivity. The theoretical maximum was validated with experimental investigations for different diameters by Lüdge et al. [Lüd02]. The investigations suggest that for crystals up to 125 mm in diameter, maximum growth rates of 80 % of the theoretical values are realistic. Table 3.4 shows the obtained maximum of the growth rates. The review by Lüdge et al. shows that the crystal pull rate influences the deflection of the crystallization interface.

The upper limitation for the melt neck is the inductor hole, especially in the needle-eye FZ techniques. If the melt touches the inductor, a short-circuit fault arises and the FZ machine could be damaged. Furthermore, vibrations and pulsations could appear in the melt for a larger melt neck, which disturbs the dislocation-free growth of the crystal. A lower limitation of the melt neck is the higher probability of disturbed feed melting for a thinner melt neck. Here, solid rings could arise, retaining the produced melt at the feed rod. These liquid reservoirs release melt stepwise when the solid rings are melted off. That results in a pulsating melt and could have a negative effect on the dislocation-free growth. In the worst case, a pulsating melt could lead to a

crystal diameter [mm]	max crystal pull rates $v_{C,max}$ (experiment) [mm/min]	(Billig) [mm/min]
7	16.0	18.9
11	12.0	15.1
25	9.0	10.1
50	6.0	7.1
67	5.0	6.1
100	4.1	5.0
125	3.8	4.5
147	2.8	4.1
150	2.7	4.1

Table 3.4.: Maximum crystal pull rates $v_{C,max}$ of growing dislocation-free silicon crystals obtained by experiments (see Lüdge et al. [Lüd02]) and the theoretical values after Billig [Bil55].

melt detachment from the feed rod, too. Figure 3.17 shows a solid ring at the melt neck.

Cone contour (defined by crystal angle) and height of the molten zone have to be chosen carefully. Forcing unfavorable quantities could create negative growth condition. Worst case are the creation of dislocations or bulge formation at the crystal with a high risk of melt leakage (as shown in figure 3.18).

The possible size of the molten zone is a further limiting factor of the process. It is determined by the equilibrium between the capillary forces of surface tension and the hydrostatic pressure of the melt. The maximum height of the melt shape is calculated by Heywang [Hey56] under the condition that only surface tension and gravity are acting. The crystal diameter becomes independent of the maximum zone height L_{max} for diameters approximately twice the maximum zone height or more:

$$L_{max} = 2.84\sqrt{\frac{\gamma}{\rho_M g}} \tag{3.23}$$

$$\approx 2\alpha \qquad \text{with } \alpha = \sqrt{\frac{2\gamma}{\rho_M g}} \tag{3.24}$$

where γ is the surface tension of the melt, ρ the density of the melt, g the gravity acceleration, and α the capillary constant. The factor 2.84 in equation 3.23 may slightly vary between 2.62 and 3.18 according to other theoretical approaches (see Bohm et al. [Boh94], p. 219). Silicon has a capillary constant of $\alpha_{Si} = 7.94$ mm. According to Heywang, a molten zone of silicon has a L_{max} of approximately 16 mm for crystals with diameters larger than 32 mm.

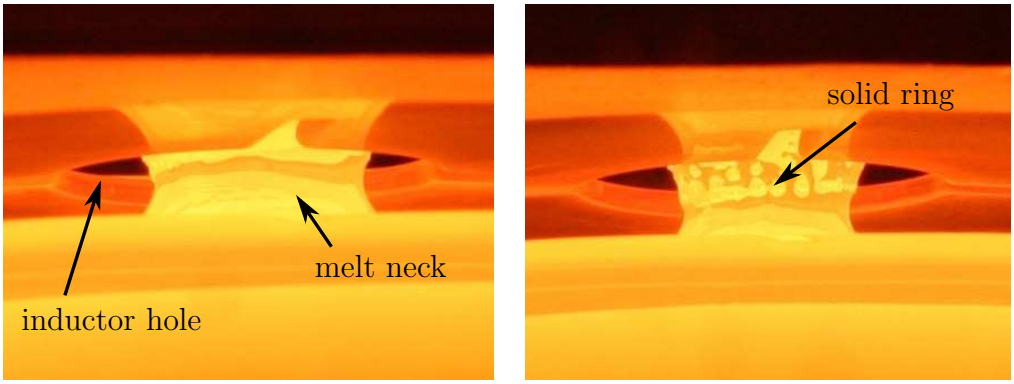

(a) (b)

Figure 3.17.: Images of melt neck and inductor hole. On the left side (a), the melt neck with suitable diameter. On the right side (b), the small melt neck with solid ring. The solid ring retains the melt flow and a liquid reservoir appears above the ring.

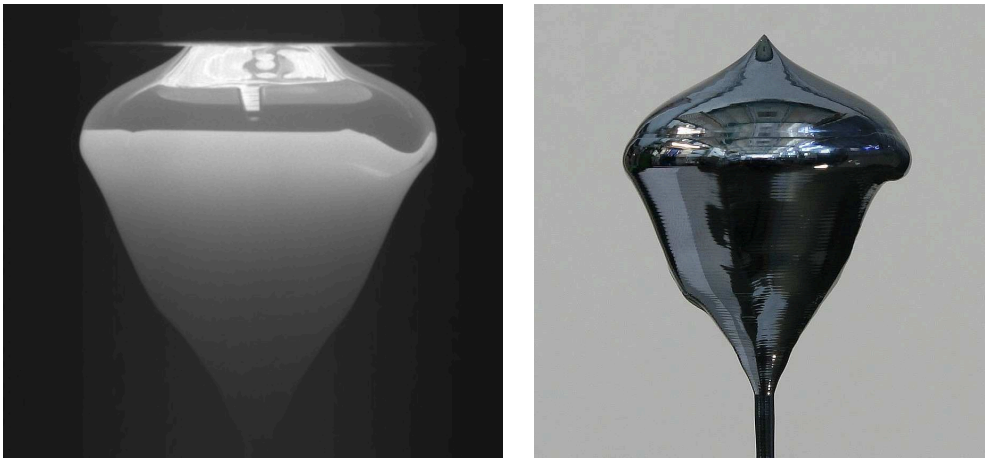

(a) Image of the growing crystal captured by the lower camera of the measurement system

(b) Image of the crystal

Figure 3.18.: Crystal with bulge formation resulting in a high risk of melt leakage. Growing crystal during the process (a) and image of the crystal after process stop (b).

4. Modeling of the Floating Zone Process

This chapter presents the mathematical model of the FZ process based on physical conservation laws. The goal is to get a set of nonlinear differential equations of first order with respect to time, which predicts the fundamental behavior of the process dynamics without expensive and time-consuming calculations. Such a mathematical model would be applicable, among other things, for process analysis, model-based observation and applications of modern automatic control.

The deductions of all differential equations are given and compared with experimental data. The equations are coupled with other model equations and model parameters are introduced to fit the experimental data. If possible, these model parameters are separately identified by using just the corresponding equation. Figures are given to compare the measurements with the results from solving the differential equations. In addition, examples of predictions obtained by numerical integration are shown to verify the model. Derivatives of the measurements are numerically calculated.

The measurements are disturbed by noise and measuring problems. Numerical differentiation of noisy signals could provide inaccurate values. A piece-wise cubic spline filter can be applied to reduce the noise of the measurements without introducing time delay (compared to low-pass filtering). These filtered measurements are to be considered as approximations of the true values of the process variables.

4.1. Low-Order Model of the Floating Zone Process

In this section a nonlinear equation set is evolved, which describes the dynamical behavior of the FZ process considering the fundamental physical aspects in the mathematical form

$$\dot{\underline{x}}(t) = f(t, \underline{x}(t), \underline{u}(t), \underline{\Theta}) \quad \text{with } \underline{x}(0) = \underline{x}_0 \qquad . \tag{4.1}$$

For a given initial state $\underline{x}_0$ and a given sequence of inputs $\underline{u}(t)$, the future run of the state vector $\underline{x}(t)$ can be calculated by using a numerical integration (for instance Runge-Kutta 4th order) of the state derivatives $\dot{\underline{x}}(t)$. The elements of the parameter vector $\underline{\Theta}$ represent the model parameters. Figure 4.1 shows a sketch of the FZ process in the cone phase. The solid feed rod and the growing crystal are held by respective holders. The position of the inductor is fixed and the pull rates of the feed holder v_F and the crystal holder v_C

$$v_F = -\frac{d}{dt}(H_F) \qquad , \tag{4.2}$$

$$v_C = \frac{d}{dt}(H_C) \tag{4.3}$$

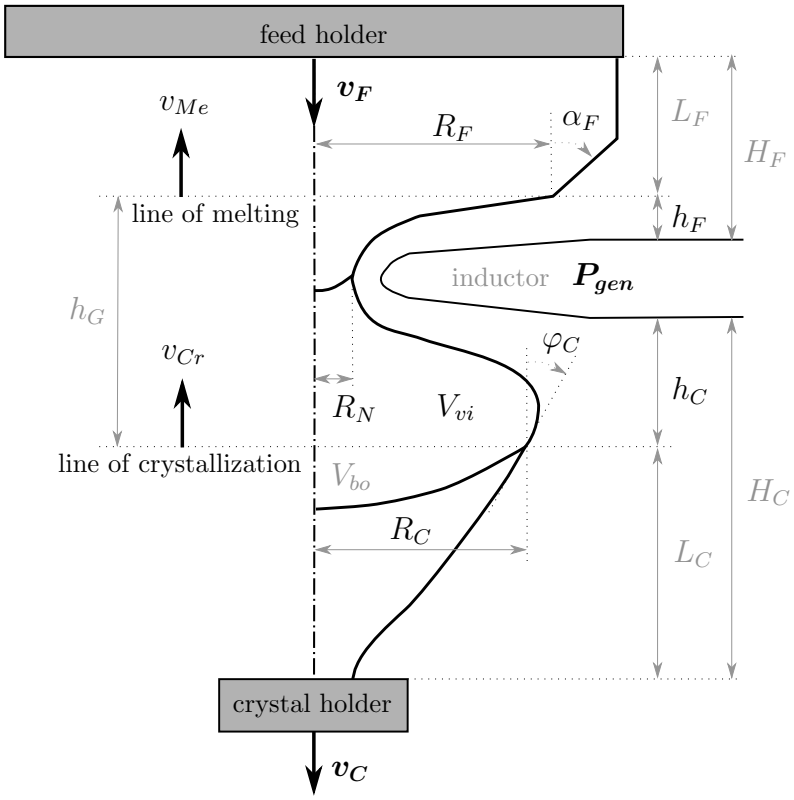

Figure 4.1.: Sketch of the floating zone process in the cone phase. Input variables: generator power P_{gen}, pull rates of the feed v_F and the crystal v_C. State variables: feed radius R_F, angle α_F at the feed rod, height h_F of the upper zone, melting rate v_{Me}, crystal radius R_C, crystal angle φ_C, height h_C of the lower zone, crystallization rate v_{Cr}, volume V_{vi} of the visible melt, radius R_N of the melt neck. Auxiliary variables: volume V_{bo} of the melt bowl, height h_G of the full zone, feed length L_F, distance H_F from feed holder to inductor top, crystal length L_C, distance H_C from crystal holder to inductor bottom.

are adjustable by the operator. The melt volume V_{melt}, established by the generator power P_{gen}, rests between feed rod and crystal. It consists of two parts: the visible melt volume V_{vi} and the volume V_{bo} of the melt bowl, which is covered by the crystal surface. The inductor covers a region at the upper part of the molten zone. This small part is hidden for the measurement system, but it can be assumed to be constant. Therefore, it is neglected concerning the dynamic process model. The line of melting is the horizontal line dividing the solid feed rod from the open melting front. Below the line of melting, it is assumed that a thin film of melt flows along the open melting front down into the melt. The temporal change of the feed length L_F is the melting rate v_{Me}

$$v_{Me} = -\frac{d}{dt}(L_F) \qquad . \tag{4.4}$$

In other words, the melting rate v_{Me} is the velocity of the line of melting with respect to the feed holder. A positive melting rate v_{Me} means a decreasing feed length. The angle at the feed shape according to the vertical axis, directly measured above the line of melting, is the feed angle α_F. The upper zone height h_F is the distance between the top of the inductor and the line of melting. The distance between the inductor bottom and the line of crystallization is defined as the lower zone height h_C. The distance between the lines of melting and crystallization is the height of the full zone h_G. The crystallization rate v_{Cr}

$$v_{Cr} = \frac{d}{dt}(L_C) \tag{4.5}$$

is the temporal change of the crystal length L_C on one hand and the velocity of the line of crystallization with respect to the crystal holder on the other hand. In the literature, the crystallization rate is also denoted as the growth rate. The melting and the crystallization rates have the physical unit length per time. In the FZ language the rates are often expressed in mm per minute. In this thesis, the melting rate v_{Me} and crystallization rate v_{Cr} are considered to be state variables. In section 4.1.7 equations are given to model the rates as functions of other states and input variables.

The visible shape of the melt is called the free melt surface. The angle at the crystal shape according to the vertical axis, directly measured at the line of crystallization, is the crystal angle φ_C. The modeled FZ process is adjustable by the generator power P_{gen} and the pull rates of feed v_F and crystal v_C. The rotation of feed rod and crystal is not included in the model. Some figures with experimental data show the feed rod diameter $D_F = 2R_F$ and the crystal diameter $D_C = 2R_C$ instead of the corresponding radii.

For the dynamic model, differential equations with respect to time are needed for the state vector $\underline{x}$ with its components:

- radius of the feed rod R_F,

- radius of the crystal R_C,
- height of the upper zone h_F,
- height of the lower zone h_C,
- angle at the feed α_F,
- angle at the crystal φ_C,
- volume of the visible melt V_{vi},
- radius of the melt neck R_N,
- crystallization rate v_{Cr},
- melting rate v_{Me},
- inductor power P_{ind}.

The state equations include one or more components of the state vector $\underline{x}$ and/or the input vector $\underline{u}$:

- generator power P_{gen},
- pull rate of the feed v_F,
- pull rate of the crystal v_C.

The low-order model is summarized in section 4.2 on page 84.

4.1.1. Modeling the Heights of Upper and Lower Zone

To get a relation between the zone height and other states or input variables, a different expression of the height is used. As shown in figure 4.1, the upper zone height h_F

$$h_F = H_F - L_F \tag{4.6}$$

is the difference between H_F (distance from feed holder to inductor top) and L_F (length of the feed). The derivative of the equation $h_F = H_F - L_F$ gives the differential equation of the upper zone height h_F

$$\frac{d}{dt}(h_F) = \underbrace{\frac{d}{dt}(H_F)}_{=-v_F} - \underbrace{\frac{d}{dt}(L_F)}_{=-v_{Me}} = v_{Me} - v_F \tag{4.7}$$

involving the melting rate v_{Me} and the pull rate of the feed v_F. This equation means, the change of the upper zone height h_F depends on the input variable v_F and the state v_{Me}. Among others, the melting rate v_{Me} can be influenced by the generator power P_{gen}. This analogously applies to the height $h_C = H_C - L_C$ of the lower zone. The derivative provides the equation

$$\frac{d}{dt}(h_C) = \underbrace{\frac{d}{dt}(H_C)}_{=v_C} - \underbrace{\frac{d}{dt}(L_C)}_{=v_{Cr}} = v_C - v_{Cr} \quad . \tag{4.8}$$

Here h_C is the lower zone height, v_{Cr} the crystallization rate, v_C the pull rate of the crystal, L_C the length of the crystal and H_C the distance between crystal holder and inductor bottom.

In the stationary case, where the zone heights are constant, the values for melting rate v_{Me} and pull rate v_F of the feed are equal. The crystallization rate v_{Cr} equals the pull rate v_C, too.

4.1.2. Modeling the Radii of Feed and Crystal

In this section, two differential equations are developed to describe the dynamics of feed radius R_F and crystal radius R_C. According to the triangle in figure 4.2 (a), the relationships $dR_F/dL_F = -tan(\alpha_F)$ and $dL_F = -v_{Me} \cdot dt$ (see equation 4.4) lead to the following differential equation

$$\frac{d}{dt}(R_F) = v_{Me} \cdot tan(\alpha_F) \qquad , \tag{4.9}$$

where R_F is the feed radius, v_{Me} the melting rate, and α_F the feed angle.

Considering the triangle in figure 4.2 (b), the relationships $dR_C = dL_C \cdot tan(\varphi_C)$ and $dL_C = v_{Cr} \cdot dt$ (see equation 4.5) provide the well known differential equation

$$\frac{d}{dt}(R_C) = v_{Cr} \cdot tan(\varphi_C) \tag{4.10}$$

including the crystal radius R_C, the crystallization rate v_{Cr}, and the crystal angle φ_C. The angles φ_F and φ_C in the triangles in figure 4.2 can be assumed as constant in terms of an infinitesimal consideration.

The growth angle φ_G is defined by

$$\varphi_G = \varphi_M - \varphi_C \tag{4.11}$$

with φ_M being the melt angle and φ_C the crystal angle. Theoretically, the melt angle φ_M equals a non-zero growth angle φ_G for the cylindrical growth ($\dot{R}_C = 0$ and $\varphi_C = 0$) (see Wünscher [Wün11c]).

Practically, the measurement system captures a melt angle of $\varphi_M = 0$ in the cylinder phase. Therefore, the growth angle φ_G is neglected for control issues in this thesis, and it is assumed that the melt angle φ_M equals the crystal angle φ_C,

$$\varphi_M = \varphi_C \qquad . \tag{4.12}$$

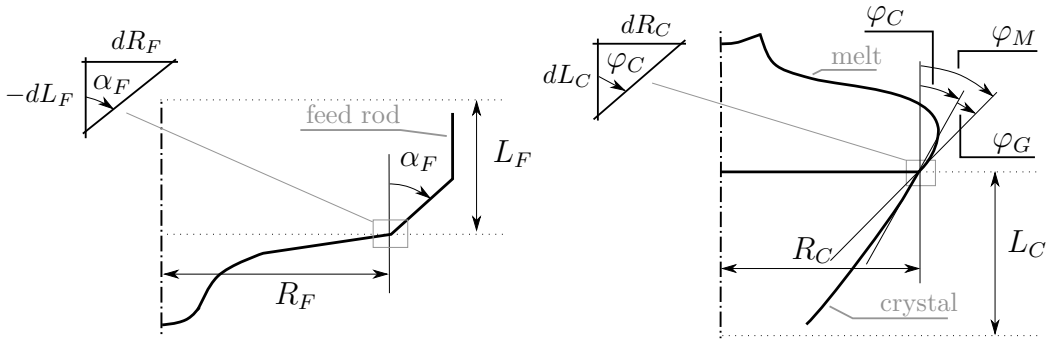

(a) Feed rod (b) Crystal and molten zone

Figure 4.2.: (a) - Sketch of the feed angle in the cone phase. (b) - Sketch of melt, crystal and growth angle in the cone phase. Crystal radius R_C, feed radius R_F, crystal angle φ_C, melt angle φ_M, growth angle φ_G, feed angle α_F, crystal length L_C, feed length L_F.

Comparison to Experimental Data

Figure 4.3 compares the model equation 4.9, $\dot{R}_F = v_{Me} \cdot tan(\alpha_F)$ (thin line), with experimental data (thick line). This is done for the thin neck phase (a) and the cone phase (b) to verify that the dynamics of the radius model fits the experiment. The derivative $\dot{R}_F$ (above) and the prediction of the feed radius R_F (below) are shown having been obtained by numerical integration of the differential equation 4.9. The measured radius R_F at the time point $t = 0$ is the initial value for the numerical integration. The values for the melting rate v_{Me} and the feed rod angle α_F are received from measurements. The feed angle α_F is directly measured and the melting rate v_{Me} is obtained by the model equation 4.7, $v_{Me} = v_F + \dot{h}_F$, using the input values of the feed pull rate v_F and the numerical differentiation $\dot{h}_F$ of the measured zone height. As shown in figure 4.3 (a) and (b), the model of the feed radius reflects the experimental dynamics in the thin neck phase and in the cone phase. The difference of approximately 4 mm between the model prediction for a process duration of 45 minutes and the measurements in the cone phase is acceptable. For the model predictive control, a prediction horizon of 2-10 minutes is used. Analogously, in figure 4.4, a comparison is shown between the model of the crystal radius R_C as well as its numerical differentiation $\dot{R}_C$ (dashed line) and experimental data (solid line). The differences in the thin neck phase primarily results from measuring problems of the crystal angle φ_C due to the small crystal diameter and the reduced brightness (see section 3.2). Another reason is an observed asymmetry of the crystal concerning the inductor hole. In that phase the camera system measures different angles at the left and the right side of the crystal being the result of the horizontal displacement between the axis of the crystal and the center of the inductor hole (see section 3.1). However, the curve of $\dot{R}_C$ correctly reflects the dynamics of the experiment in the thin neck and in the cone phase.

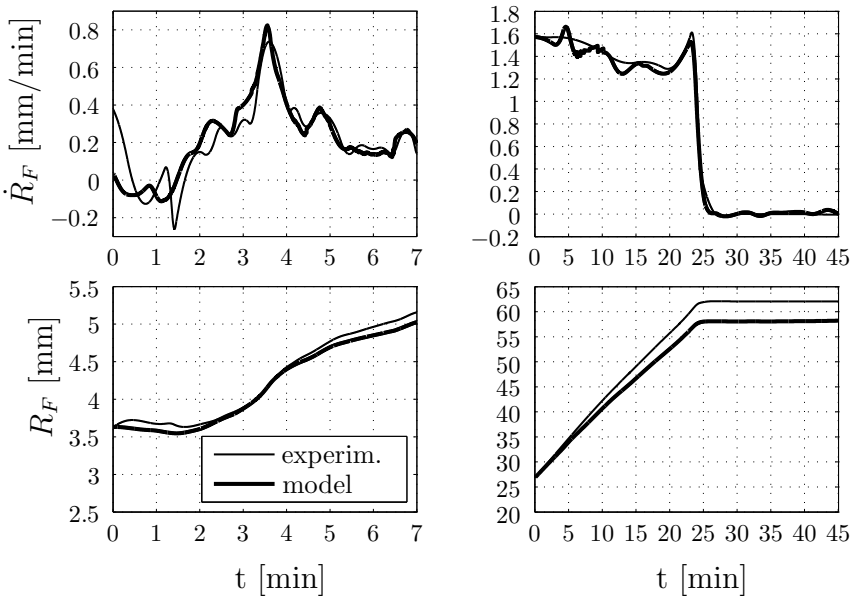

(a) Thin neck phase (experiment 1). (b) Cone phase (experiment 2).

Figure 4.3.: Comparison between the feed radius R_F and its numerical differentiation $\dot{R}_F$ of two experiments (thin line) and the prediction based on the model equation 4.9 (thick line). The melting rate v_{Me} and the feed rod angle α_F are experimental data.

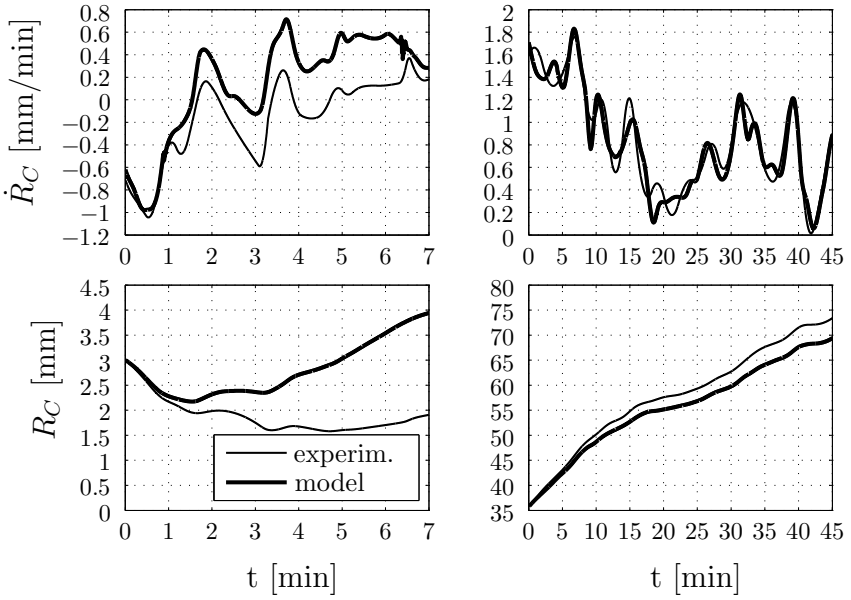

(a) Thin neck phase (experiment 1). (b) Cone phase (experiment 2).

Figure 4.4.: Comparison between the crystal radius R_C and its numerical differentiation $\dot{R}_C$ of two experiments (thin line) and the prediction based on the model equation 4.10 (thick line). The crystallization rate v_{Cr} and the crystal angle φ_C are experimental data.

4.1.3. Modeling the Feed Angle

The angle α_F at the feed rod is independent of other state and input variables. The angle only depends on the shape of the feed rod. Assuming a constant feed angle α_F, the following differential equation can be used:

$$\frac{d}{dt}(\alpha_F) = 0 \qquad . \tag{4.13}$$

The angle α_F is considered as a system state, because it is an estimated value in the Kalman filter to reduce the measurement noise.

4.1.4. Modeling the Melt Neck

The coupling of the melt neck R_N to other states is analyzed in this section. Based on experimental experiences, the melt neck R_N is influenced by the inductor power. The following experiment was performed to find a relationship. The inductor power is increased in a continuous way in the cylinder phase of a crystal of 100 mm in diameter. As shown in figure 4.5, the relationship between the melt neck R_N and the height h_G of the full zone is approximately linear. This linear behavior is obtained in the cylinder phase. Experimental data has shown that this relationship is also valid in the cone phase for a crystal radius R_C with more than approximately 20 mm. According to the model-based control of the FZ process, the melt neck R_N plays a roll only for crystals with a radius larger than 20 mm. The following equation

$$\frac{d}{dt}(R_N) = \begin{cases} 0 & \text{for } R_C \leq 20 \text{ mm} \\ n_h(\dot{h}_F + \dot{h}_C) & \text{for } R_C > 20 \text{ mm} \end{cases} \tag{4.14}$$

is applied with the model parameter $n_h = -0.9$. The behavior is not modeled for R_C smaller than 20 mm. Modeling of the dynamics for smaller radii could be a task for future works.

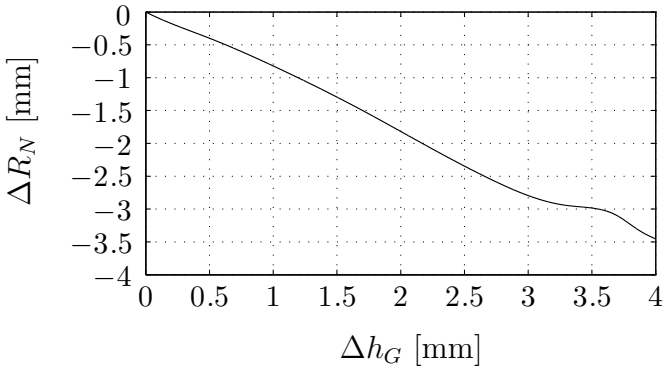

Figure 4.5.: Measured relationship between the changes of the height Δh_G of the full zone and the melt neck ΔR_N in the cylinder phase of a crystal of 100 mm in diameter.

4.1.5. Modeling the Melt Volume

This section provides an approach to describe the dynamics of the melt mass and the melt volume. Figure 4.6 shows a sketch of the molten zone. A thin film of melt flows along the surface of the solid feed residual (open melting front) into the molten zone and increases the melt mass. The melt mass m_{melt}

$$m_{melt} = m_{vi} + m_{bo} \tag{4.15}$$

consists of the visible melt mass m_{vi} and the melt bowl m_{bo}. The derivative of the melt mass

$$\frac{d}{dt}(m_{melt}) = \frac{d}{dt}(m_{vi}) + \frac{d}{dt}(m_{bo}) \tag{4.16}$$

can be alternatively expressed by the incoming and outgoing flow terms

$$\frac{d}{dt}(m_{melt}) = -\dot{m}_F - \dot{m}_C \quad , \tag{4.17}$$

where $\dot{m}_F$ is the change of the feed mass (because of melting) and $\dot{m}_C$ the change of the crystal mass (because of crystallization). It has to be considered that a negative change of the feed mass m_F increases the melt mass m_{melt}. Therefore, the minus sign before $\dot{m}_F$ is necessary. In other words, $-\dot{m}_F$ describes the flow of the melting mass from the feed rod into the molten zone and $\dot{m}_C$ that of the solidified mass into the crystal.

The derivative of the visible melt mass follows from equation 4.16 and 4.17

$$\underbrace{\frac{d}{dt}(m_{vi})}_{\rho_M \dot{V}_{vi}} = -\dot{m}_F - \dot{m}_C - \underbrace{\frac{d}{dt}(m_{bo})}_{\rho_M \dot{V}_{bo}} \tag{4.18}$$

and the derivative $\dot{V}_{vi}$ of the visible melt volume is

$$\rho_M \dot{V}_{vi} = -\dot{m}_F - \dot{m}_C - \rho_M \dot{V}_{bo} \quad , \tag{4.19}$$

where ρ_M is the density of the melt, $\dot{m}_F$ the change of the feed mass, $\dot{m}_C$ the change of the crystal mass and $\dot{V}_{bo}$ the derivative of the melt bowl volume.

Considering the infinitesimal change of the mass, provides equations for the calculation of $\dot{m}_F$ and $\dot{m}_C$. In a first approach, the influences on the mass balance of feed residual and melt bowl are neglected. This can be assumed in the thin neck phase. Afterwards, the equations are extended with corresponding terms to achieve suitable formulations for the cone phase.

As shown in figure 4.7, the infinitesimal change of the solid feed mass $dm_{F,1}$ above the line of melting can be calculated using the volume calculation of a

cone frustum (see equation A.33):

$$dm_{F,1} = \rho_S \frac{\pi\ dL_F}{3}\Big(R_F^2 + R_F(R_F + dR_F) + (R_F + dR_F)^2\Big) \tag{4.20}$$

$$= \rho_S \pi R_F^2 dL_F \quad . \tag{4.21}$$

Terms of higher order such as dR_F^2 are assumed to be zero. The term $dm_{F,1}$ describes only the change of the feed mass above the line of melting. Additionally considering the influence of the feed residual provides the formula

$$dm_F = \rho_S(\pi R_F^2 dL_F + dV_{fr}) \quad , \tag{4.22}$$

where dL_F is the change of the feed length, dV_{fr} the change of the solid feed residual, ρ_S the solid density and R_F the feed radius at the line of melting.

The derivative $\dot{m}_F$ of the feed material follows from equations 4.22 and 4.4 ($dL_F = -v_{Me}\ dt$):

$$\dot{m}_F = \rho_S(\dot{V}_{fr} - \pi R_F^2 v_{Me}) \quad . \tag{4.23}$$

Analogously, the infinitesimal change of the crystal mass can be formulated as

$$dm_C = \rho_S(\pi R_C^2 dL_C - dV_{bo}) \quad , \tag{4.24}$$

where dL_C is the change of the crystal length, dV_{bo} the change of the melt bowl volume, ρ_S the solid density and R_C the crystal radius.

The derivative $\dot{m}_C$ of the crystallizing material follows from equations 4.24 and 4.5 ($dL_C = v_{Cr} \cdot dt$)

$$\dot{m}_C = \rho_S(\pi R_C^2 v_{Cr} - \dot{V}_{bo}) \quad . \tag{4.25}$$

Considering equations 4.19, 4.23, and 4.25, the differential equation for modeling the visible melt volume V_{vi} is obtained

$$\rho_M \frac{d}{dt}(V_{vi}) = \rho_S(\pi R_F^2 v_{Me} - \dot{V}_{fr}) - \rho_S \pi R_C^2 v_{Cr} - (\rho_M - \rho_S)\dot{V}_{bo} \quad . \tag{4.26}$$

Approximations for the derivatives of feed residual and melt bowl, $\dot{V}_{fr} = f(R_F, \dot{R}_F)$ and $\dot{V}_{bo} = f(R_C, \dot{R}_C)$ are developed in sections 3.3 and 3.4. It is worth to introduce the model parameters a_{fr} and a_{bo}

$$\rho_M \frac{d}{dt}(V_{vi}) = \rho_S(\pi R_F^2 v_{Me} - a_{fr}\dot{V}_{fr}) - \rho_S \pi R_C^2 v_{Cr} - (\rho_M - \rho_S)a_{bo}\dot{V}_{bo} \tag{4.27}$$

to overcome approximation inaccuracies and to fit the derivative of the visible melt volume V_{vi} to experimental data. Within the thin neck phase, the volume

derivatives of feed residual V_{fr} and melt bowl V_{bo} are zero.

The relation

$$R_F^2 v_F = R_C^2 v_C \tag{4.28}$$

holds for stationary growth conditions ($\dot{V}_{vi} = 0$, $\dot{V}_{fr} = 0$, $\dot{V}_{bo} = 0$, $v_{Me} = v_F$ and $v_{Cr} = v_C$). That means, the stationary crystal radius R_C only depends on the stationary feed radius R_F, the feed pull rate v_F, and the crystal pull rate v_C.

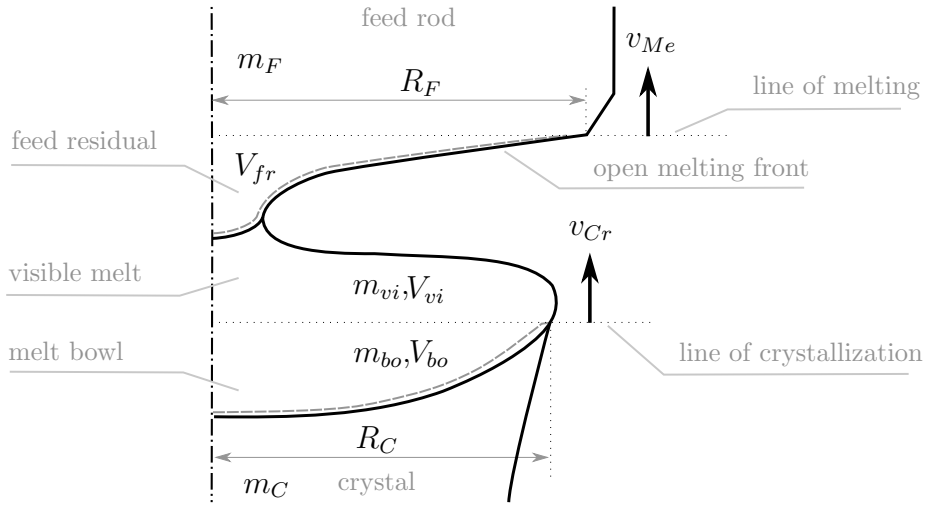

Figure 4.6.: Sketch of the molten zone (radius of the feed R_F, melting rate v_{Me}, radius of the crystal R_C, crystallization rate v_{Cr}, mass of the visible melt m_{vi}, mass of melt bowl m_{bo}, volume of the feed residual V_{fr}, volume of the visible melt V_{vi}, volume of melt bowl V_{bo}, feed mass m_F, crystal mass m_C).

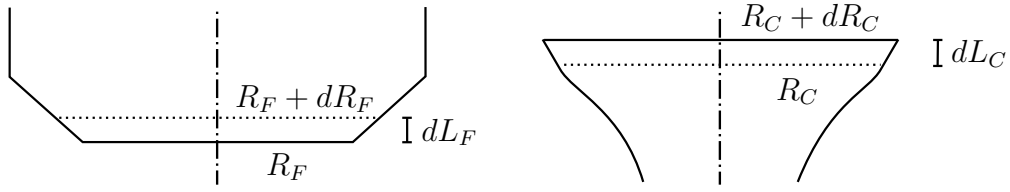

(a) Feed rod (b) Crystal

Figure 4.7.: Sketch of mass balance for feed rod (a) and crystal (b). The influence of feed residual and melt bowl is neglected. R_F is the feed radius, R_C the crystal radius, dL_F and dL_C the infinitesimal change of the length of feed rod and crystal.

Comparison to Experimental Data

Figure 4.8 shows the comparison between the model prediction and two experiments. The visible volume V_{vi} is obtained by numerical integration of equation 4.27 by using experimental data of the radii R_F and R_C of feed and crystal, and the rates v_{Me} and v_{Cr} of melting and crystallizing. Equations 3.19 and 3.21 are applied to calculate the volume derivatives of melt bowl $\dot{V}_{bo}$ and feed residual $\dot{V}_{fr}$. Two model predictions are shown to demonstrate the essential influence of $\dot{V}_{fr}$ and $\dot{V}_{bo}$. The parameters a_{fr} and a_{bo} in model 1 are adjusted to fit the measurements. The two parameter are assumed to be identical to keep the parameters simple. A value of $a_{fr} = a_{bo} = 1.35$ is obtained. Model 2 neglects the volumes of feed residual and melt bowl ($a_{fr} = a_{bo} = 0$). As shown in figure 4.8, the model reflects the dynamics of the experiments in the thin neck phase and in the cone phase.

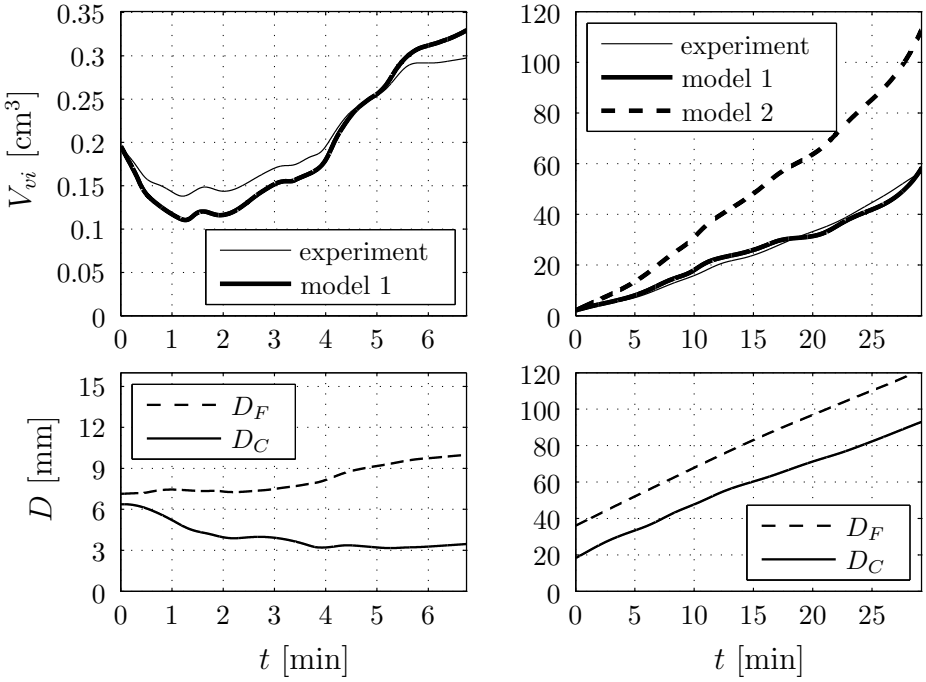

(a) Experiment 1: thin neck phase

(b) Experiment 2: cone phase

Figure 4.8.: Model validation of the visible melt volume V_{vi} by using equation 4.27. Crystal diameter D_C, feed diameter D_F, melting rate v_{Me} and crystallization rate v_{Cr} are experimental data. The parameters $a_{fr} = a_{bo} = 1.35$ are used in model 1 to fit the data. The influences of feed residual and melt bowl ($a_{fr} = 0$, $a_{bo} = 0$) are neglected in model 2.

4.1.6. Modeling the Melt Angle

Modeling the dynamics of the melt angle φ_M is a complex issue. Nevertheless, a model equation is required because the melt angle $\varphi_M = \varphi_C$ is included in the differential equation 4.10 of the derivative $\dot{R}_C$ of the crystal radius. The melt angle φ_M is defined as the angle of the melt shape at the solid-liquid interface with respect to the vertical axis (see figure 4.2 (b), page 63). The melt shape can be calculated by solving the Laplace-Young equation (see Coriell and Cordes [Cor77]), which describes the force equilibrium of a point on a melt drop

$$\underbrace{P_0}_{\substack{\text{pressure}\\ \text{difference}}} - \underbrace{\rho_M g z}_{\substack{\text{hydrostatic}\\ \text{pressure}}} + \underbrace{\frac{1}{2}\rho_M r^2 \Omega^2}_{\substack{\text{centrifugal}\\ \text{pressure}}} + \underbrace{F_n}_{\substack{\text{electro-}\\ \text{magnetic}\\ \text{pressure}}} = \underbrace{\gamma \cdot K}_{\substack{\text{capillary}\\ \text{pressure}}} \tag{4.29}$$

including the pressure difference P_0 between a reference point in the melt and the ambient pressure, the melt density ρ_M, the gravitational acceleration g, the radial coordinate r, the vertical coordinate z, the rate of rotation Ω, the electromagnetic pressure F_n, the surface tension γ, and the curvature K.

Assuming rotational symmetry, equation 4.29 can be transformed into a system of three differential equations (see section A.2). The numerical integration of these differential equations gives the shape of the melt according to a start and a stop condition. The pressure difference P_0 is used to fit the calculated melt shape to a given reference point. This can be done by varying the pressure difference P_0 so that the melt shape hits the reference point. Wünscher uses that method to investigate the growth angle by comparing shape calculations with data from high-resolution images from experiments (see Wünscher [Wün11a] and [Wün11b]). Wünscher neglects the effect of rotation due to small influence on the solution, but he considers the electromagnetic pressure F_n calculated by the approximation of surface ring currents. The inductor geometry is required to calculate the electromagnetic pressure F_n, therefore, F_n is neglected in this investigations to keep the obtained dynamics simple. Due to Wünscher, this approximation is appropriate because of the low influence of F_n on the melt shape.

The following assumptions and conditions were made to calculate the shape of the melt:

- the melt shape has rotational symmetry and is stationary,
- the centrifugal and electromagnetic pressure F_n are neglected, to keep the calculation simple,
- the start condition s_i of the melt shape solution is defined by the melt angle φ_M and the crystal radius R_C,

- the stop condition s_t is defined by the vertical h_m and radial component r_m of a reference point.

Figure 4.9 shows a sketch of the shape of the molten zone including start s_i and stop condition s_t. Considering thin neck and cone phase, the stop condition $s_t = [r_m, h_m]$ is determined by different geometrical quantities. In the cone phase, s_t is equal to the position of the melt neck ($r_m = R_N$ and $h_m = h_C$). In the thin neck phase, no melt neck exists due to the small diameter of the feed rod and the non-existing feed residual. Here, s_t is equal to the position of the lower end of the feed rod ($r_m = R_F$ and $h_m = h_G$).

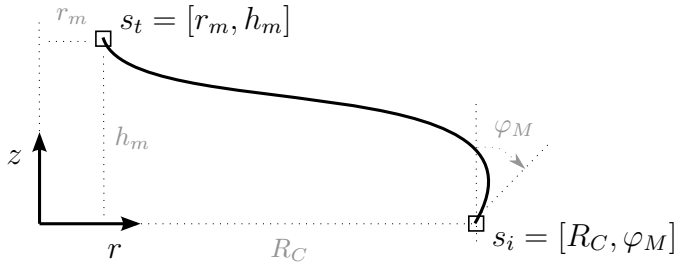

Figure 4.9.: Sketch of the shape of the molten zone including start s_i and stop condition s_t.

Based on the radial and vertical coordinates r_k and z_k of the melt shape, the visible melt volume V_{vi} can be approximated by the Riemann sum

$$V_{vi} \approx \sum_k \pi r_k^2 \cdot (z_{k+1} - z_k) \qquad . \tag{4.30}$$

Figure 4.10 shows two melt shapes obtained by numerically solving the Laplace-Young equation using reference points from experiments: (a) thin neck phase and (b) cone phase. In (a) the melt shape starts with a negative melt angle φ_M = -4.49° at crystal radius R_C of 2.21 mm. This will lead in a decreasing diameter. The molten zone has a height of h_G = 6.9 mm and ends at the feed rod with a radius R_F of 3.68 mm. In (b) the melt shape starts with a positive melt angle φ_M = 20.63° at crystal radius R_C of 34.94 mm. The stop condition of the shape is at h_C = 13.95 mm (height of the lower zone) and R_N = 10.68 mm (melt neck). A corresponding melt shape for the cylinder phase is similar to (b), only having a melt angle φ_M of zero.

Starting from the Laplace-Young equation, Landau derives an explicit formulation of the melt angle φ_M depending on the melt height h_m. His deduction is published in the book of Landau and Lifshitz [Lan87]. A half-plane with a constant melt height h_m at infinity is assumed (see figure A.4) and the relation between melt angle φ_M and melt height h_m is given by

$$\varphi_M = arcsin(\frac{h_m^2}{\alpha_{Si}^2} - 1) \tag{4.31}$$

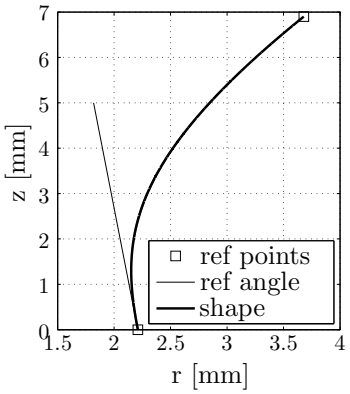

(a) Decreasing crystal radius in the thin neck phase. Crystal radius $R_C = 2.2$ mm, melt angle $\varphi_M = -4.5°$, height of the full zone $h_G = 6.9$ mm, and feed radius $R_F = 3.7$ mm.

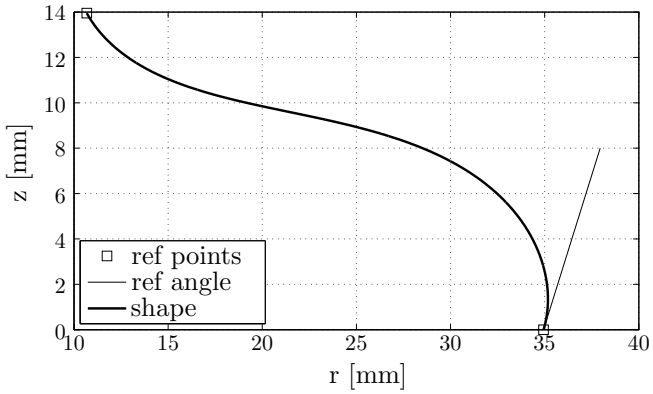

(b) Increasing crystal radius in the cone phase. Radius of the crystal $R_C = 34.94$ mm, melt angle $\varphi_M = 20.63°$, height of the lower zone $h_C = 13.95$ mm, and radius of the melt neck $R_N = 10.68$ mm.

Figure 4.10.: Calculated melt shapes by numerically solving the Laplace-Young equation. The centrifugal and electromagnetic pressures are neglected. Melt shape in thin neck phase (a) and cone phase (b) using reference points based on experimental data.

with the melt angle φ_M, the melt height h_m and the capillary constant[1] of silicon $\alpha_{Si} = 7.94$ mm. For large diameters, the melt height h_m can be approximately calculated by

$$h_m = \frac{V_{vi}}{\pi R_C^2} \tag{4.32}$$

from the visible melt volume V_{vi} and the crystal radius R_C. This equation is an approximation and usable for large diameters, but its accuracy is insufficient in the thin neck and at the beginning of the cone phase. A new approach is needed.

Total Derivative

It is obvious that the melt angle φ_M is coupled to the shape of the melt. Considering figure 4.10, the melt shape primarily depends on the melt volume, the melt height and the radii of bottom and top. Within the thin neck phase, it is assumed that the melt angle φ_M

$$\varphi_M = f(V_{vi}, R_C, h_G, R_F) \tag{4.33}$$

[1] The capillary constant is defined as $\alpha = \sqrt{\frac{2\gamma}{g\rho_M}}$, where γ is the surface tension of the melt, ρ_M the density of the melt, g the gravity acceleration

is a function of the visible melt volume V_{vi}, the crystal radius R_C, the full zone height h_G and the feed radius R_F. For the cone phase, it is assumed that the melt angle φ_M is a function of the visible melt volume V_{vi}, the crystal radius R_C, the height h_C of the lower zone and the radius R_N of the melt neck:

$$\varphi_M = f(V_{vi}, R_C, h_C, R_N) \qquad . \tag{4.34}$$

First, equation 4.34 is considered to describe the derivative $\dot{\varphi}_M$ of the melt angle during the cone phase. The reference values φ_M, R_C, h_C and R_N are known and available from several experiments. Based on these values, the melt shape is calculated by numerically solving the Laplace-Young equation with respect to the reference values.

The total derivative of equation 4.34

$$\begin{aligned} d\varphi_M(V_{vi}, R_C, h_C, R_N) = &\left.\frac{\partial \varphi_M}{\partial V_{vi}}\right|_{R_C,h_C,R_N} \cdot dV_{vi} + \left.\frac{\partial \varphi_M}{\partial R_C}\right|_{V_{vi},h_C,R_N} \cdot dR_C \\ &+ \left.\frac{\partial \varphi_M}{\partial h_C}\right|_{V_{vi},R_C,R_N} \cdot dh_C + \left.\frac{\partial \varphi_M}{\partial R_N}\right|_{V_{vi},R_C,h_C} \cdot dR_N \end{aligned} \tag{4.35}$$

being divided by dt

$$\begin{aligned} \frac{d}{dt}(\varphi_M) = &\left.\frac{\partial \varphi_M}{\partial V_{vi}}\right|_{R_C,h_C,R_N} \cdot \dot{V}_{vi} + \left.\frac{\partial \varphi_M}{\partial R_C}\right|_{V_{vi},h_C,R_N} \cdot \dot{R}_C \\ &+ \left.\frac{\partial \varphi_M}{\partial h_C}\right|_{V_{vi},R_C,R_N} \cdot \dot{h}_C + \left.\frac{\partial \varphi_M}{\partial R_N}\right|_{V_{vi},R_C,h_C} \cdot \dot{R}_N \end{aligned} \tag{4.36}$$

is used to describe the dynamic behavior of the melt angle φ_M as a superposition of four terms. The variables $\dot{V}_{vi}$, $\dot{R}_C$, $\dot{h}_C$ and $\dot{R}_N$ can be calculated by the differential equations 4.27, 4.10, 4.8, and 4.14. The numerical approximation by difference quotients will be used below to calculate the unknown partial derivatives. Each partial derivative depends on the combination of the variables V_{vi}, R_C, h_C, R_N, and φ_M.

The calculation of the complete five-dimensional field is complex and not all combinations are physically possible. It is obvious to choose reference points close to real measurements to get significant data and to ensure feasibility of the calculated melt shape. As shown in figure 4.11, the development of the quantities V_{vi}, h_C, R_N, and φ_M in a growth experiments can be approximated as functions of the crystal radius R_C. That means, for a specific value of crystal radius R_C, similar values of V_{vi}, h_C, R_N, and φ_M are obtained within different experiments. Therefore, it is assumed that the needed values of the partial derivatives are functions of the crystal radius R_C. Four correction factors a_V, a_R, a_h and a_N are introduced to handle the simplifications and to fit experimental data.

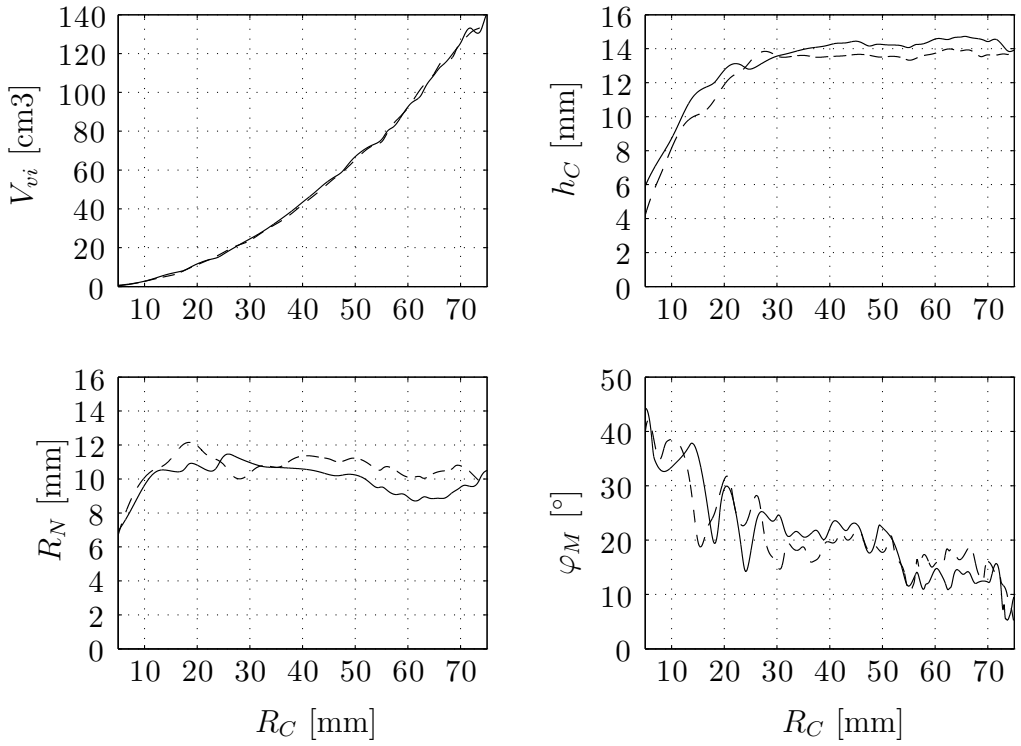

Figure 4.11.: Development of the quantities V_{vi}, h_C, R_N, and φ_M for two 6-inch experiments plotted over crystal radius R_C

Based on the approximation by difference quotients, the following relations

$$\left.\frac{\partial \varphi_M}{\partial V_{vi}}\right|_{R_C,h_C,R_N}(\varphi_M, R_C, V_{vi}, h_C, R_N) \approx a_V \left.\frac{\Delta \varphi_M}{\Delta V_{vi}}\right|_{R_C,h_C,R_N}(R_C), \tag{4.37}$$

$$\left.\frac{\partial \varphi_M}{\partial R_C}\right|_{V_{vi},h_C,R_N}(\varphi_M, R_C, V_{vi}, h_C, R_N) \approx a_R \left.\frac{\Delta \varphi_M}{\Delta R_C}\right|_{V_{vi},h_C,R_N}(R_C), \tag{4.38}$$

$$\left.\frac{\partial \varphi_M}{\partial h_C}\right|_{V_{vi},R_C,R_N}(\varphi_M, R_C, V_{vi}, h_C, R_N) \approx a_h \left.\frac{\Delta \varphi_M}{\Delta h_C}\right|_{V_{vi},R_C,R_N}(R_C), \tag{4.39}$$

$$\left.\frac{\partial \varphi_M}{\partial R_N}\right|_{V_{vi},R_C,h_C}(\varphi_M, R_C, V_{vi}, h_C, R_N) \approx a_N \left.\frac{\Delta \varphi_M}{\Delta R_N}\right|_{V_{vi},R_C,h_C}(R_C) \tag{4.40}$$

are used to obtain the partial derivatives. The following equation can be used to calculate the derivative of the melt angle φ_M

$$\begin{aligned}\frac{d}{dt}(\varphi_M) = a_V \frac{\Delta \varphi_M}{\Delta V_{vi}} \cdot \dot{V}_{vi} + a_R \frac{\Delta \varphi_M}{\Delta R_C} \cdot \dot{R}_C \\ + a_h \frac{\Delta \varphi_M}{\Delta h_C} \cdot \dot{h}_C + a_N \frac{\Delta \varphi_M}{\Delta R_N} \cdot \dot{R}_N\end{aligned} \tag{4.41}$$

in the cone phase. As mentioned in section 4.1.2, the melt angle φ_M and the

crystal angle φ_C can be assumed as being equal.

Calculation of $\Delta\varphi_M/\Delta V_{vi}$:

The difference quotient is estimated comparing two melt shapes having been obtained by solving the Laplace-Young equation. As shown in figure 4.12, the two shapes - the first one with the start point $s_i = (R_C, \varphi_M)$ and the second one with $s_i = (R_C, \varphi_M + \Delta\varphi_M)$ - are used to obtain the value of ΔV_{vi}. Both shapes use the same stop point $s_t = (R_N, h_C)$ as reference. The melt volumes $V_{vi,1}$ and $V_{vi,2}$ of the shapes are calculated by the Riemann sum (equation 4.30) under the assumption of rotational symmetry. The differential quotient is calculated by the formula:

$$\frac{\Delta\varphi_M}{\Delta V_{vi}} = \frac{\varphi_{M,2} - \varphi_{M,1}}{V_{vi,2} - V_{vi,1}} \quad . \tag{4.42}$$

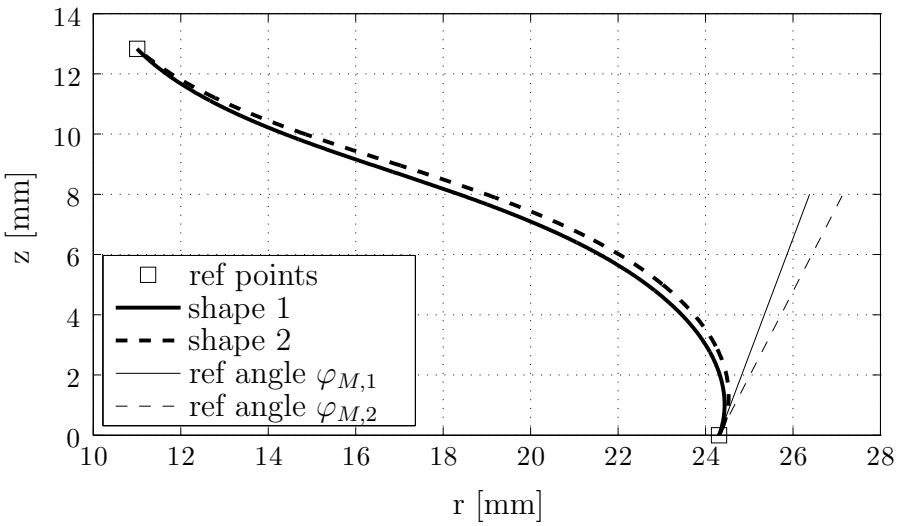

Figure 4.12.: Two melt shapes with different ref angles φ_M for calculating the difference quotient $\Delta\varphi_M/\Delta V_{vi}$ ($\Delta\varphi_M = \varphi_{M,2} - \varphi_{M,1}$ and $\Delta V_{vi} = V_{vi,2} - V_{vi,1}$).

Calculation of $\Delta\varphi_M/\Delta R_C$:

Here, the calculation of the difference quotient is more sophisticated due to the condition of constant melt volume V_{vi}.

The first shape starts with the condition $s_i = (R_C, \varphi_M)$ and the second one with $s_i = (R_C + \Delta R_C, \varphi_M + \Delta\varphi_M)$. Both shapes have the same stop condition $s_t = (R_N, h_C)$. ΔR_C is determined manually and $\Delta\varphi_M$ is varied by a numerical optimization algorithm so, that the melt volume V_{vi} of both shapes are equal. A least-squared objective function is used. The definition of the optimization

problem is

$$\Delta\varphi_{M,opt} = \underset{\Delta\varphi_M}{\arg\min} \left(V_{vi}(R_C, \varphi_M) - V_{vi}(R_C + \Delta R_C, \varphi_M + \Delta\varphi_M)\right)^2 \quad (4.43)$$

where $V_{vi}(R_C, \varphi_M)$ is the corresponding volume of the shape based on the condition R_C and φ_M. The differential quotient is calculated by the formula:

$$\frac{\Delta\varphi_M}{\Delta R_C} = \frac{\Delta\varphi_{M,opt}}{\Delta R_C} \quad . \quad (4.44)$$

Calculation of $\Delta\varphi_M/\Delta h_C$:

Analogously, Δh_C is determined manually and $\Delta\varphi_M$ is obtained by solving the optimization problem:

$$\underset{\Delta\varphi_M}{\arg\min} \left(V_{vi}(h_C, \varphi_M) - V_{vi}(h_C + \Delta h_C, \varphi_M + \Delta\varphi_M)\right)^2 \quad . \quad (4.45)$$

Calculation of $\Delta\varphi_M/\Delta R_N$:

Analogously, ΔR_N is determined manually and $\Delta\varphi_M$ is obtained by solving the optimization problem:

$$\underset{\Delta\varphi_M}{\arg\min} \left(V_{vi}(R_N, \varphi_M) - V_{vi}(R_N + \Delta R_N, \varphi_M + \Delta\varphi_M)\right)^2 \quad . \quad (4.46)$$

Figure 4.13 shows the obtained difference quotients for three different experiments. The mean average of the three experiments as function of the crystal radius R_C is drawn in gray and the corresponding values are listed in table 4.1. As expected, the dynamics of the melt angle φ_M is strongly coupled to the crystal radius R_C. All curves show a decreasing nonlinear influence in absolute terms for increasing crystal radius. The differential quotients obtained from the three experiments revealed a higher variance for smaller radii. Here, the approximation with a numerical calculation of the differential quotients results in a high variance.

Derivative of the melt angle in the thin neck phase:

Considering equation 4.33 and

$$\begin{aligned}\frac{d}{dt}(\varphi_M) = a_V \frac{\Delta\varphi_M}{\Delta V_{vi}} \cdot \dot{V}_{vi} + a_R \frac{\Delta\varphi_M}{\Delta R_C} \cdot \dot{R}_C \\ + a_h \frac{\Delta\varphi_M}{\Delta h_G} \cdot \dot{h}_G + a_N \frac{\Delta\varphi_M}{\Delta R_F} \cdot \dot{R}_F\end{aligned} \quad (4.47)$$

suitable for the thin neck phase, it is difficult to get an approximation of the difference quotients as function of R_C (such as shown in figure 4.13) with re-

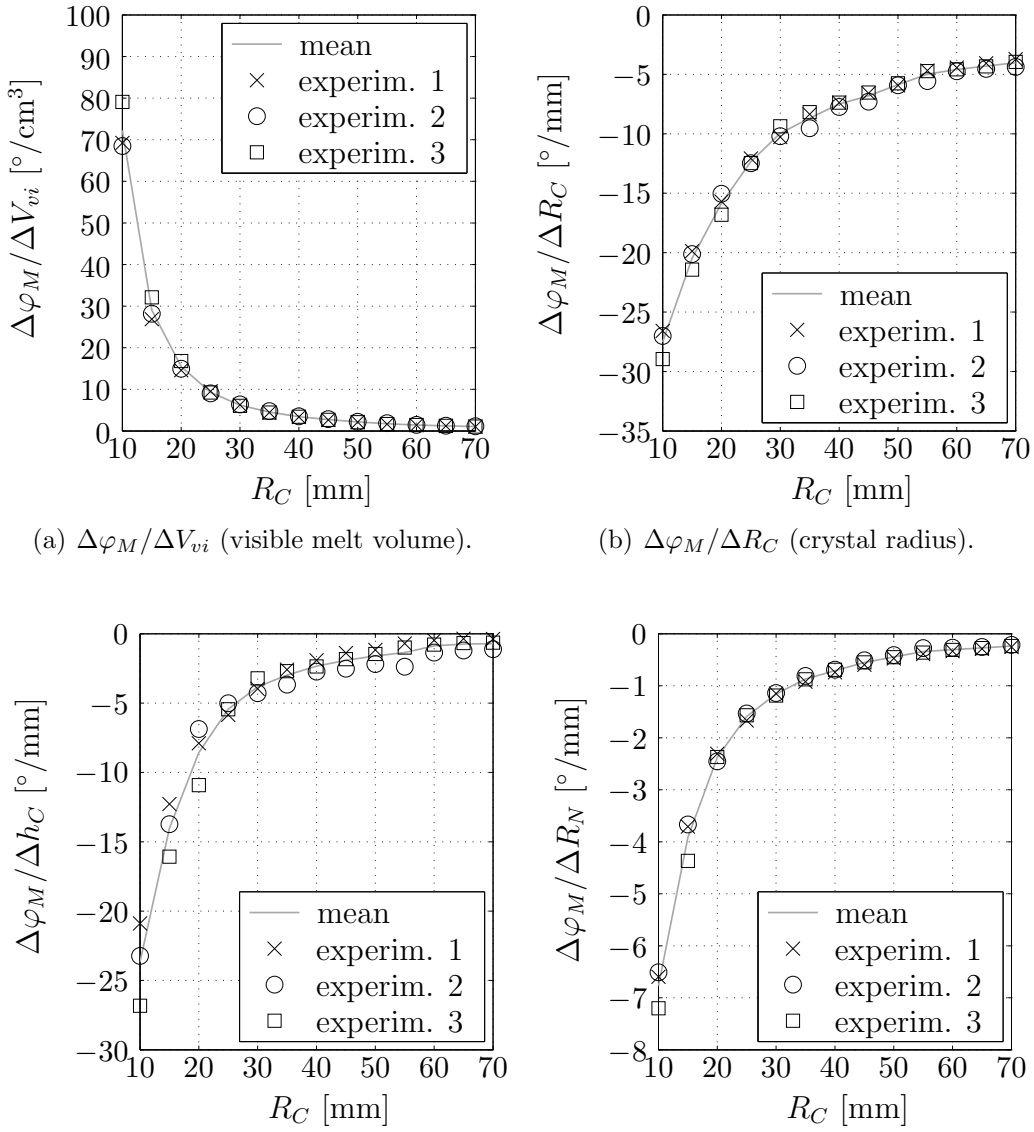

(a) $\Delta\varphi_M/\Delta V_{vi}$ (visible melt volume).

(b) $\Delta\varphi_M/\Delta R_C$ (crystal radius).

(c) $\Delta\varphi_M/\Delta h_C$ (lower zone height).

(d) $\Delta\varphi_M/\Delta R_N$ (melt neck).

Figure 4.13.: Difference quotients obtained from three experiments in the range of $10 \leq R_C \leq 70$, where φ_M is the melt angle, V_{vi} the visible melt volume, R_C the crystal radius, h_C the height of the lower zone, and R_N the radius of the melt neck. Mean average is drawn in gray and listed in table 4.1.

R_C [mm]	$\Delta\varphi_M/\Delta V_{vi}$ [°/cm^3]	$\Delta\varphi_M/\Delta R_C$ [°/mm]	$\Delta\varphi_M/\Delta h_C$ [°/mm]	$\Delta\varphi_M/\Delta R_N$ [°/mm]
10	72.27	-27.52	-23.65	-6.77
15	29.06	-20.47	-14.03	-3.91
20	15.45	-15.85	-8.56	-2.38
25	9.26	-12.34	-5.44	-1.59
30	6.22	-9.95	-3.83	-1.16
35	4.54	-8.69	-2.98	-0.87
40	3.43	-7.50	-2.33	-0.71
45	2.73	-6.81	-1.91	-0.55
50	2.15	-5.87	-1.60	-0.45
55	1.73	-4.99	-1.36	-0.34
60	1.43	-4.58	-0.87	-0.31
65	1.23	-4.31	-0.75	-0.27
70	1.06	-4.02	-0.71	-0.24

Table 4.1.: Calculated difference quotients by using the numerical solution of the Laplace-Young equation averaged over three experiments.

spect to ΔV_{vi}, ΔR_C, Δh_G, and ΔR_F. The quotients are not primarily coupled to the crystal radius R_C, instead, all variables (melt volume V_{vi}, full zone height h_G, crystal R_C and feed radius R_F) seem to be effecting the quotients. Hence, a kind of hypersurface would be needed for every partial derivative. Furthermore, an approximation function depending on the crystal radius R_C is unsuitable because the goal of the thin neck is to keep a constant crystal radius of 2-3 mm over the pull length of 30-50 mm. To keep the calculations simple, a mean average of the complete thin neck phase of several experiments is used to obtain values for the differential quotients. The estimated values are given in table 4.2.

R_C [mm]	$\Delta\varphi_M/\Delta V_{vi}$ [°/cm^3]	$\Delta\varphi_M/\Delta R_C$ [°/mm]	$\Delta\varphi_M/\Delta h_G$ [°/mm]	$\Delta\varphi_M/\Delta R_F$ [°/mm]
$\leq$5	443.87	-18.66	-8.27	-11.89

Table 4.2.: Difference quotients obtained for the thin neck phase.

Comparison to experimental data

Figure 4.14 (a) compares the prediction based on the model equation 4.47 (thick line), with experimental data (thin line) of the thin neck phase. The differential quotients from table 4.2 and numerical differentiations of $\dot{V}_{vi}$, $\dot{R}_C$, $\dot{h}_G$, and $\dot{R}_F$ are used. The correction factor of the melt neck a_N is set to zero

to avoid a negative effect in control and state estimation quality due to the measuring and modeling problems of the melt neck. In the cone phase, the value of a_h is set manually to 1.3 to fit the experimental data. Figure 4.14 (b) and (c) shows analog prediction for the cone phase and the comparison with two experiments. The plots in figure 4.14 show, that the model of the crystal angle φ_C reflects the dynamics of the experiments in the thin neck phase and in the cone phase.

4.1.7. Modeling the Rates of Melting and Crystallization

Finding a mathematical description for the melting rate v_{Me} and the crystallization rate v_{Cr} is more difficult due to the thermodynamical influence of the generator power P_{gen}. At first, a relation between the generator power P_{gen} and the power of the inductor P_{ind} is needed. The description of the electrotechnical behavior needs a detailed knowledge of a generator. A first order element

$$\frac{d}{dt}(P_{ind}) = \frac{1}{\tau_P}(K_P \cdot P_{gen} - P_{ind}) \tag{4.48}$$

is inserted to avoid time-consuming analysis of the electrotechnical components. The two model parameters in equation (4.48), time constant τ_P and gain factor K_P, characterize the relation between the generator power P_{gen} and the inductor power P_{ind}. The values of these parameters depend on the generator and its configuration. In this work, the power loss is neglected ($K_P = 1$).

The required heat Q to melt a mass m is calculated by the following equation

$$Q_{melting} = q_0 \cdot m \tag{4.49}$$

including the latent heat q_0. The latent heat q_0 is the specific heat to change a mass from a solid to a liquid state. It also describes the released heat if the state changes from melt to solid

$$Q_{crystallize} = q_0 \cdot m \quad . \tag{4.50}$$

The latent heat q_0 for silicon is 1803 $\frac{kJ}{kg}$. The relevant power to establish a mass flow for melting or crystallization is calculated by the following equations

$$\dot{m}_F = -\frac{P_{F,melting}}{q_0} \quad , \tag{4.51}$$

$$\dot{m}_C = \frac{P_{C,crystallize}}{q_0} \quad . \tag{4.52}$$

Here, $\dot{m}_F$ is the derivative of the feed mass, $\dot{m}_C$ the derivative of the crystal mass, $P_{F,melting}$ the power used for melting, $P_{C,crystallize}$ the released power due

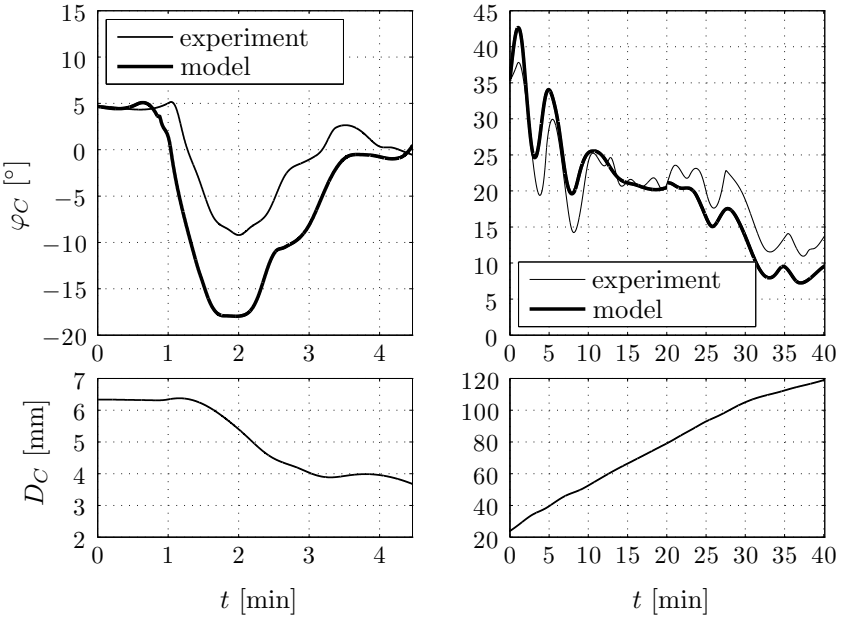

(a) Thin neck phase (experiment 1). The values $a_V = 1$, $a_R = 1$, $a_h = 1$, and $a_N = 0$ are used.

(b) Begin of cone phase (experiment 2): two predictions starting from $t = 0$ and $t = 20$ min. $a_V = a_R = 1$, $a_h = 1.3$, and $a_N = 0$.

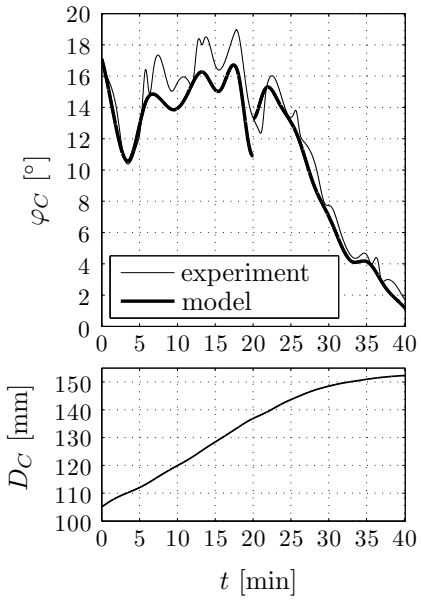

(c) End of the cone phase (experiment 3): two predictions (from $t = 0$, and $t = 20$ min). $a_V = a_R = 1$, $a_h = 1.3$, and $a_N = 0$.

Figure 4.14.: Comparison between the crystal angle φ_C from experiment (thin line) and the calculation based on the model equation (thick line).

to crystallization, and q_0 the latent heat. In section 4.1.5, the formulations for $\dot{m}_F$ and $\dot{m}_C$

$$\dot{m}_F = \rho_S(\dot{V}_{fr} - \pi R_F^2 v_{Me}) \quad , \tag{4.23}$$
$$\dot{m}_C = \rho_S(\pi R_C^2 v_{Cr} - \dot{V}_{bo}) \tag{4.25}$$

are deducted including the volume derivatives of feed residual $\dot{V}_{fr}$ and melt bowl $\dot{V}_{bo}$.

A quasi-steady balance equation for the power concerning the feed rod is:

$$0 = P_F - P_{F,loss} - P_{F,melting} \quad , \tag{4.53}$$

where P_F is the power introduced into the feed rod, $P_{F,loss}$ the power loss due to radiation, and $P_{F,melting}$ the power used for melting the feed material.

Based on Billig [Bil55], the power loss can be approximated as function of the radius R

$$P_{loss}(R) = \zeta_{lost} R^{\frac{3}{2}} \quad , \tag{4.54}$$

where ζ_{lost} is the power loss constant (for silicon $\zeta_{Si,lost} = 335.59\ \mathrm{kW} \cdot \mathrm{m}^{-\frac{3}{2}}$). A deduction of the equation is given in appendix A.1.

Analogously for the crystal, the quasi-steady balance equation for the power is

$$0 = P_C - P_{C,lost} + P_{C,crystallize} \quad , \tag{4.55}$$

where P_C is the power introduced into the crystal, $P_{C,loss}$ the power loss due to radiation, and $P_{C,crystallize}$ the power released due to crystallization.

Using equation 4.51, 4.23, and 4.53, the following equation for the melting rate v_{Me}

$$v_{Me} = \frac{P_F - P_{F,loss}}{q_0 \rho_S \pi R_F^2} + \frac{\dot{V}_{fr}}{\pi R_F^2} \tag{4.56}$$

is obtained. The derivative $\dot{v}_{Me}$ of the melting rate follows from

$$\begin{aligned} \dot{v}_{Me} = {} & \frac{1}{q_0 \rho_S \pi R_F^2} \cdot \left(\dot{P}_F - \dot{P}_{F,loss} - 2\frac{\dot{R}_F}{R_F}(P_F - P_{F,loss}) \right) \\ & + \frac{1}{\pi R_F^2} \cdot \left(\ddot{V}_{fr} - 2\frac{\dot{R}_F}{R_F}\dot{V}_{fr} \right) \quad . \end{aligned} \tag{4.57}$$

Analogously for the crystal, using equation 4.52, 4.25, and 4.55, the following

equation for the crystallization rate v_{Cr}

$$v_{Cr} = \frac{P_{C,loss} - P_C}{q_0 \rho_S \pi R_C^2} + \frac{\dot{V}_{bo}}{\pi R_C^2} \tag{4.58}$$

is obtained. The derivative $\dot{v}_{Cr}$ of the crystallization rate follows from

$$\begin{aligned} \dot{v}_{Cr} = & \frac{1}{q_0 \rho_S \pi R_C^2} \cdot \left(\dot{P}_{C,loss} - \dot{P}_C - 2\frac{\dot{R}_C}{R_C}(P_{C,loss} - P_C) \right) \\ & + \frac{1}{\pi R_C^2} \cdot \left(\ddot{V}_{bo} - 2\frac{\dot{R}_C}{R_C}\dot{V}_{bo} \right) \quad . \end{aligned} \tag{4.59}$$

Modeling the variables P_F (power introduced into the feed rod) and P_C (power introduced into the crystal) is a complex task. Building a physical model is very time-consuming and leads to complex equations. To keep the equation simple, a heuristic approach is applied. The introduced power depends primarily on the inductor power, the radius of feed/crystal, and the corresponding zone height. The model equations have to reflect the following effects:

- the introduced power is gained if the inductor power increases due to the higher heater power
- the introduced power is gained if the radius of the corresponding rod (feed or crystal) increases due to the higher cross section
- the introduced power decreases if the corresponding zone height (lower or upper) increases due to the higher distance between heater source and corresponding rod (feed or crystal)

The following approach is used to fulfill these requirements:

$$P_F = P_{ind,F} \cdot (R_F)^{r_F} \cdot (1 - f_0 h_F)^{f_1} \quad , \tag{4.60}$$

$$P_C = P_{ind,C} \cdot (R_C)^{r_C} \cdot (1 - c_0 h_C)^{c_1} \quad , \tag{4.61}$$

where $P_{ind,F}$ is the part of the inductor power acting on the feed rod and $P_{ind,C}$ that for the crystal. The variables r_F, f_0, f_1, r_C, c_0, and c_1 are model parameters to fit experimental data. The equations include the heater power, the influence of the radii of feed $(R_F)^{r_F}$ and crystal $(R_C)^{r_C}$, and the upper h_F and lower h_C zone height. Effects of hole and slits of the inductor are neglected in this approach. The equations 4.60 and 4.61 are used in a suitable range of radii and zone heights. The parameters f_0 and c_0 have to be set that the terms $(1 - f_0 h_F)$ and $(1 - c_0 h_C)$ are positive for the appearing zone heights. The used parameters are listed in table 4.3.

The generator power P_{gen} could not directly be adjusted on the used FZ machines. Instead, the value of the DC voltage U_{gen} of the generator can be

adjusted to manipulate the heater power. The following relations are used

$$\frac{d}{dt}(U_{ind}) = \frac{1}{\tau_P}(K_P \cdot U_{gen} - U_{ind}) \tag{4.62}$$

and

$$P_{ind,F} = p_F\Big(U_{ind}\Big)^{e_F} \quad , \tag{4.63}$$

$$P_{ind,C} = p_C\Big(U_{ind}\Big)^{e_C} \quad . \tag{4.64}$$

to describe the power values $P_{ind,F}$ and $P_{ind,C}$ involving the model parameters p_F, p_C, e_F, and e_C. Table 4.3 gives the values of the used parameters of the thermodynamical model for the thin neck and the cone phase. The parameters are specified concerning a generator voltage in the unit kV and zone heights and radii in mm. The listed parameters are manually adjusted. The identification of p_F and p_C using numerical optimization is part of the section 4.4.

Parameter	thin neck	cone
K_P	1	1
τ_P	2 s	20 s
e_F	2	2
r_F	2	1
f_0	0.1	0.05
f_1	1	1
e_C	2	2
r_C	2	1.5
c_0	0.1	0.05
c_1	2	2

Table 4.3.: Parameters of the thermodynamical model. The parameters are specified concerning a generator voltage in the unit kV and zone heights and radii in mm.

4.2. Overview of the Low-Order Model

Table 4.4 gives an overview of the low-order model of the FZ process. The states of the model are listed with the corresponding number of the differential equation. Additionally, the states and the input variables involved in the differential equations are given.

state	equat.	involving states	involving inputs
radius R_F of the feed	4.9	melting rate v_{Me} feed angle α_F	
radius R_C of the crystal	4.10	crystalliz. rate v_{Cr} crystal angle φ_C	
upper zone height h_F	4.7	melting rate v_{Me}	pull rate v_F
lower zone height h_C	4.8	crystalliz. rate v_{Cr}	pull rate v_C
visible melt volume V_{vi}	4.27	feed radius R_F crystal radius R_C melting rate v_{Me} crystalliz. rate v_{Cr}	
melting rate v_{Me}	4.57	inductor power P_{ind} feed radius R_F upper zone height h_F	
crystalliz. rate v_{Cr}	4.59	inductor power P_{ind} crystal radius R_C lower zone height h_C	
crystal angle φ_C	4.41	vis. melt volume V_{vi} crystal radius R_C lower zone height h_C radius melt neck R_N	
radius melt neck R_N	4.14	upper zone height h_F lower zone height h_C	
inductor power P_{ind}	4.48	inductor power P_{ind}	gen. power P_{gen}
feed angle α_F	4.13		

Table 4.4.: Overview of the model equations.

4.3. Simulation Studies of the Low-Order Model

Figure 4.15 (a) shows the step response of the system according to a step of the heater power (in this case the generator voltage U_{gen}). The increment of the penetrated heater power produces a temporary melt overhang resulting in an increasing angle and diameter. Both, crystal angle and diameter, return to

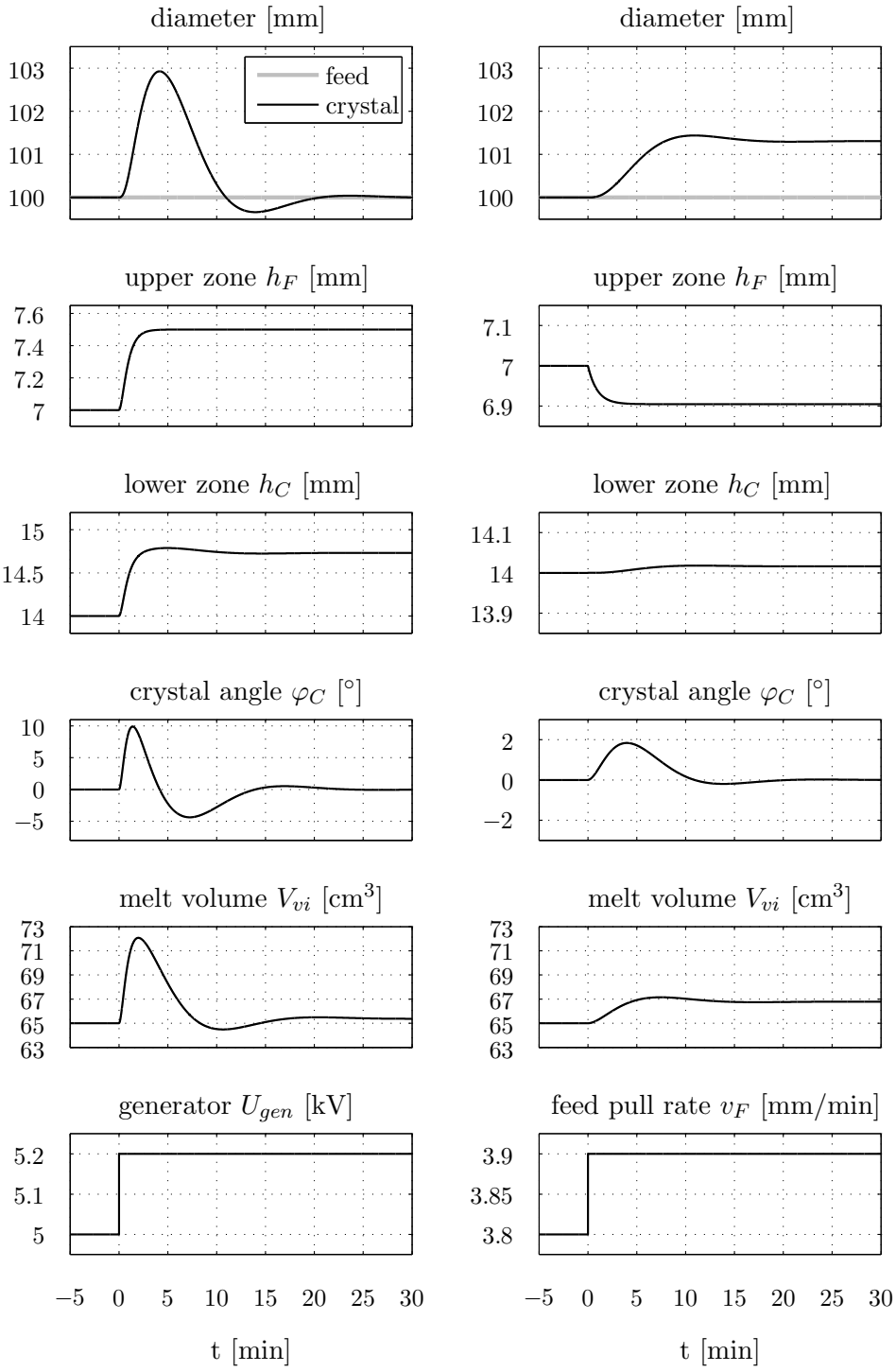

(a) Step response of the generator voltage U_{gen}.

(b) Step response of the feed pull rate v_F.

Figure 4.15.: Two simulation studies of the low-order model. For $t \leq 0$ the system is stationary. Feed and crystal start with a diameter of 100 mm. The step responses of the heater power (a) and the pull rate of the feed (b) are shown.

its initial values after approximately 20 minutes. This is due to the stationary mass balance given in equation 4.28. The step of the heater power has a stationary effect on the zone heights, but not on the crystal diameter. An undershooting of the diameter during the settling response is observable. Figure 4.15 (b) shows the step response of the feed pull rate v_F. Stationary effects are observable in the values of zone heights and crystal diameters. The crystal diameter shows a slight overshooting during the settling response. This is observable in the experimental data of the *landing phase* also, where the crystal cone is swinging into the cylindrical part. The transient response of the quantities can be fitted to experimental data by adjusting the model parameters. This procedure is denoted as *parameter identification*.

4.4. Comparison with Experimental Data

This section presents the result of the parameter identification of the model and Kalman filter. Most of the model parameters, except for p_F and p_C, are obtained in separate identifications. Only the two parameters p_F and p_C are used to fit experimental data. This is done separately for the thin neck phase and the cone phase using numerical optimization (see sections 2.4.3). The used weight matrix $\boldsymbol{W}_\Theta$ is given in the section A.4.2 in the appendix. A list of all model parameters is given in sections A.6.1 and A.6.2.

For the cone phase, two growth experiments of crystals with 100 mm in diameter on FZ machine 1 using an inductor (applicable for 100 mm crystals) are used to identify the parameters p_F and p_C. Figure 4.16 shows the comparison between model prediction and experimental data which are involved in the identification. As expected, a high prediction quality is achieved. Two examples of a conformity validation are shown in figure 4.17 and 4.18 using experiments which are not involved in the identification process. The growth experiment, shown in figure 4.17, was made on FZ machine 1 using an inductor applicable for 150 mm crystals. The experiment, shown in figure 4.18, was made on FZ machine 2 using an inductor applicable for 100 mm crystals. The model predictions reproduce the dynamics of the process. The application of the model at different machines and for different crystal diameters can be expected valid without a renewed parameter identification.

Figure 4.19 shows the result of the state estimation using Kalman filter. The Kalman filter uses the full model and estimates the process states such as melting v_{Me} and crystallization rate v_{Cr}. These both quantities are not directly measurable, but needed during the model-based automation. In addition, the Kalman filter reduces the measurement noise of all quantities. As mentioned in section 2.5.2, the parameters $\boldsymbol{Q}$ and $\boldsymbol{R}$ of the Kalman filter are obtained using numerical optimization. The used weight matrix $\boldsymbol{W}_{QR}$ is given in the section A.4.1. Lists of the identified parameters are given in sections A.5.1 and A.5.2.

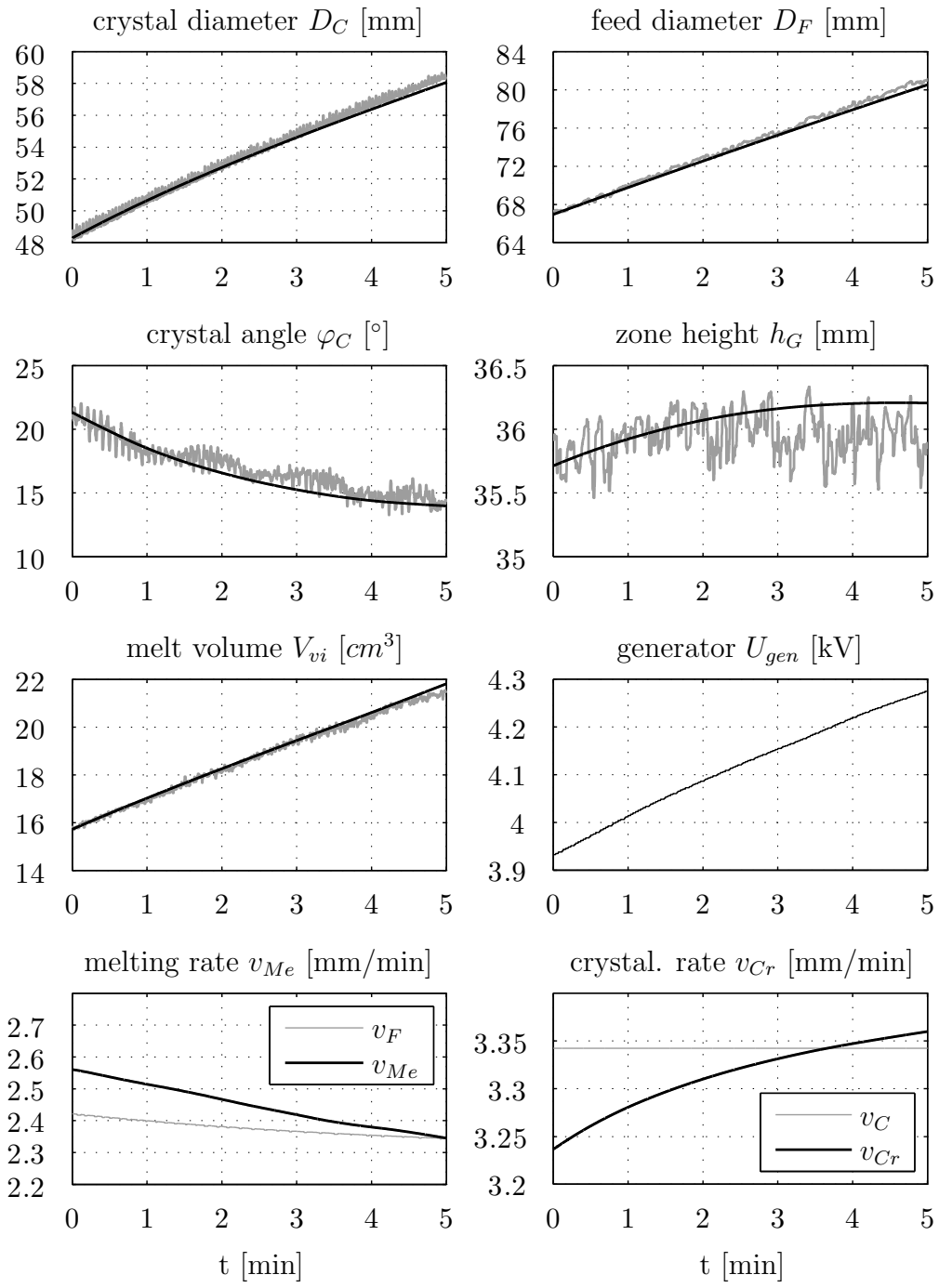

Figure 4.16.: Comparison between model prediction (black) and experimental data (gray) which are involved in the parameter identification. The growth experiment was made on FZ machine 1 using an inductor applicable for 100 mm crystals. v_F is the pull rate of the feed rod and v_C the pull rate of the crystal.

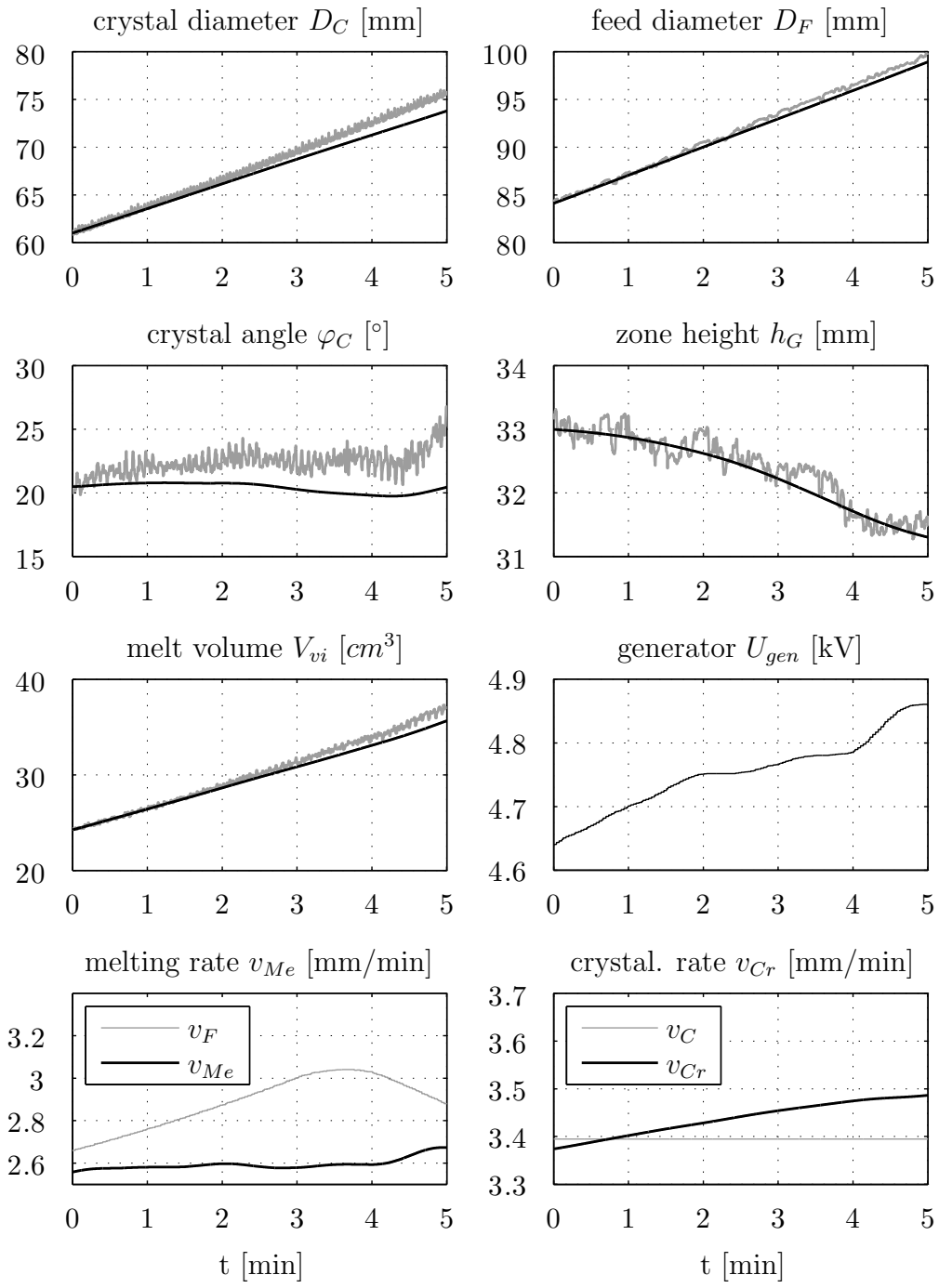

Figure 4.17.: Cross-validation: Comparison between model prediction (black) and experimental data (gray) which are not involved in the parameter identification. The growth experiment was made on FZ machine 1 using an inductor applicable for 150 mm crystals. v_F is the pull rate of the feed rod and v_C the pull rate of the crystal.

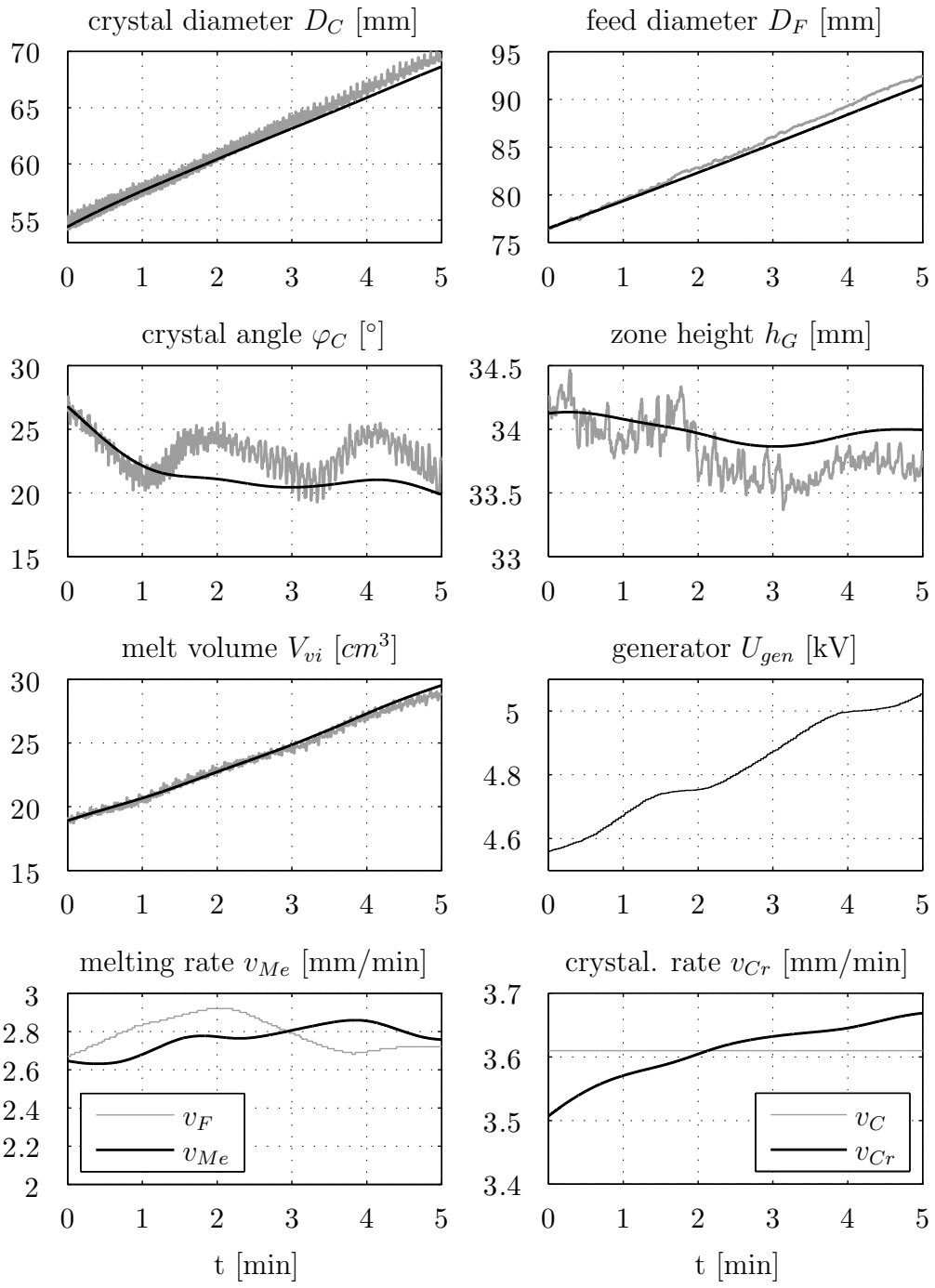

Figure 4.18.: Cross-validation: Comparison between model prediction (black) and experimental data (gray) which are not involved in the parameter identification. The growth experiment was made on FZ machine 2 using an inductor applicable for 100 mm crystals. v_F is the pull rate of the feed rod and v_C the pull rate of the crystal.

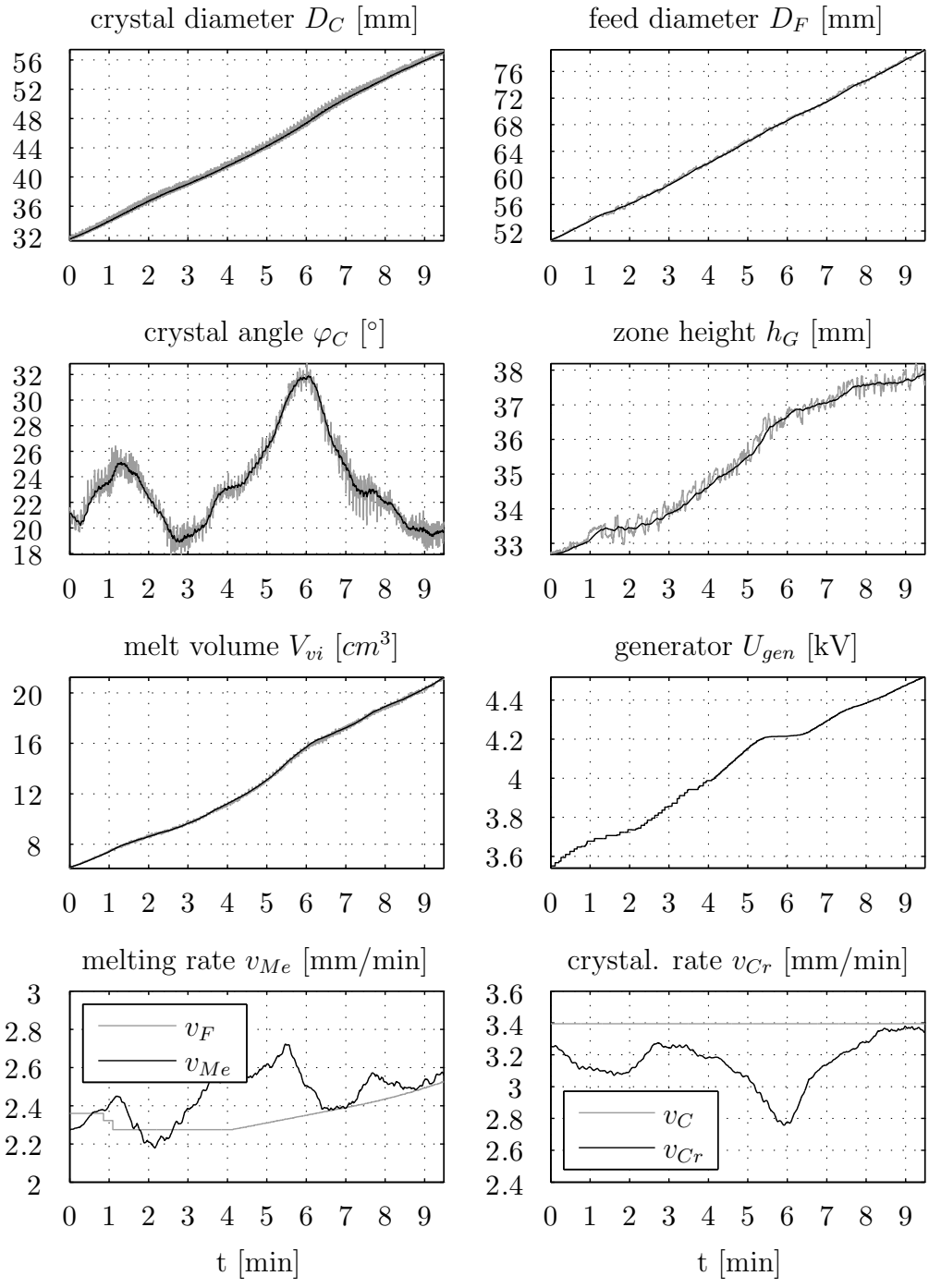

Figure 4.19.: Result of state estimation using Kalman filter. The Kalman filter is applied to estimate melting v_{Me} and crystallization rate v_{Cr} and to reduce measurement noise. v_{Me} and v_{Cr} are not directly measurable, but needed during the model-based automation. v_F is the pull rate of the feed rod and v_C the pull rate of the crystal. Estimated states are shown in black and measurements in gray.

5. Automation

This section presents the automation concept of the FZ process developed in this thesis. The different phases of the process are analyzed with respect to the tasks of control engineering. The applicability of the low-order model is investigated using a predictive controller. Functional details of the controller are given in section 2.4.4.

5.1. FZ Control Approaches

5.1.1. Control Phases

With respect to control engineering, the FZ process can be divided into the following phases:

- Forming the *feed tip*:

  This is the preparation step to produce suitable conditions for creating the thin neck. Feed and seed crystal are moved upwards to form the feed tip. This is regulated by a PI-controller due to the low dynamics and the approximately constant working point. In the following phases, the model predictive controller is used to regulate the process.

- Creating the *thin neck*:

  This is the begin of growing the crystal. Feed and crystal are moved downwards to create the thin neck. The crystal diameter of 5-6 mm, resulting from the diameter of the seed, has to be reduced down to 2-3 mm and kept constant until the end of that phase.

- Establishing the *molten zone*:

  Here, the molten zone is filled with melt to produce a melt overhang needed to increase the crystal diameter. The pull rates of the feed and the crystal are set to approximately constant values and the heater power is adjusted to stabilize the melt overhang.

- Growing the *crystal cone*:

  The crystal diameter has to be increased by keeping the melt overhang. This is done by adjusting heater power and pull rate of the feed. Then, the melt overhang is slowly decreased to avoid a leakage of the melt. In addition, the melt neck has to be kept in its constraints due to the inductor hole. This phase can be divided into two parts: the first part, where the diameter of the feed is changing due to its tapered shape and the second phase, where the tapered feed rod is melted off and the feed retains a constant diameter. In the first part, the dynamics are more complex as in the second one because of the changing size. In this and the next phases, it is common to use a constant or very slow changing pull rate of the crystal to ensure a dislocation-free crystal growth (see

section 3.5). A slowly decreasing pull rate of the crystal pull rate is used for crystals with diameters of more the 125 mm.

- Swinging into the cylindrical part (*landing*):

  The melt overhang is decreased to zero, so that the crystal diameter hits the desired value. The corresponding pull rate of the feed can be calculated based on the stationary mass balance (see section 4.1.5)

  $$D_F^2 v_F = D_C^2 v_C \quad , \tag{5.1}$$

  where D_F is the diameter of the feed, D_C the desired diameter of the crystal, v_F the pull rate of the feed, and v_C that of the crystal.

- Growing the *cylinder*:

  Here, the crystal diameter is held constant. This is managed by constant heater power and constant pull rates of feed and crystal. The process is self-regulating and in a stable state during this phase. At the end of the process, the heater power has to be adjusted slightly to keep the height of the molten zone. Here, the heat transport of the feed rod is effected due to length reduction.

5.1.2. Choice of Reference and Manipulated Variables

It is essential to set up suitable reference and control variables to fulfill the requirements of the respective phases. The control variables of the FZ process are the heater power of the inductor and the pull rates of feed and crystal. The reference values can be defined as functions of time, crystal diameter or crystal length.

The automation of the feed tip has to ensure suitable start conditions for the thin neck phase. These conditions are defined as shape of the feed tip (diameter D_F across the length), zone height h_G, and the melt volume V_{vi}. For creating the thin neck, the references are the zone height and the crystal diameter as functions of time. Two strategies are investigated: the first one uses heater power and pull rate of the crystal for satisfying the references, the second one uses heater power and feed pull rate (see table 5.1).

To establish the molten zone, the heater power is adjusted to satisfy the desired zone height, which is defined as a function of the crystal diameter. Here, the pull rates are set to constant values. The automation of this phase is not included in the thesis and could be a task of future works. However, pretrial experiments have shown that this could produce sufficient results. If a given crystal diameter is reached (approximately 15-20 mm), then the cone phase starts.

Two approaches are investigated to automate the crystal growth of the cone into the cylindrical part.

Phase	Reference Variables	Control Variables
feed tip	zone height, feed diameter, melt volume	heater power, pull rate of feed or crystal
thin neck	zone height, crystal diameter, melt volume	heater power, pull rate of feed or crystal

Table 5.1.: Reference and control variables for regulating feed tip and thin neck

Cone Regulation (Approach 1):

In the first approach, the process is stabilized by controlling crystal angle φ_C and full zone height h_G as function of crystal diameter. This is done by adjusting the control variables heater power and feed pull rate. The observation of the melt neck is important to satisfy the limits due to the inductor hole (see section 3.5). To overcome measuring problems of the melt neck, the zone height h_G is applied as an auxiliary quantity within the automation. The reference of the zone height can be designed so that a suitable melt neck appears. To ensure this, a constraint for the melt neck can be set. The reference values are defined as functions of the crystal diameter. This results in a kind of smooth regulation of the cone.

In the landing phase, references for the zone height h_G and crystal diameter D_C are used. Equation 5.1 determines the needed pull rate of the feed to satisfy the desired diameter of the crystal. The current pull rate is increased slowly up to the needed pull rate and the heater power is used to keep the zone height. When the cylinder is grown, constant references are used of zone height and crystal diameter. Here, only small changes of heater power and feed pull rate are necessary to satisfy the reference values. An overview of the variables used in this approach is shown in figure 5.1 and listed in table 5.2.

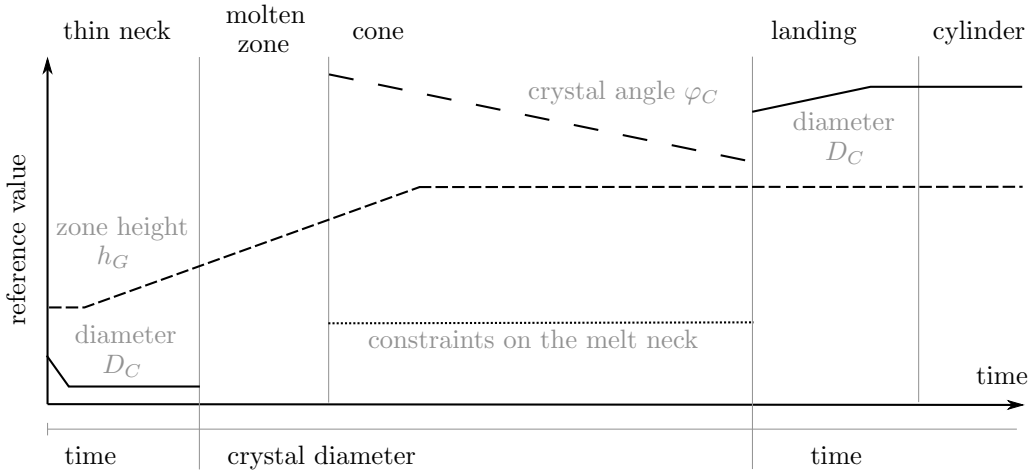

Figure 5.1.: Sketch of the reference variables applied to automate the FZ process (Approach 1)

Phase	Reference Variables	Control Variables
cone	crystal angle and zone height	heater power and pull rate of the feed
landing	crystal diameter and zone height	heater power and pull rate of the feed
cylinder	crystal diameter and zone height	heater power and pull rate of the feed

Table 5.2.: Reference and control variables for the regulation of the FZ process (Approach 1)

Cone Regulation (Approach 2):

This approach achieves a reproducible shape of the crystal by using the crystal diameter (instead of the crystal angle) as reference. The complete crystal, starting from the cone, is defined as function of the crystal length L_C. Here, the separation of the phases concerning different reference values is omitted. Different cone shapes for such as crystals with 100 mm, 125 mm, 150 mm in diameter can be defined and adjusted easily. A sketch of the references used in this approach is shown in figure 5.2. It must be noted that the definition of the cone contour has to be done carefully based on experimental experiences. Forcing unfavorable quantities could create negative growth condition. This can lead to creation of bulge formation at the crystal (as shown in figure 3.18 in section 3.5), creation of dislocations, or leakage of melt.

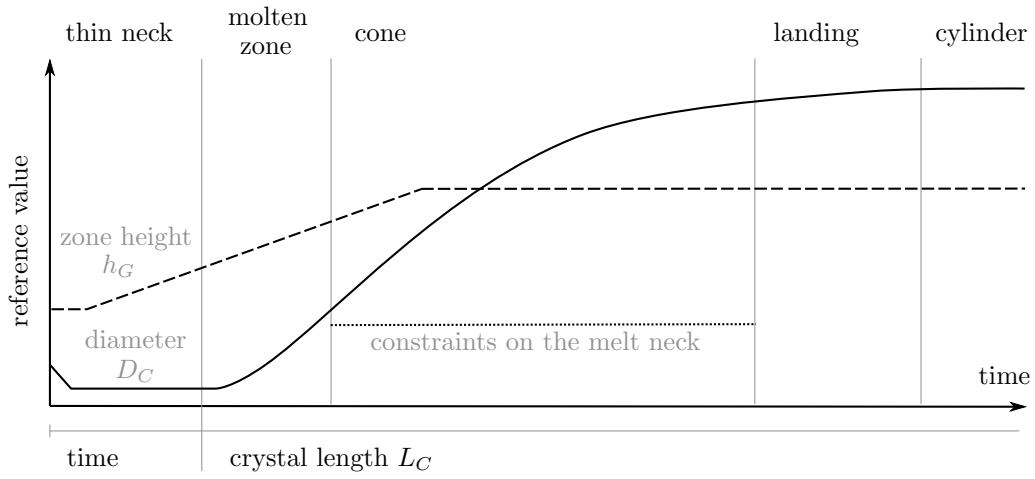

Figure 5.2.: Sketch of the references applied to automate the FZ process (Approach 2)

5.2. Automatic Forming of the Feed Tip

This section presents an approach for the regulated forming of the feed tip to produce specified start conditions for the growth of the thin neck. The principle quantities which define the start conditions are the shape of the feed tip, the zone height, and the melt volume. The shape of the feed tip is determined by the diameter across the length. Before the regulation starts, the seed crystal was manually dipped into the melt drop. After melting together, the feed rod and the seed starts to move upwards to build the solid feed tip. The automatic forming of the feed tip consists of two sequential steps: the first forms the diameter of the feed tip and second generates the desired volume and height of the molten zone. The regulation is sufficiently achieved by standard PI controller due to the low dynamics and a nearly fixed working point. In the figures of the experiments, negative pull rates mean an upward movement of feed or crystal.

5.2.1. Regulation of the Feed Tip Diameter

The goal of the regulation is reducing the feed diameter D_F to its final target (approximately 6-8 mm). To stabilize the process, the full zone height h_G has to be controlled as well. The final target of h_G is the desired value for the start of thin neck phase. The generator voltage U_{gen} is adjusted by a PI controller (see equation 2.1) to control the zone height h_G. The parameter K_p and K_i are obtained using the root locus method. The conditions of a maximum overshoot of 1 % and a settling time of 60 seconds are considered in the control design. The parameter are given in the section A.7.1.

The pull rate v_F of the feed is calculated by the equation

$$v_F = v_C \left(\frac{D_C}{D_F} \right)^2 \quad , \tag{5.2}$$

where D_C is the measured diameter of the crystal, D_F the desired diameter of the feed, and v_C is the pull rate of the crystal. Experiments showed that at the beginning of the regulation, where the feed has a diameter D_F of 12-14 mm, the molten zone was moved upwards due to a too high pull rate v_C. The zone was covered by the inductor and could not be captured by the measuring system. Figure 5.3 (a) shows the applied reference trajectory of the pull rate v_C. The rate is determined as function of the feed diameter D_F. The pull rate v_C has to be lower at the beginning of the regulation compared to the end. This ensure the visibility of the molten zone for the measurement system. In the control loop, v_C is set automatically depending on the measured feed diameter D_F. As shown in figure 5.3 (b), the reference of the zone height h_G is determined as function of D_F as well. This is done to avoid an aggressive acting of the controller and to reduce the risk of undershooting of the zone height.

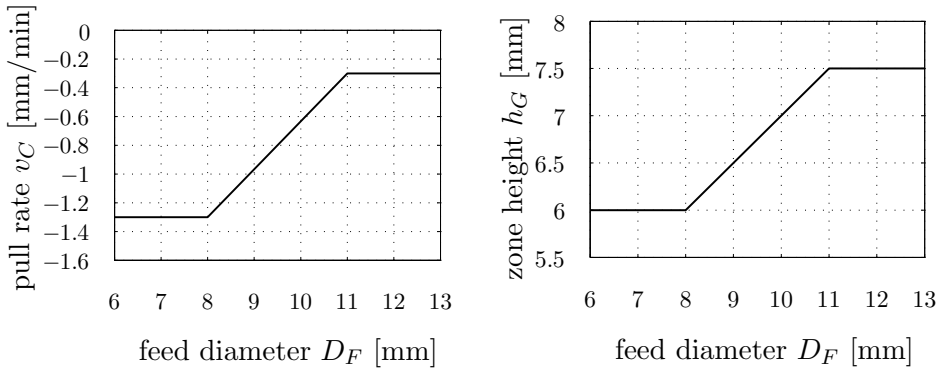

(a) Reference of the crystal pull rate v_C (b) Reference of the zone height h_G

Figure 5.3.: Reference trajectories of crystal pull rate v_C and zone height h_G

Figure 5.4 shows a regulation experiment. The feed tip is formed by automatic control using the targets of feed diameter D_F = 7.5 mm and zone height h_G = 6 mm. The reference trajectories, given in figure 5.3, are used within the regulation. The regulation of the feed diameter finishes at t = 12 minutes, where the desired length of the feed tip is reached. The oscillating pull rate v_F is due to the rotation of the crystal and resulting oscillations of the measurement. In the next step, the desired melt volume and zone height have to be generated.

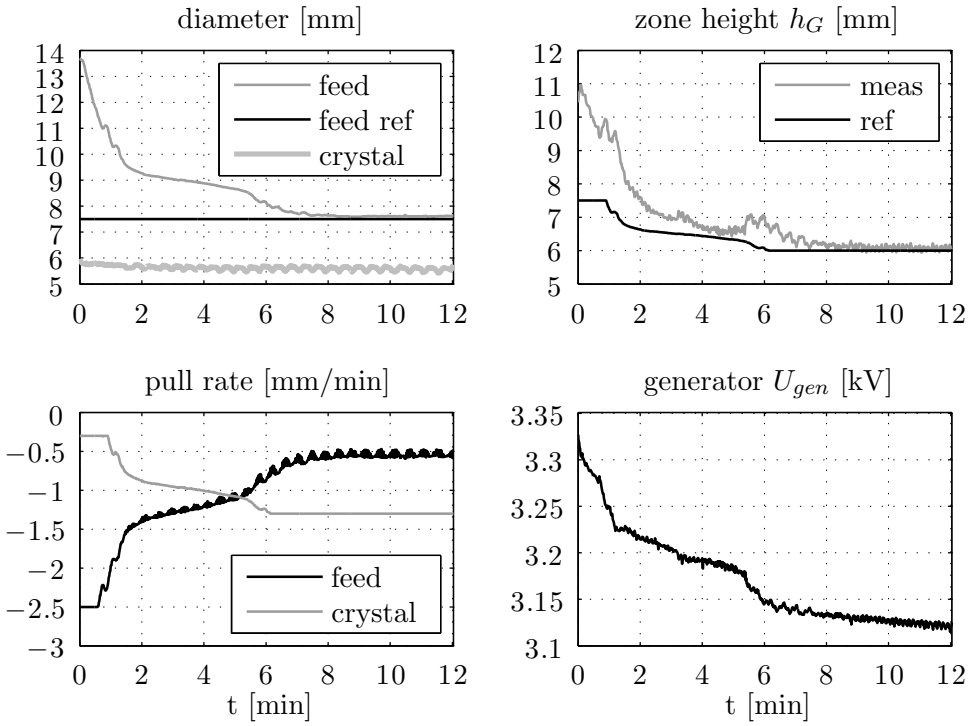

Figure 5.4.: Time plot of an automatic forming of the feed tip with final targets of 7.5 mm in diameter and a zone height h_G of 6 mm.

5.2.2. Regulation of Volume and Height of the Molten Zone

Figure 5.5 shows the regulation technique for reducing the volume of the molten zone. The feed is moved upwards and the crystal downwards by constantly keeping the height of the molten zone. The pull rates of crystal v_C and feed v_F are adjusted by a P controller using the equation

$$v_F = -K_p \cdot (V_{vi,meas} - V_{vi,ref}) \quad , \tag{5.3}$$

$$v_C = K_p \cdot (V_{vi,meas} - V_{vi,ref}) \quad , \tag{5.4}$$

where K_p is the proportional factor of the P controller, $V_{vi,meas}$ the measured volume, and $V_{vi,ref}$ the desired volume. K_p is given in the section A.7.1. Limitations of the pull rates of ± 0.3 mm/min are applied to avoid an aggressive control response. The generator voltage U_{gen} is adjusted by a PI controller to control the zone height h_G.

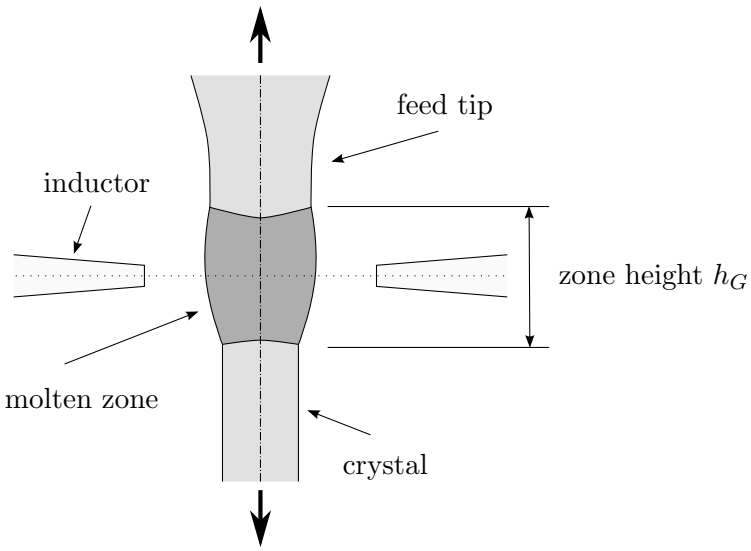

Figure 5.5.: Sketch of the regulation technique for reducing the volume of the molten zone. The feed is moved upwards and the crystal downwards by constantly keeping the height of the molten zone.

Figure 5.6 shows a regulation experiment. The volume of the molten zone is reduced from 280 mm^3 down to 180 mm^3 and the zone height h_G is kept at 6 mm. The regulation takes 8 minutes to satisfy the reference of the volume.

The regulation of the feed tip including diameter and volume, takes twice as much time compared to the manual growth. There are two reasons. On the one hand, the regulation is limited due to the visibility of the measurement system. On the other hand, the operator forms simultaneously the feed tip and the melt volume. Nevertheless, the higher regulation time is negligible with respect to the growth time of several hours and the generation of reproducible start conditions for the thin neck phase.

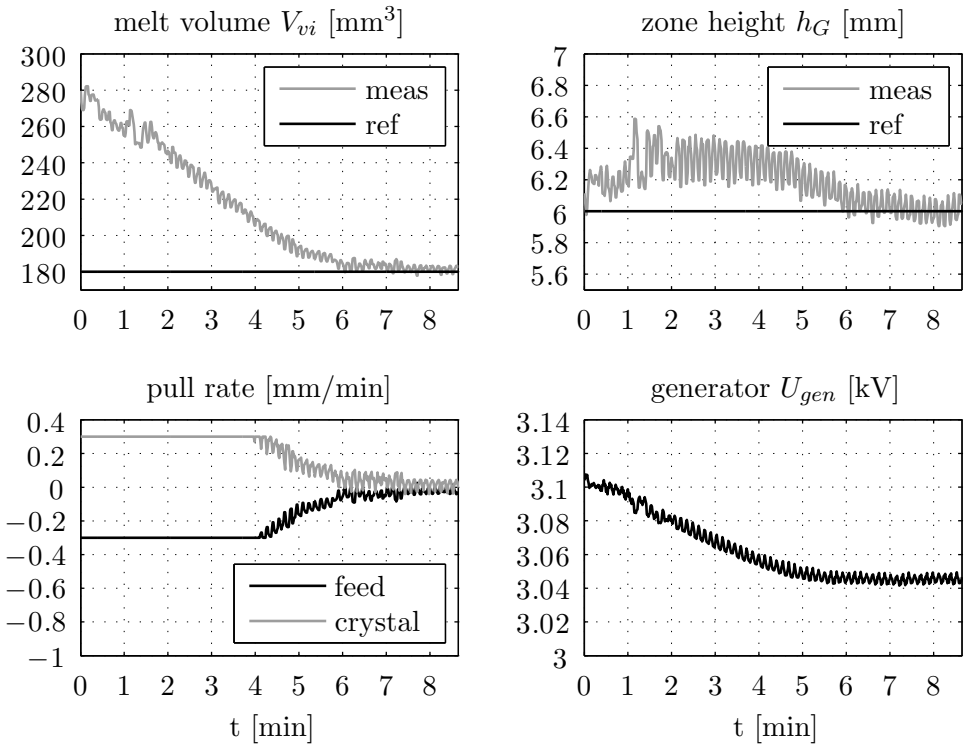

Figure 5.6.: Regulated reducing of the volume V_{vi} of the molten zone from 280 mm^3 down to 180 mm^3 by moving the pull rates in the opposite direction and constantly keeping the zone height h_G at 6 mm. Limitation of the maximum pull rates of ± 0.3 mm/min are applied.

5.3. Regulated Growth of the Thin Neck

In this section, two strategies are presented to stabilize the thin neck phase referencing of crystal diameter D_C and zone height h_G. The first strategy uses the heater power and the pull rate of the crystal to satisfy the references, the second one heater power and feed pull rate.

Before growing the thin neck, the feed tip is formed and the pull rates are switched off (v_F=v_C=0). To achieve a fast reduction of the crystal diameter after activating the pull rates, it is recommended to keep a small zone height h_G first. Afterward, the zone height has to be increased by using steps or ramps. As shown in figure 5.7 (a), the height h_G of the molten zone has to be kept in a suitable range, otherwise, the crystal and the feed could freeze together (b) or the feed could be divided from the molten zone (c). Additionally, it is useful to start with a smaller diameter reference as the final target of 2-3 mm to achieve a fast diameter reduction.

It can be observed that the molten zone moves slowly upwards during the growth of the thin neck. That results in measuring problems of the lower

zone height on the one hand and in a disturbed molten zone on the other hand. Here, disturbed means that the heater power can not penetrate into the crystal. In that case the regulation failed. To avoid a moving zone, a lower limitation of the lower zone height h_C of 1-3 mm is implemented within the controller.

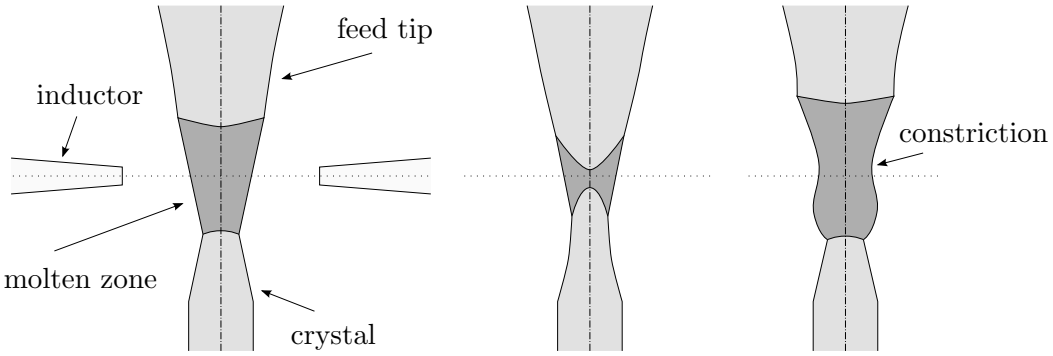

(a) Stable molten zone (b) Small zone (c) Large zone

Figure 5.7.: Sketch of the molten zone during the thin neck phase. Stable molten zone with the shape of a trapeze (a). Small zone with a high risk of freezing (b). Large zone with a constriction and a high risk of separation of the feed from the molten zone (c).

5.3.1. Using Heater Power and Crystal Pull Rate (Approach 1)

The generator voltage U_{gen} is adjusted by the model predictive controller to satisfy the reference for the zone height h_G and to fulfill the lower limitation of the lower zone height h_C. The pull rate v_F of the feed is constant and that of the crystal v_C

$$v_C = v_F \left(\frac{D_F}{D_C} \right)^2 \quad , \tag{5.5}$$

is calculated based on the stationary mass balance (see equation 5.1), where D_F is the measured diameter of the feed tip and D_C the desired diameter of the thin neck.

Figure 5.8 shows the result of a control experiment. The parameters of the model predictive controller are given in section A.7.2. The target diameter of the thin neck is 2.5 mm. The regulation starts at t=0 by activating the pull rates with initial values of v_C=15 mm/min and v_F=2.3 mm/min. First, the controller reduces the heater power to retain the increasing zone height h_G. At t=45 seconds, the reference of h_G is set from 8 mm up to 10 mm to stabilize the strongly reducing zone. Additionally, the lower limitation of the lower zone height $h_C \geq 2.5$ mm supports the stabilization. After 2 minutes, the desired crystal diameter of 2.5 mm is reached and kept.

5.3.2. Using Heater Power and Feed Pull Rate (Approach 2)

Another strategy growing the thin neck is the usage of the feed pull rate v_F and the heater power as control variables. Here, the pull rate v_C of the crystal is constant. At first, the calculation of $v_F = v_C \cdot (D_C/D_F)^2$ based on equation 5.1 can be tried. It is obvious that the pull rate of the feed decreases $v_F\downarrow$ during the thin neck phase due to the increasing diameter $D_F\uparrow$ of the feed tip. In experiments, it could be observed that this leads to an unstable molten zone. The molten zone suddenly shrinks and the heater power strongly increases to stabilize the zone. Therefore, the desired diameter of the thin neck of 2-3 mm could not be reached.

An advanced approach is the consideration of the stability of the molten zone. The shape of a stable zone could by approximated as the shape of a trapeze or a frustum. The sketch of the circular cone frustum is given in appendix A.3. For a stable zone, the reference of the melt volume V_{vi}

$$V_{vi} = \frac{\pi}{12} \cdot h_G \cdot (D_C^2 + D_C D_F + D_F^2) \tag{5.6}$$

can be formulated based on the frustum volume, where D_C is the desired diameter of the thin neck, D_F the measured diameter of the feed tip, and h_G the reference of the full zone height.

Figure 5.9 shows the result of a control experiment with a target diameter of 3 mm. The predictive controller adjusts the generator voltage U_{gen} and the pull rate v_F of the feed to satisfy the references of the zone height h_G and the melt volume V_{vi}. The volume reference is calculated by equation 5.6. The predictive controller uses a piecewise linear development of the generator voltage U_{gen} and a piecewise constant development of the pull rate v_F to permit a fast reaction of the control error with respect to the limitations $0.8 \leq v_F \leq 3.5$ mm/min. The crystal pull rate v_C is constant at 8 mm/min. The parameters of the model predictive controller are given in section A.7.3. After 2 minutes, the desired crystal diameter of 3 mm is reached. The reference of the zone height h_G is implemented as positive ramp starting from 60 seconds. The risk of an up-moving molten zone is low, the boundary of the lower zone height $h_C \geq 1.5$ is fulfilled at any point during the experiment. The regulation shows an oscillating evolution in the generator voltage U_{gen}. This could be improved by adjusting the controller parameter.

However, both control strategies (figure 5.8 and 5.9) are usable for the regulated growth of a thin neck. A behavior comparable to the manual growth can be achieved.

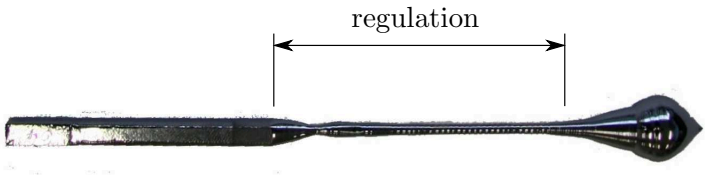

(a) Image

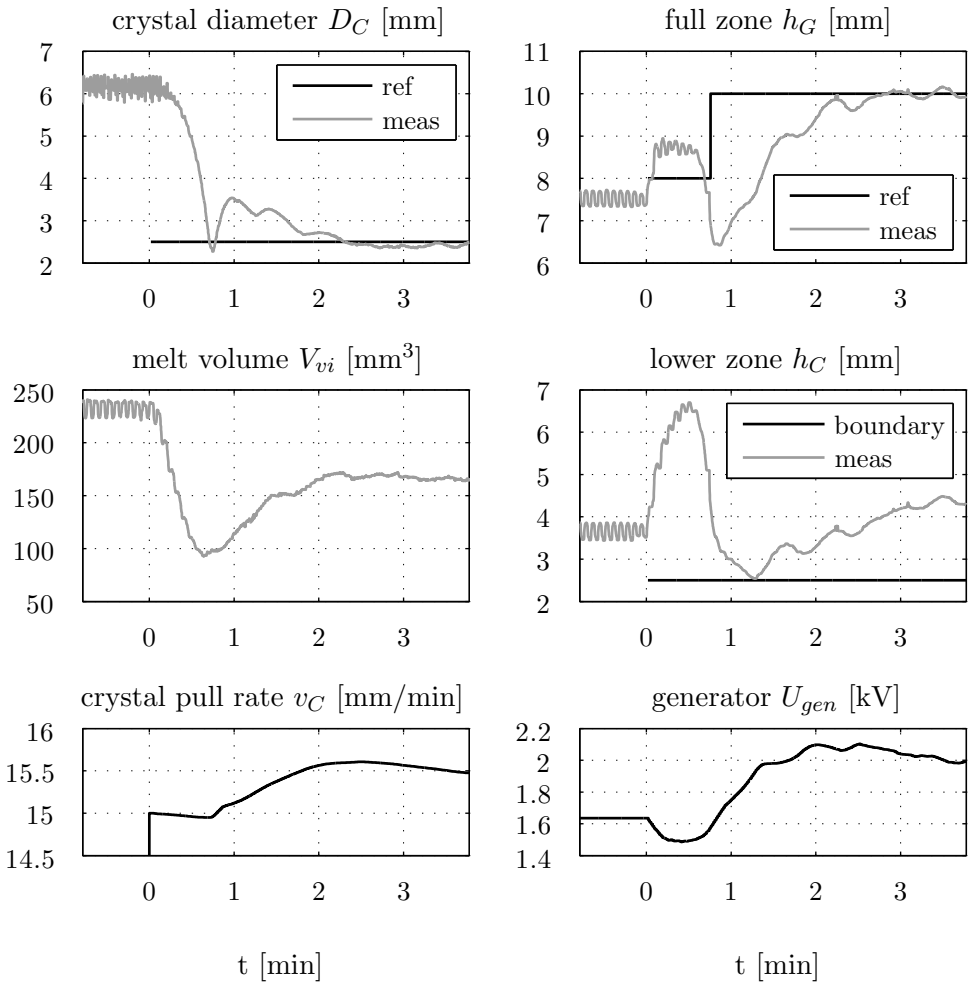

(b) Time plot

Figure 5.8.: Regulated growth of a thin neck with a reference of 2.5 mm in diameter. The control variables is the generator voltage U_{gen} to fulfill the reference at the zone height h_G and the lower limitation for the lower zone height h_C. The pull rate v_C of the crystal is calculated by using equation 5.5. The feed pull rate v_F is constant at 2.3 mm/min. Before starting the regulation at t=0, the pull rates are off.

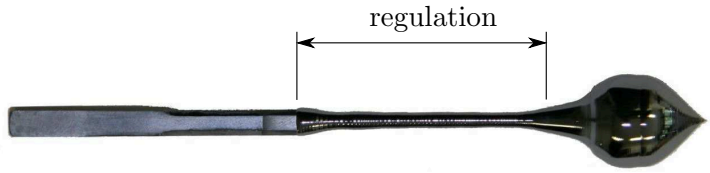

(a) Image

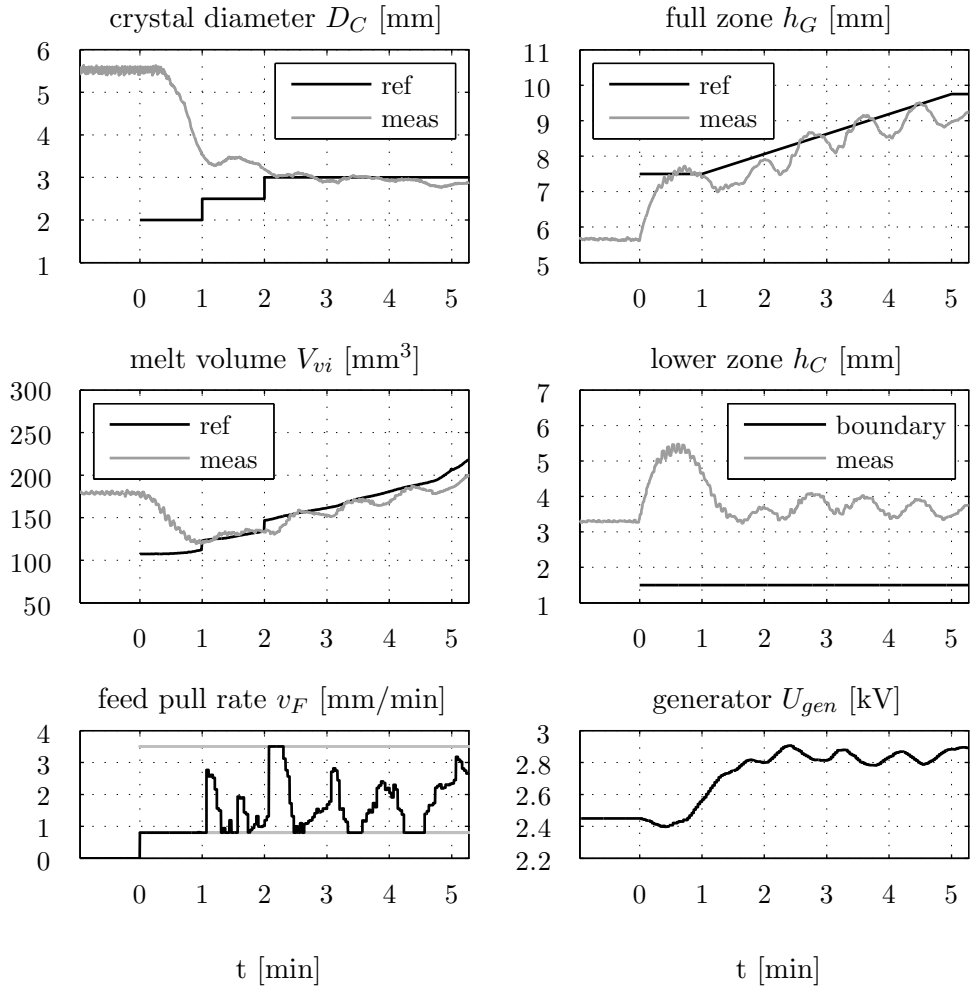

(b) Time plot

Figure 5.9.: Regulated growth of a thin neck with a reference of 3 mm in diameter. Volume reference is calculated based on the trapeze condition involving measured feed diameter, desired crystal diameter, and reference of the full zone height. The control variables are the generator voltage U_{gen} and the pull rate v_F of the feed. The rate v_F has to be in its limitations $0.8 \leq v_F \leq 3.5$ mm/min. The crystal pull rate v_C is constant at 8 mm/min. Before starting the regulation at t=0, the pull rates are off.

5.4. Regulated Growth of the Crystal Cone (Approach 1)

This section presents two variations to regulate the growth of the crystal cone. In the first one (section 5.4.1),

- generator voltage U_{gen} is adjusted by the model predictive controller to fulfill the reference of the crystal angle φ_C,
- feed pull rate v_F is calculated by a feedforward strategy based on the stationary mass balance.

In the second one (section 5.4.2),

- generator voltage U_{gen} and feed pull rate v_F are adjusted by the model predictive controller using references of full zone height h_G and crystal angle φ_C.

5.4.1. Regulation using the Stationary Mass Balance as Feedforward Component

In this approach, the generator voltage U_{gen} is adjusted by the model predictive controller to satisfy the reference of the crystal angle φ_C. The controller uses a piecewise linear evolution (see section 2.4.4). In other words, a ramp of the heater power is calculated to fulfill the references of the crystal angle φ_C. These ramps generate smooth control actions, which is beneficial for the growth of dislocation-free crystals. The feed pull rate v_F is calculated using the stationary mass balance (see equation 5.1)

$$v_F = v_C \left(\frac{D_C + \kappa_C}{D_F} \right)^2 \tag{5.7}$$

as feedforward component, where D_F and D_C are the measured diameters of feed and crystal, κ_C a diameter offset, and v_C the pull rate of the crystal. The analysis of manually controlled experiments has shown, that the values of the feed pull rate v_F can be reproduced using equation 5.7 and a suitable κ_C. The pull rate v_F is involved in the model prediction as piecewise linear evolution from the current value to the calculated one in a defined time horizon considering the upper and lower limits of the slope. The parameters of the model predictive controller are given in section A.7.4.

A regulated growth experiment of the crystal cone is given in figure 5.10. The regulation begins at the crystal diameter of 30 mm at time point $t = 0$. Here, the current crystal angle φ_C is 15° and its reference 30°. The controller shows, first, an oscillating reaction. After 7 minutes the process is stabilized and a stationary control error of approximately 5° is observed. The control error could be reduced by adjusting the diameter offset κ_C within the feedforward part. During the regulation phase, the melt neck D_N increases and reaches a critical value at the end. It must be noted that the measured value of

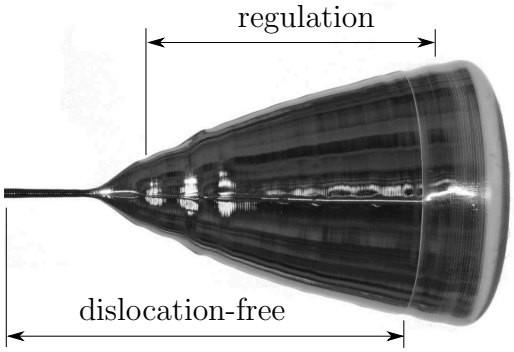

(a) Image of the grown crystal cone of silicon

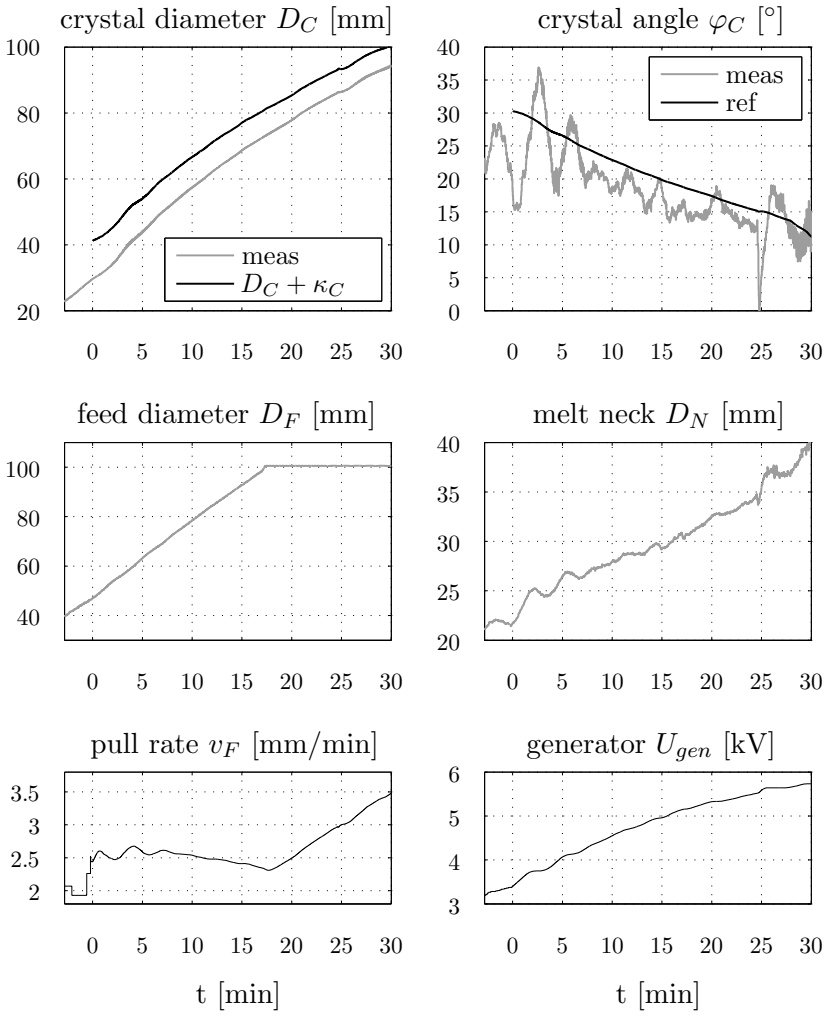

(b) Time plot

Figure 5.10.: Regulated growth of a cone beginning from time point $t = 0$. Feedforward control of the feed pull rate v_F and model predictive control of the crystal angle φ_C adjusting the generator voltage U_{gen}. Dislocations appeared at time point $t = 25$ min because of arcing.

D_N is only an approximation due to the visibility problems produced by the inductor. Therefore, it is not recommended to use the measurement of the melt neck D_N within the controller. But its possible to achieve sufficient values of melt neck D_N and crystal angle φ_C by finding suitable angle references and suitable values of κ_C. Furthermore, figure 5.10 shows the control reaction to a strong disturbance. At time point $t = 25$ min, the crystal looses its dislocation-free structure due to arcing. Arcing is a corona discharge at the inductor and occurs at high voltages. The reason for arcing is not known in this experiment, but it can be assumed to be independent of the regulation. However, the regulation stabilized the process having been disturbed by arcing, so that the process could be terminated in stable conditions without leakage of the melt or cracking of the crystal. To examine the reproducibility of the regulation, two further experiments were conducted. Figure 5.11 shows two dislocation-free crystals of silicon grown by the regulation. In the cylindrical part of the second crystal (b), step attempts of heater power and pull rates were made to investigate the dynamics.

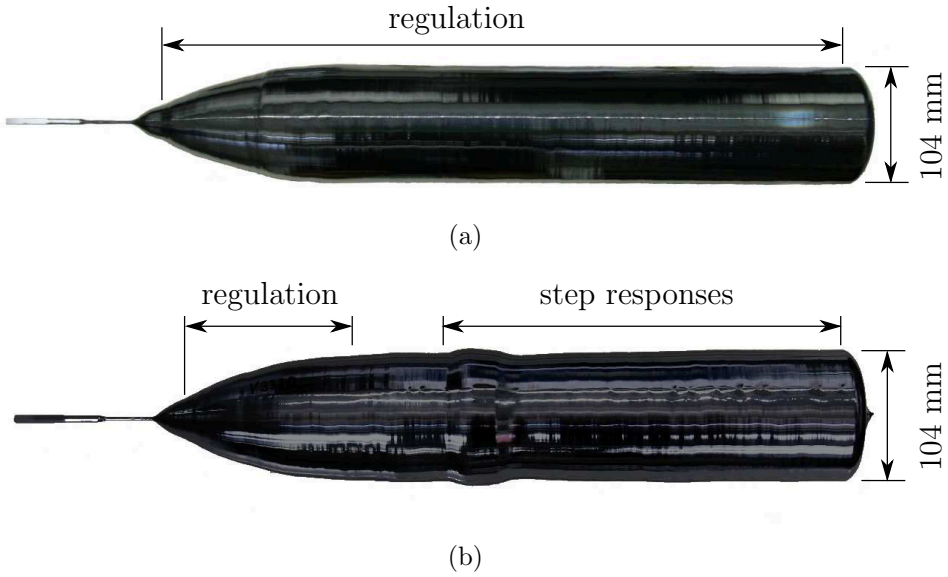

Figure 5.11.: Dislocation-free crystals of silicon grown by the regulation. Feedforward control of the feed pull rate v_F and model predictive control of the crystal angle φ_C adjusting the generator voltage U_{gen}. In the cylindrical part of crystal (b), several step responses were measured to investigate the dynamics.

5.4.2. Full Regulation by Predictive Control

To benefit from the advantages of the FZ modeling, it is obvious to calculate both, the heater power and the feed pull rate by the predictive controller. The coupled process quantities of feed rod, crystal, and molten zone can be directly considered within the regulation. References of the zone height h_G and

the crystal angle φ_C are used to ensure stable growth conditions. The model of the melt neck D_N (see section 4.1.4) shows a proportional relation to the zone height. For a suitable reference of the zone height, a proper melt neck can be expected. The parameters of the model predictive controller are given in section A.7.5.

Figure 5.12 shows a regulation experiment starting at $t = 0$. The predictive controller calculates ramps of feed pull rate v_F and generator voltage U_{gen} to satisfy the references. These ramps generate smooth evolutions of the control variables, which is beneficial for the growth of dislocation-free crystals. The controller uses a prediction horizon of 5 minutes and shows a high control precision. At time point $t = 11$ minutes, the feed rod is changed form the tapered shape to the constant diameter. The change of the geometrical and thermodynamical conditions is considered within the prediction. A temporary error of the crystal angle of 3° is observable. In this experiment, the peak in the measurements of the zone height h_G at 11 minutes results from measuring problems due to the changing shape of the feed rod. But this effect is negligible within the control due to the short time of appearance. The diameter D_N of the melt neck is in a proper range during the growth process. The regulation starts at a crystal diameter of 46 mm.

5.4.3. Regulation of the Landing Phase

This section presents the regulation of the landing phase, where the crystal cone is swinging into the cylindrical part. The controller references are the crystal diameter and the zone height. The predictive controller calculates the heater power to satisfy the desired zone height h_G. The feed pull rate v_F is determined by the stationary mass balance

$$v_F = v_C \left(\frac{D_C}{D_F} \right)^2 \tag{5.8}$$

where v_C is the pull rate of the crystal, D_C the final diameter of the crystal, and D_F the measured diameter of the feed rod. The pull rate v_F is not directly set to the calculated value. To achieve a smooth change, a linear evolution to the calculated one is used considering the upper limit of $\Delta v_{F,ub} = +0.1$ mm/min^2. The parameters of the model predictive controller are given in section A.7.6.

Figure 5.13 shows the time plot of an experiment. The crystal diameter shows an overshooting which is observable by manual growth as well. It can be reduced by adjusting the reference values, or reducing the maximum slope of the rate v_F, or considering the crystal angle within the regulation. The crystal diameter shows a steady-state control error of 0.7 mm. The measurements can be expected as exact, because the control error was confirmed by re-measuring the crystal afterward. A cause of the control error could be the implementation of the pull rates. The technical and mechanical requirements to the pull rates

are very high and a realization with a high precision is sophisticated. To eliminate the control error, appropriate methods can be used such as offset-free tracking presented in the book by Maciejowski [Mac02]. The idea of the offset-free tracking is to estimate the prediction error between model and process first and then to consider it in the calculations of the controller.

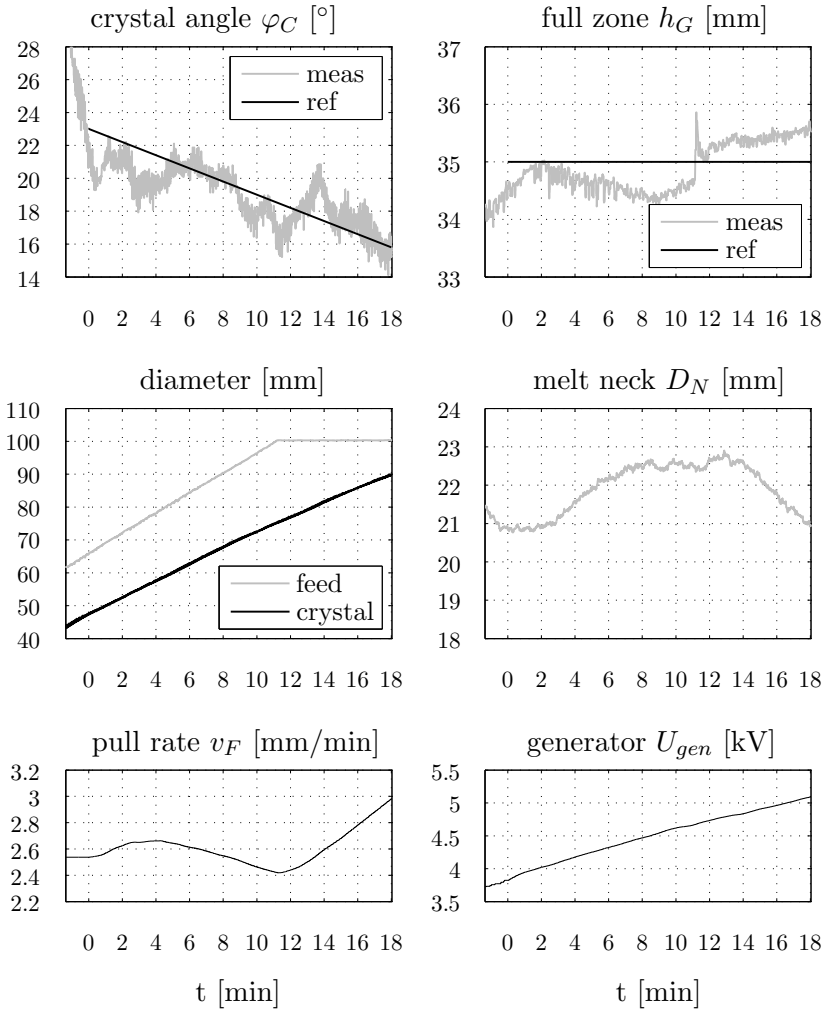

Figure 5.12.: Regulated growth of the crystal cone with a finale diameter of 104 mm. The feed pull rate v_F and the generator voltage U_{gen} are adjusted by the predictive controller to satisfy references of the zone height h_G and the crystal angle φ_C.

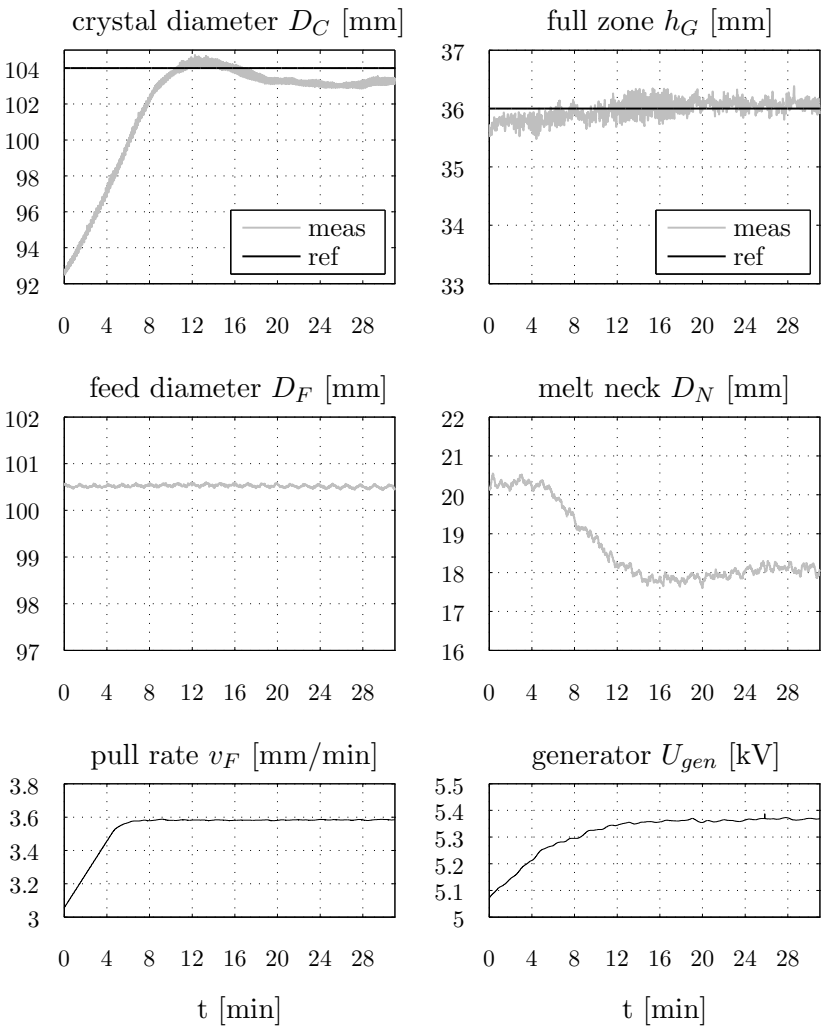

Figure 5.13.: Regulation of the landing phase. The crystal cone is swinging into the cylindrical part with an target diameter of 104 mm.

5.5. Regulated Growth of the Crystal Cone (Approach 2)

In this approach, the complete crystal shape, starting from the cone, is defined as function of the crystal length L_C. The separation of phases concerning different reference values is omitted. References are the crystal diameter D_C and the full zone height h_G. In the next sections, two regulated growth experiments are presented. First, the growth of a crystal with 150 mm in diameter. Second, the growth of a crystal with a special shape, the so-called Avogadro crystal. In the experiments, different inductors are applied, but the controller uses the model parameters identified in section 4.4. A renewed parameter identification was not executed. In both experiments, the regulation starts at a crystal diameter of approximately 40 mm. Before, the growth has been done manually.

5.5.1. Crystal with 150 mm in Diameter

Figure 5.14 shows the used reference to grow a crystal with a diameter of 150 mm. Shown is the desired crystal diameter D_C as function of the crystal length L_C. The predictive controller uses a piecewise linear development of generator voltage U_{gen} and pull rate v_F. Upper and lower limits of the slope of the input variables ΔU_{gen} and Δv_F are shown in figure 5.14 as well. For diameter smaller then 135 mm, it is not allowed to reduce the heater power to avoid the risk of dislocation creation. Afterwards the controller is able to reduce slightly the power to fulfill the references. Also here, the upper limit of the power is decreased to avoid an aggressive controlling of the power. Only a slight adjustment of the feed pull rate v_F at diameter smaller then 50 mm is allowed to ensure a smooth development of the pull rate. The references of the crystal diameter and limits of the input variables are defined by sample points (marked with circles in figure 5.14). Between these sample points a linear interpolation is used. The parameters of the model predictive controller are given in section A.7.7.

Figure 5.15 shows the development of the main measurements over time. The automation starts at crystal diameter D_C of 40 mm using a constant reference of the zone height h_G of 36.1 mm. After activating the regulation, the controller adjust feed pull rate v_F and generator voltage U_{gen} to fulfill references of crystal diameter D_C and full zone height h_G. As mentioned in section 3.5, an upper limit for the crystal pull rate v_C exists to ensure dislocation-free growth. A high crystal pull rate v_C may result in a high thermal stress in the crystal. If a critical stress is reached, than dislocations can appear or the crystal can crack. Therefore, v_C is slowly reduced from 3.4 mm/min to 2.6 mm/min during the cone phase. This is manually done and orientated at the crystal diameter D_C.

Figure 5.16 (a) gives the control error (the difference between reference and measurement) of crystal diameter D_C and full zone height h_G over crystal length L_C. The regulation starts with a control error (error = meas - ref)

of -1.5 mm of crystal diameter and -1.0 mm of zone height. The controller overcomes these differences in approximately 17 minutes ($\Delta L_C \approx 60$ mm). Then, the regulation shows a precise performance. Both, crystal diameter D_C and zone height h_G have a control error in the range of ± 0.5 mm. In the cylinder phase, the crystal diameter shows a steady-state control error of 0.3 mm. The regulation does not produce an overshooting of the crystal diameter, such as in section 5.4.3.

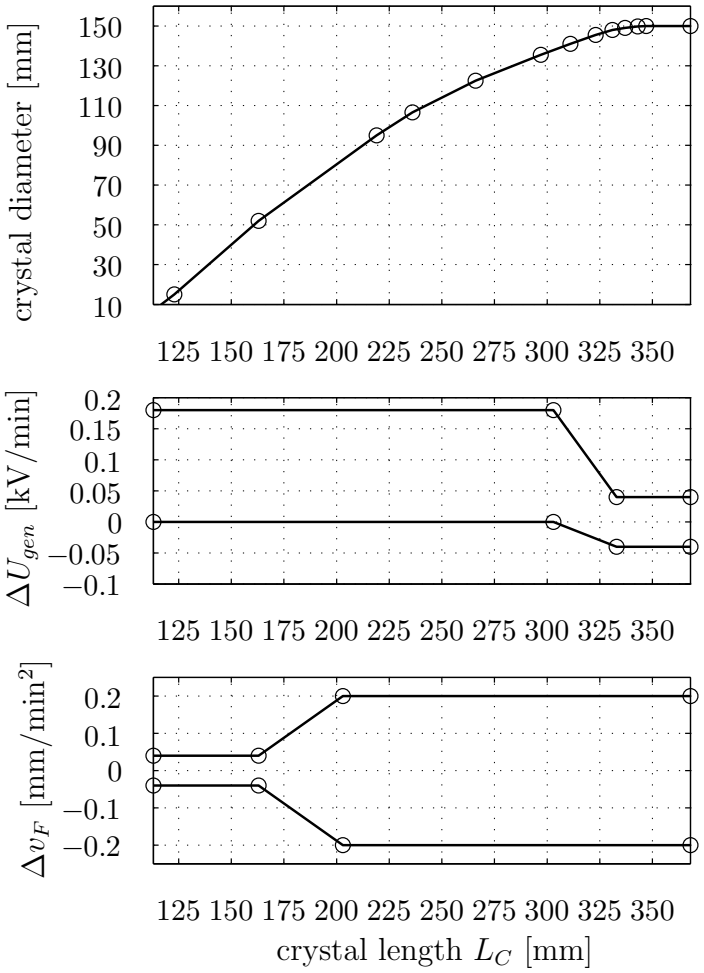

Figure 5.14.: Reference of the crystal diameter D_C as function of the crystal length L_C. Upper and lower limit of the slope of the input variables: generator voltage ΔU_{gen} and pull rate of the feed rod Δv_F. References and limits are defined by sample points (marked with circles). Between these sample points a linear interpolation is used.

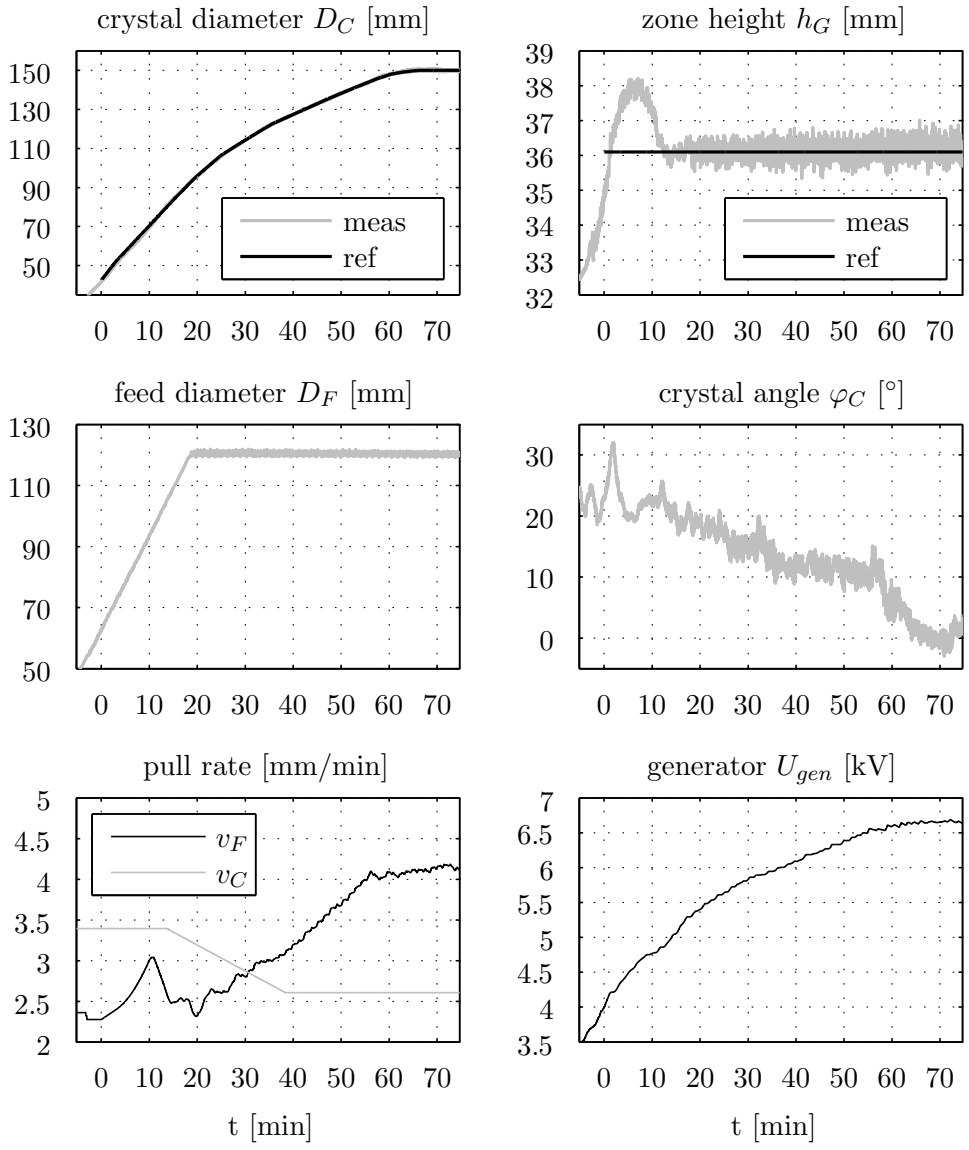

Figure 5.15.: Regulated growth of a 150 mm crystal of silicon starting from time point $t = 0$. The model predictive controller adjust feed pull rate v_F and generator voltage U_{gen} to fulfill references of crystal diameter D_C and full zone height h_G. The pull rate of the crystal v_C is slowly reduced from 3.4 mm/min to 2.6 mm/min during the cone phase. This is manually done and orientated at the crystal diameter D_C.

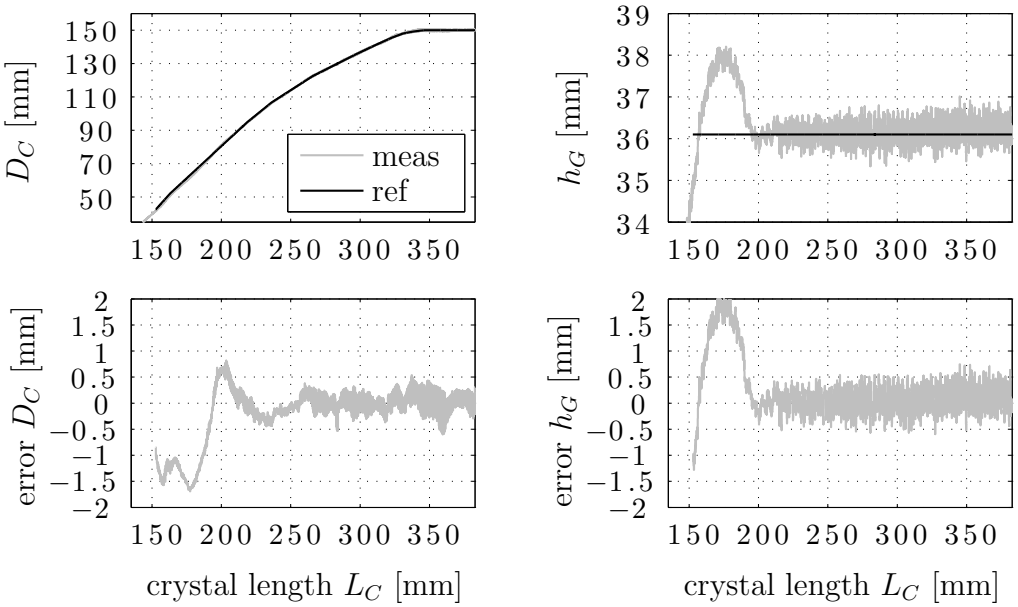

(a) Control error of crystal diameter D_C and full zone height h_G

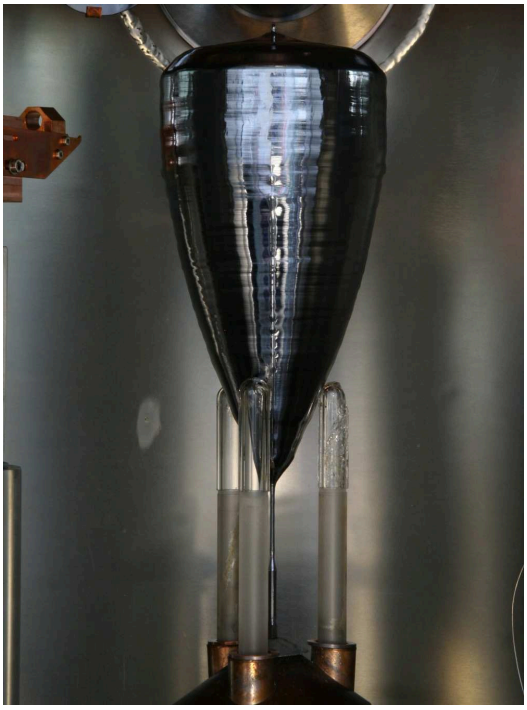

(b) Image of the crystal

Figure 5.16.: Grown crystal with 150 mm in diameter using regulation

5.5.2. Avogadro Crystal

This section presents the regulated growth of a crystal with a special shape, the so-called Avogadro crystal. The crystal is used in an approach to determine the Avogadro constant by "counting" the atoms of a 1 kg monocrystalline sphere of ^{28}Si isotope. Details of the physical background are given in the reviews of Broys et al. [Bor07], Becker et al. [Bec09], and Becker and Schiel [Bec13].

Two silicon spheres have to be obtainable from one grown crystal. Due to the high cost of the material, a regulation is applied to grow a crystal with an economical wastage of the material. Figure 5.17 shows the determined shape of the crystal including the two spheres. In this crystal shape no cylindrical part with a constant diameter existed. The diameter has to be decreased after finishing the cone and increased again up to the full diameter. A regulation is needed to fulfill this reference of the shape. In the scope of this thesis, the model-based regulation technique has been used to prove a possible application. Here, a common feed rod of polycrystalline silicon is used instead of the expensive ^{28}Si material.

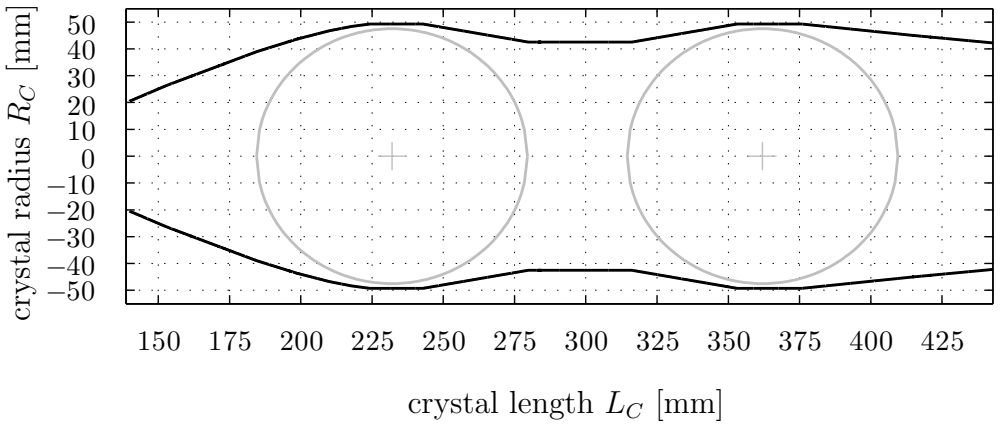

Figure 5.17.: Shape of the Avogadro crystal including the two spheres

Figure 5.18 shows the development of the main measurements over time. The parameters of the model predictive controller are given in section A.7.8. The automation starts at crystal diameter D_C of 42 mm using a constant reference of the zone height h_G of 31.6 mm. Figure 5.19 presents the control error of crystal diameter D_C and full zone height h_G as function of crystal length L_C. In the cone phase, the regulation shows a precise performance comparable to the regulated growth of the 150 mm crystal. Both, crystal diameter D_C and zone height h_G have a control error in the range of ± 0.5 mm. An error of approximately -1 mm in diameter can be seen during the phases of decreasing the crystal diameter. A reason is the modeling, for instance of the crystal angle. Here, the focus was putted on the cone phase where only increasing diameters and positive angles are notable. Two Avogadro crystals are successfully grown

using the regulation. Figure 5.20 shows an image of an Avogadro crystal. Two experiments of growing the first part of the Avogadro crystal running at another FZ machine are successfully done too. A comparable control error has been reached.

The conclusion is that the model predictive controller is useable for growing several crystals (such as 150 mm and Avogadro crystals) using different FZ machines without renewed parameter identification.

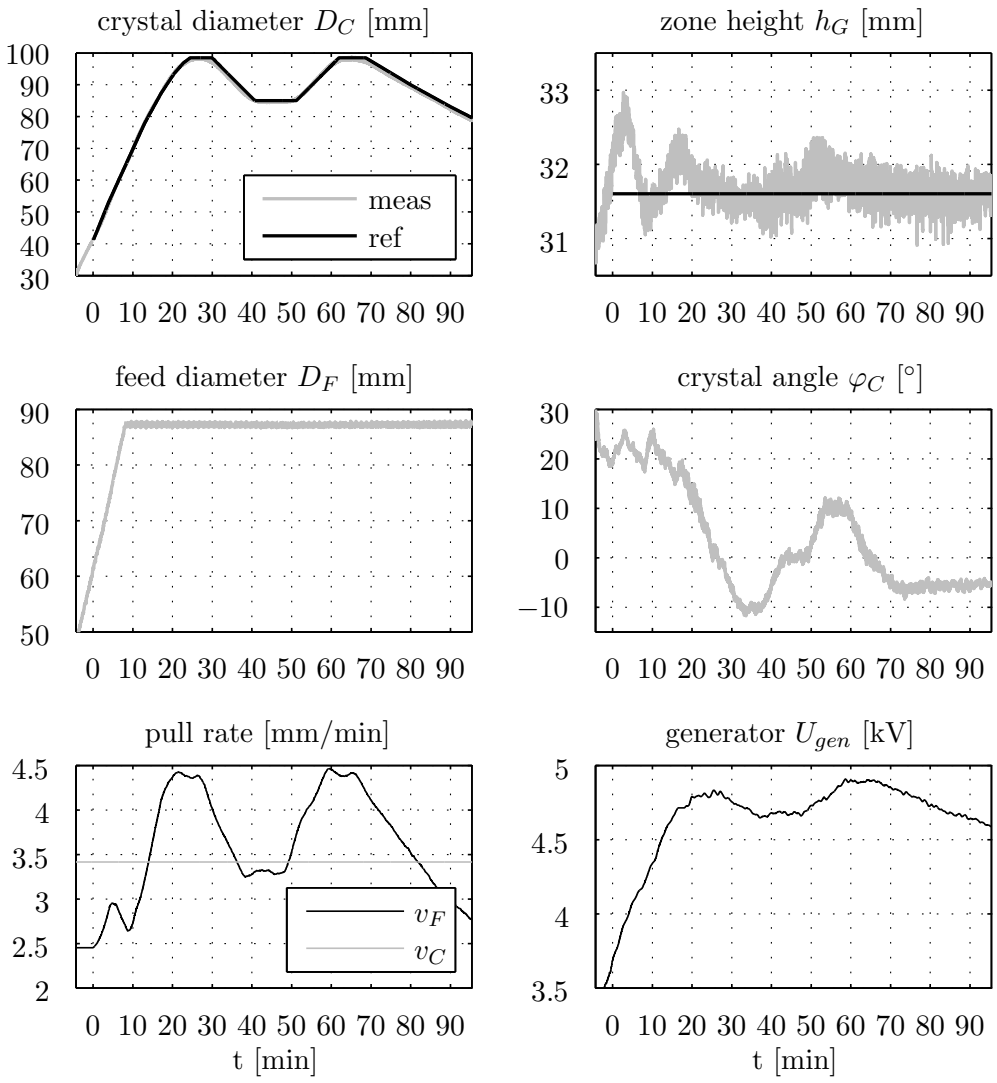

Figure 5.18.: Regulated growth of the Avogadro crystal of silicon starting from time point $t = 0$. The model predictive controller adjust feed pull rate v_F and generator voltage U_{gen} to fulfill references of crystal diameter D_C and full zone height h_G.

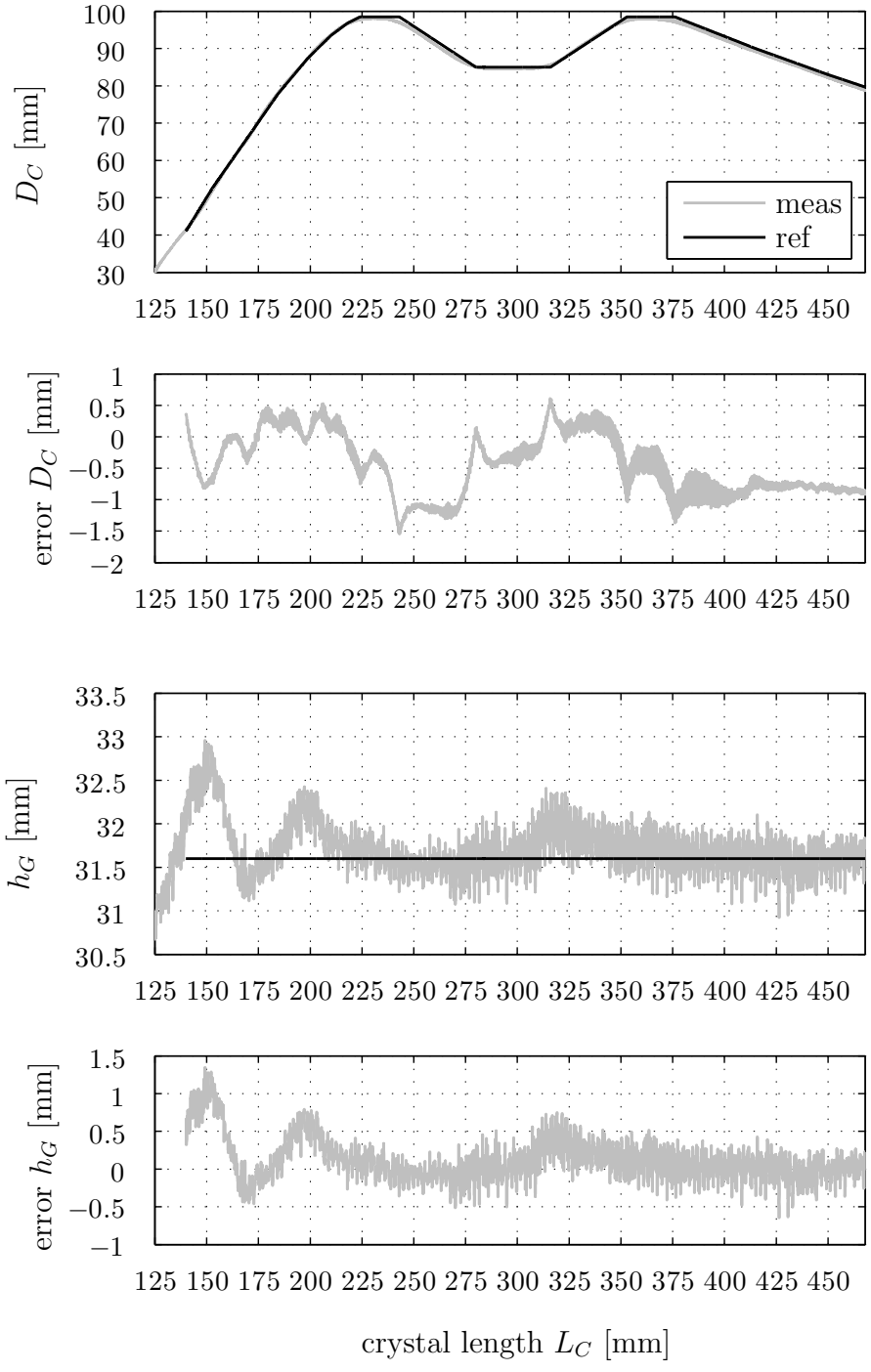

Figure 5.19.: Regulated growth of the Avogadro crystal of silicon. Control error of crystal diameter D_C and full zone height h_G.

Figure 5.20.: Image of the grown Avogadro crystal using regulation. The image was taken by Turschner at the Leibniz Institute for Crystal Growth (IKZ).

6. Conclusion

In this thesis, a model-based automation concept was developed to regulate the FZ process including the following phases: forming the feed tip, creating the thin neck, making the cone and growing the cylinder. The focus was on modeling the process dynamics and identifying suitable trajectories for a stable process control.

A measurement system was created to obtain the geometrical quantities based on visual image processing. Digital cameras were applied to capture the process. The acquired images were analyzed by gradient-based methods. A frequency of 10 analyzed frames per second was realized on a standard PC. Camera images of the feed rod are used, among other things, to determine an approximation of the feed residual. Furthermore, the deflection of the solid-liquid interface was analyzed and a formula was determined to approximate height and volume of the bowl of molten silicon being invisible during the process. The interfaces were visualized by the LPS method. The modeling of the melt volume has shown that both volumes, the one of the feed residual and that of the melt bowl, are not negligible because of their significant effect on the melt dynamics. A model-based state estimation technique, the Kalman filter, and a model predictive controller were implemented to regulate the process. To use those methods, a nonlinear low-order model had to be developed including the geometrical and thermodynamical aspects.

The presented model in this thesis is the main contribution for the intended automation of the complete FZ process and has not being developed before. The deduction of the differential equations is given and the validity was examined by comparison with experimental data. The model allows the prediction of the radii and angles of feed and crystal, the upper and lower zone heights, the melt volume, the melt neck, and the rates of melting and growing. The control variables of the model are the heater power and the pull rates of feed and crystal. The computation time is less than a second to predict the process behavior for up to 5 minutes. Surprisingly, the model is suitable for the main phases: the thin neck, the cone, and the cylindrical phase. A prediction horizon of several minutes can be provided with sufficient accuracy.

An automation was developed for forming the feed tip using a PI controller. This provides reproducible start conditions for the growth of the thin neck Two regulation strategies were successfully applied for creating the thin neck using the model-based concept. The first one used heater power and crystal pull rate to stabilize the process, the second one heater power and feed pull rate.

The regulated growth beginning from the cone and swinging into the cylindrical phase was realized using references of zone height, diameter and angle of the crystal. The model accuracy allows a predictive control without additional con-

troller components such as a PID controller. The model predictive controller calculated ramps of the heater power and the feed pull rate to satisfy these references. The ramps generated smooth evolutions of the control variables, which was beneficial for the growth of dislocation-free crystals. Experiments showed a high control precision. With this automation concept, dislocation-free crystals with different diameters were grown on two FZ machines without a renewed parameter identification. Because of the reproducibility of the process conditions, it can be expected that dislocations would be generated less often than with a manual control, where the operator is not able to re-run the process as precise as this control concept does.

7. Outlook

The automation of the following two phases of the FZ process have not been regarded during this work: finishing the crystal and growing the crystal cone up to a diameter of 15-20 mm after finishing the thin neck (this phase is denoted as *establishing the molten zone*). To realize a complete automation of the crystal growth by FZ technique, these phases have to be investigated with respect to control engineering. It is highly probable that the concept of the model predictive control can also be used here.

In an industrial setting, additional components such as reflector rings are used to improve the melting behavior of the feed material. These components mounted on top of the inductor reduce the visibility of the upper zone. In this case, not all quantities (for instance the diameter of the feed rod) are directly available. Therefore, these quantities have to be calculated or estimated by the observer.

Better results for the control accuracy of crystal angle and zone height are expected with the improvement of the model. The influence of hole and slits of the inductor could be modeled. Especially in the beginning of the cone phase, improved control accuracy could be reached. The strength of the predictive control could be more intensively exploited by considering constraints such as limitations of the melt neck. Adaptive control approaches could be investigated to improve the flexibility according different FZ setups.

The automation could be applied to investigate required process conditions for dislocation-free growth. Especially, the swing from the cone into the cylindrical part is very sensitive. Here, the automation could help to find suitable trajectories. The growth rate and the pull rate of the crystal could be used within the regulation to satisfy the trajectories.

A. Appendix

A.1. Heat Dissipation from a Solid Cylinder in Contact with Melt

In this section, an equation for the power loss of a heated cylinder is constructed. As shown in figure A.1, the cylinder bottom is heated to the melting temperature T_m and a flat crystallization interface, an infinity length, cold surroundings (T=0 K) and a temperature-independent surface emissivity are assumed. The calculation bases on the analytical equation of the surface temperature profile determined by Billig [Bil55].

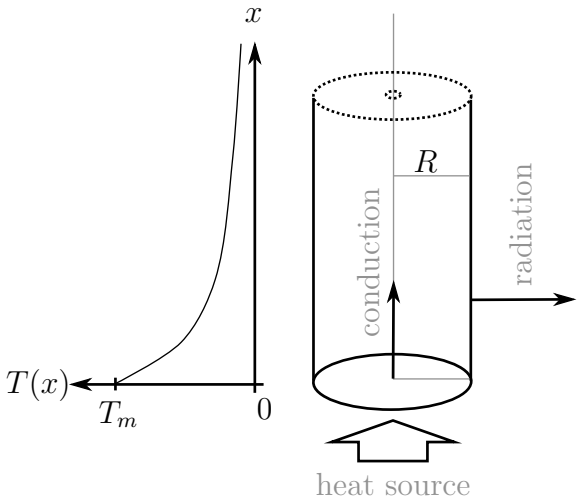

Figure A.1.: Model for the calculation of the temperature profile $T(x)$ by Billig. The bottom of a semi-infinite cylinder with a flat crystallization interface is heated up to melting temperature T_m. The cylinder has a constant radius R.

Billig uses the equation of the heat conduction W

$$W = -A\lambda_T \frac{dT}{dx} \tag{A.1}$$

along the cylinder and the heat radiation from an infinitesimal element dx of its surface

$$dW = -\epsilon\sigma T^4 U dx \tag{A.2}$$

to determine a second-order differential equation of the temperature T

$$\frac{d^2T}{dx^2} = \frac{2\epsilon\sigma}{\lambda_m T_m R} T^5 \quad . \tag{A.3}$$

Here, x is the distance to the heater, R the cylinder radius, A the cylinder cross-section, U the cylinder circumference, ϵ the surface emissivity, λ_T the

thermal conductivity depending on temperature T, λ_m the thermal conductivity at melting temperature T_m, and σ=$5.67 \cdot 10^{-8}$ $\frac{W}{m^2 K^4}$ the Stefan-Boltzmann constant. Billig approximates the thermal conductivity λ_T

$$\lambda_T = \lambda_m \frac{T_m}{T} \tag{A.4}$$

inverse proportional with the temperature T. The differential equation A.3 can be analytical solved by the Emden-Fowler equation. The temperature profile as function of x is determined by the equation

$$T(x) = a_0 (x + a_1)^{-\frac{1}{2}} \quad , \tag{A.5}$$

$$a_0 = \Big(\frac{3\lambda_m T_m R}{8\epsilon\sigma}\Big)^{\frac{1}{4}} \quad , \tag{A.6}$$

$$a_1 = \frac{a_0^2}{T_m^2} \quad . \tag{A.7}$$

The temperature gradient at the solid-liquid interface is

$$\left.\frac{dT}{dx}\right|_{x=0} = -\Big(\frac{2\epsilon\sigma T_m^5}{3\lambda_m R}\Big)^{\frac{1}{2}} \quad . \tag{A.8}$$

To obtain the power loss of the complete cylinder, the loss of a infinitesimal element dx has to be integrated over the infinity length of the cylinder. The temperature profile $T(x)$ by Billig is used within the integration. The power loss P_{loss}(R) is calculated by

$$P_{loss}(R) = 2\pi R\epsilon\sigma \int_0^\infty T^4(x)\,\mathrm{d}x \quad , \tag{A.9}$$

$$= 2\pi R\epsilon\sigma \frac{a_0^4}{a_1} \quad , \tag{A.10}$$

$$= \underbrace{\Big(\frac{3\pi^2 \lambda_m T_m^5 \epsilon\sigma}{2}\Big)^{\frac{1}{2}}}_{\zeta_{lost}} R^{\frac{3}{2}} \quad . \tag{A.11}$$

	Unit	Description	Silicon	Germanium
T_m	[K]	melting temperature	1683	1211
λ_m	$[\frac{W}{m \cdot K}]$	thermal conductivity at melting point	21.6	17.3
ϵ	[-]	surface emissivity (solid)	0.46	0.55
ζ_{lost}	$[\mathrm{kW} \cdot \mathrm{m}^{-\frac{3}{2}}]$	power loss constant	335.59	161.16

Table A.1.: Material parameters of silicon and germanium to calculate the temperature profile and the power loss of a heated cylinder

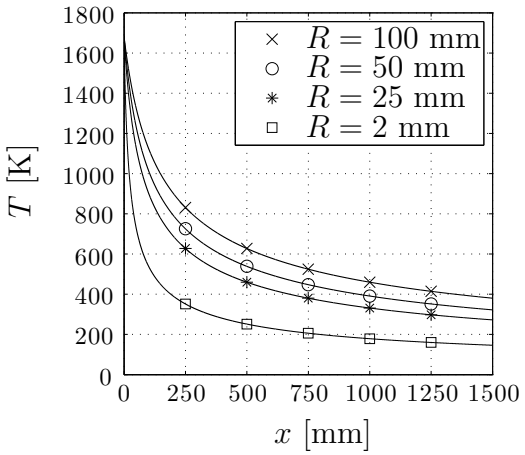

(a) Temperature profiles $T(x)$ for different cylinder radii R calculated by equation A.5

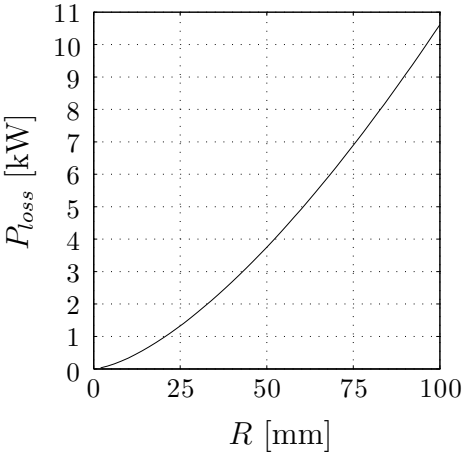

(b) Power loss P_{loss} as function of the cylinder radius R calculated by equation A.11

Figure A.2.: Temperature profiles $T(x)$ and power loss P_{loss} of silicon cylinder based on the calculations by Billig

A.2. Laplace-Young Problem

The Laplace-Young equation (see Coriell and Cordes [Cor77])

$$\underbrace{P_0}_{\substack{\text{pressure}\\ \text{difference}}} - \underbrace{\rho_M g z}_{\substack{\text{hydrostatic}\\ \text{pressure}}} + \underbrace{\frac{1}{2}\rho_M r^2 \Omega^2}_{\substack{\text{centrifugal}\\ \text{pressure}}} + \underbrace{F_n}_{\substack{\text{electro-}\\ \text{magnetic}\\ \text{pressure}}} = \underbrace{\gamma \cdot K}_{\substack{\text{capillary}\\ \text{pressure}}} \tag{A.12}$$

describes the capillary pressure difference at the interface between melt and vapor. Here, the involving variables are the pressure difference P_0 between a reference point in the melt and the ambient pressure, the melt density ρ_M, the gravitational acceleration g, the radial coordinate r, the vertical coordinate z, the rate of rotation Ω, the electromagnetic pressure F_n, the surface tension γ and the curvature K. Assuming rotational symmetry, the curvature K can be calculated by

$$K = \frac{d\varphi'}{ds} + \frac{sin(\varphi')}{r} \tag{A.13}$$

or

$$K = -\frac{d\varphi}{ds} + \frac{cos(\varphi)}{r} \tag{A.14}$$

using $\varphi' = 90° - \varphi$. Here, s is the arc length. A sketch of the angles φ and φ' is given in figure A.3. The Laplace-Young equation A.12 can be transformed

into a system of three nonlinear differential equations

$$\frac{dr(s)}{ds} = sin(\varphi) \tag{A.15}$$

$$\frac{dz(s)}{ds} = cos(\varphi) \tag{A.16}$$

$$\frac{d\varphi(s)}{ds} = \frac{cos(\varphi)}{r} + \frac{\rho_M g z}{\gamma} - \frac{\rho_M r^2 \Omega^2}{2\gamma} - \frac{F_n(s)}{\gamma} - \frac{P_0}{\gamma} \quad , \tag{A.17}$$

involving the initial values $r(0) = R_C$, $z(0) = 0$ and $\varphi(0) = \varphi_M$. The solution of the differential equations delivers the shape of the molten zone. The pressure difference P_0 is used to fit the shape to experimental data such as melt volume V_{vi} and melt neck R_N.

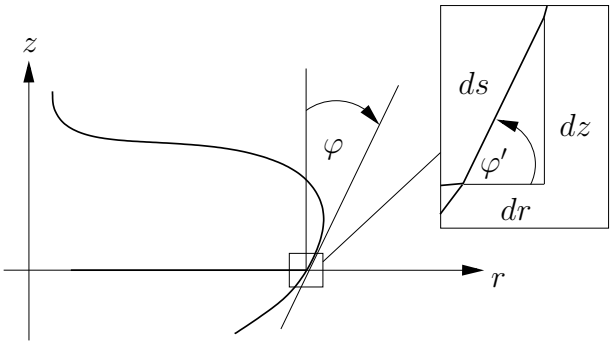

Figure A.3.: Sketch of the shape of the molten zone

Explicit Formulation of the half-plane Shape

Landau and Lifshitz derive in [Lan87] an explicit equation for an up-pulling liquid shape by the contact with a solid body. Analog to Landau and Lifshitz, this section gives an explicit equation for the melt shape $x = x(z)$ under the assumption of a constant melt height h_m for $x \to -\infty$. As shown in figure A.4, the melt shape has a horizontal evolution of the melt height at infinity. Please consider that the rotational direction of the melt angle φ_M is opposite to the mathematical positive direction.

In the following equations the capillary constant

$$\alpha = \sqrt{\frac{2\gamma}{\rho_M g}} \quad , \tag{A.18}$$

appears, which has the dimension of length and is calculated from surface tension γ, gravitational acceleration g, and melt density ρ_M. Silicon has a capillary constant of $\alpha_{Si} = 7.94$ mm.

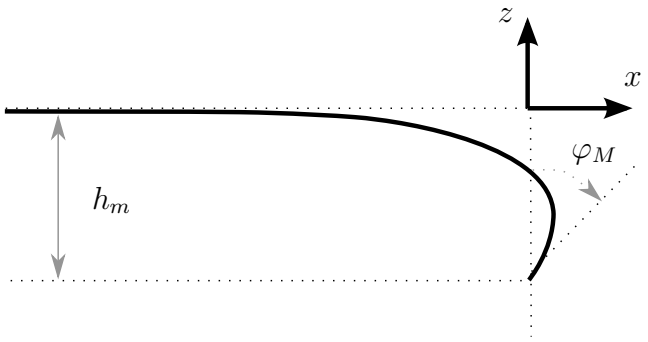

Figure A.4.: Sketch of the melt shape in a half-plane.

Neglecting the centrifugal and the electromagnetic pressure within the Laplace-Young equation leads to the equation

$$P_0 - \rho_M g z = \gamma K \quad . \tag{A.19}$$

The two-dimensional curvature K is defined as

$$K = \frac{1}{R_1} + \frac{1}{R_2} \tag{A.20}$$

and in the half-plane, the radii are $R_1 = \infty$ and $R_2 = -\frac{(1+z'^2)^{\frac{3}{2}}}{z''}$. Therefore, the Laplace-Young equation in the half-plane is given by

$$\frac{P_0}{\gamma} - \frac{\rho_M g z}{\gamma} = -\frac{z''}{(1+z'^2)^{\frac{3}{2}}} \quad . \tag{A.21}$$

As shown in figure A.4, the vertical coordinate $z(x)$ and its first $z'(x)$ and second $z''(x)$ derivatives are zero for $x \to -\infty$. Which means that P_0 has to be zero too, to fulfill equation A.21. That leads to the equation

$$\frac{2z}{\alpha^2} = \frac{z''}{(1+z'^2)^{\frac{3}{2}}} \quad . \tag{A.22}$$

The indefinite integration of both sides ($\int \ldots dz$) gives the following equation

$$\frac{z^2}{\alpha^2} = -\frac{1}{\sqrt{1+z'^2}} + c_1 \tag{A.23}$$

with the constant of integration c_1. The constant $c_1 = 1$ can be obtained using the conditions $z(x) = 0$ and $z'(x) = 0$ for $x \to -\infty$. Rearranging equation A.23 gives

$$z' = \frac{\sqrt{2 - \frac{z^2}{\alpha^2}}}{\frac{\alpha}{z} - \frac{z}{\alpha}} \quad . \tag{A.24}$$

The relations $z^{'} = dz/dx$ and $1/z^{'} = dx/dz = x'$ lead to the formula

$$x^{'}(z) = \frac{\frac{\alpha}{z} - \frac{z}{\alpha}}{\sqrt{2 - \frac{z^2}{\alpha^2}}} \quad . \tag{A.25}$$

The integration $\int x^{'}(z)dz$ using equation A.25 gives an explicit formula for the calculation of $x(z)$

$$x(z) = -\frac{\alpha}{\sqrt{2}} \cdot arcosh(\sqrt{2}\frac{\alpha}{z}) + a\sqrt{2 - \frac{z^2}{\alpha^2}} \quad . \tag{A.26}$$

As shown in figure A.4, the angle φ is defined by $x'(z) = tan(-\varphi)$. This leads to

$$z'(x) = \frac{1}{tan(-\varphi)} = \frac{cos(-\varphi)}{sin(-\varphi)} \tag{A.27}$$

Inserting in equation A.23 gives

$$\frac{z^2}{\alpha^2} = 1 - \frac{1}{\sqrt{1 + \frac{cos^2(-\varphi)}{sin^2(-\varphi)}}} \tag{A.28}$$

$$= 1 - sin(-\varphi) \tag{A.29}$$

$$= 1 + sin(\varphi) \quad . \tag{A.30}$$

This leads to an explicit formula to describe the angle φ

$$sin(\varphi) = \frac{z^2}{\alpha^2} - 1 \quad . \tag{A.31}$$

The melt angle $\varphi_M = \varphi(z = -h_m)$ can be calculated by

$$sin(\varphi_M) = \frac{h_m^2}{\alpha^2} - 1 \quad . \tag{A.32}$$

A.3. Circular Cone Frustum

A circular cone frustum is a cone with a circular base by cutting off the tip of the cone. The top and button of the conical frustum are parallel.

Volume of the frustum V and frustum angle ϕ are calculated by

$$V = \frac{\pi h}{3}(R_1^2 + R_1R_2 + R_2^2) \quad , \tag{A.33}$$

$$tan(\phi) = \frac{R_2 - R_1}{h} \quad , \tag{A.34}$$

where R_1 is the radius of the bottom base, R_2 the radius of the top base, and

h the frustum height.

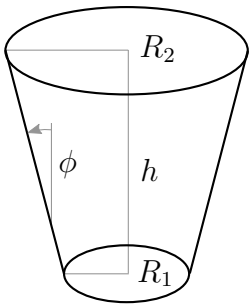

Figure A.5.: Sketch of the circular cone frustum

A.4. Weights: Parameter Identification

A.4.1. Identification of the Kalman Parameter

State	Unit	diagonal element of $\boldsymbol{W}_{QR}$
Feed rod radius R_F	mm	2
Crystal radius R_C	mm	2
Upper zone height h_F	mm	3
Lower zone height h_C	mm	3
Visible melt volume V_{vi}	cm^3	0.5
Melting rate v_{Me}	mm/min	4
Crystallization rate v_{Cr}	mm/min	4
Crystal angle φ_C	°	2
Inductor power P_{ind}	kV	0.5
Melt neck radius R_N	mm	0.5
Feed angle α_F	°	2

Table A.2.: Diagonal elements of the weight matrix $\boldsymbol{W}_{QR}$ used for the parameter identification of the Kalman filter (thin neck and cone phase)

A.4.2. Identification of the Model Parameter

Measurement	Unit	diagonal element of $\boldsymbol{W}_{\Theta}$
Feed rod radius R_F	mm	0
Crystal radius R_C	mm	1
Upper zone height h_F	mm	2
Lower zone height h_C	mm	2
Visible melt volume V_{vi}	cm^3	0
Crystal angle φ_C	°	0
Melt neck radius R_N	mm	0
Feed angle α_F	°	0

Table A.3.: Diagonal elements of the weight matrix $\boldsymbol{W}_{\Theta}$ used for the model parameter identification (thin neck and cone phase)

A.5. Parameter: Kalman Filter

A.5.1. Thin Neck

State	square root of the diagonal element of $\boldsymbol{P}_0$	Unit	square root of the diagonal element of $\boldsymbol{Q}$	Unit
Feed rod radius R_F	0.02	mm	0.014824	mm/s
Crystal radius R_C	0.02	mm	0.0030071	mm/s
Upper zone height h_F	0.05	mm	0.015144	mm/s
Lower zone height h_C	0.05	mm	0.00021597	mm/s
Visible melt volume V_{vi}	0.01	cm^3	4.4259e-009	cm^3/s
Melting rate v_{Me}	0.2	mm/min	0.072693	mm/min/s
Crystallization rate v_{Cr}	0.2	mm/min	0.11629	mm/min/s
Crystal angle φ_C	2	°	0.10397	°/s
Inductor power P_{ind}	0.0001	kV	0.0001	kV/s
Melt neck radius R_N	0.5	mm	0.01	mm/s
Feed angle α_F	2	°	0.24383	°/s

Table A.4.: Thin neck phase: square roots of the diagonal elements of covariance matrix $\boldsymbol{P}_0$ and spectral density matrix $\boldsymbol{Q}$

Measurement	square root of the diagonal element of $\boldsymbol{R}$	Unit
Feed rod radius R_F	0.05564	mm
Crystal radius R_C	0.03124	mm
Upper zone height h_F	0.03788	mm
Lower zone height h_C	0.05162	mm
Visible melt volume V_{vi}	0.00232	cm^3
Crystal angle φ_C	0.26781	°
Melt neck radius R_N	0.00234	mm
Feed angle α_F	0.19877	°

Table A.5.: Thin neck phase: square roots of the diagonal elements of the covariance matrix $\boldsymbol{R}$

A.5.2. Cone

State	square root of the diagonal element of $\boldsymbol{P}_0$	Unit	square root of the diagonal element of $\boldsymbol{Q}$	Unit
Feed rod radius R_F	0.02	mm	0.015289	mm/s
Crystal radius R_C	0.02	mm	0.056313	mm/s
Upper zone height h_F	0.05	mm	0.0078478	mm/s
Lower zone height h_C	0.05	mm	0.0033683	mm/s
Visible melt volume V_{vi}	0.01	cm^3	0.040479	cm^3/s
Melting rate v_{Me}	0.2	mm/min	0.0096804	mm/min/s
Crystallization rate v_{Cr}	0.2	mm/min	0.016047	mm/min/s
Crystal angle φ_C	2	°	0.45075	°/s
Inductor power P_{ind}	0.0001	kV	0.00001	kV/s
Melt neck radius R_N	0.5	mm	0.03846	mm/s
Feed angle α_F	2	°	0.025	°/s

Table A.6.: Cone phase: square roots of the diagonal elements of covariance matrix $\boldsymbol{P}_0$ and spectral density matrix $\boldsymbol{Q}$

Measurement	square root of the diagonal element of $\boldsymbol{R}$	Unit
Feed rod radius R_F	1.00341	mm
Crystal radius R_C	0.99772	mm
Upper zone height h_F	0.46025	mm
Lower zone height h_C	0.28278	mm
Visible melt volume V_{vi}	2.19553	cm^3
Crystal angle φ_C	5.94744	°
Melt neck radius R_N	0.498563	mm
Feed angle α_F	0.60321	°

Table A.7.: Cone phase: square roots of the diagonal elements of the covariance matrix $\boldsymbol{R}$

A.6. Parameter: Low-Order Model

A.6.1. Thin Neck

Parameter	Values	Unit
Density of liquid silicon ρ_M	2.53	kg/cm^3
Density of solid silicon ρ_S	2.34	kg/cm^3
Latent heat of silicon q_0	1803	kJ/kg
Fitting factor a_V (derivative of melt angle)	1	-
Fitting factor a_R (derivative of melt angle)	1	-
Fitting factor a_h (derivative of melt angle)	1	-
Fitting factor a_N (derivative of melt angle)	0	-
Fitting factor n_h (derivative of melt neck)	0	-
Gain factor K_P of the inductor power	1	-
Time constant τ_P of the inductor power	2	s
Power loss constant ζ_{lost} of silicon	335.59	kWm$^{-\frac{3}{2}}$
Fitting factor a_{bo} (derivative of melt volume)	0	-
Fitting factor a_{fr} (derivative of melt volume)	0	-
Polynomial coefficient a_0 of melt bowl volume	0	mm
Polynomial coefficient a_1 of melt bowl volume	0	mm^2
Polynomial coefficient a_2 of melt bowl volume	0	mm
Polynomial coefficient a_3 of melt bowl volume	0	-
Polynomial coefficient d_0 of feed residual volume	0	mm
Polynomial coefficient d_1 of feed residual volume	0	mm^2
Polynomial coefficient d_2 of feed residual volume	0	mm
Polynomial coefficient d_3 of feed residual volume	0	-
Fitting factor p_F of the power P_F	0.95368	-
Fitting factor e_F of the power P_F	2	-
Fitting factor r_F of the power P_F	2	-
Fitting factor f_0 of the power P_F	0.1	-
Fitting factor f_1 of the power P_F	1	-
Fitting factor p_C of the power P_C	0.277888	-
Fitting factor e_C of the power P_C	2	-
Fitting factor r_C of the power P_C	2	-
Fitting factor c_0 of the power P_C	0.1	-
Fitting factor c_1 of the power P_C	2	-
Difference quotients $\Delta\varphi_M/\Delta x_i$ (melt angle)	Table 4.2	-

Table A.8.: Thin neck phase: parameters of the low-order model

A.6.2. Cone

Parameter	Values	Unit
Density of liquid silicon ρ_M	2.53	kg/cm^3
Density of solid silicon ρ_S	2.34	kg/cm^3
Latent heat of silicon q_0	1803	kJ/kg
Fitting factor a_V (derivative of melt angle)	1	-
Fitting factor a_R (derivative of melt angle)	1	-
Fitting factor a_h (derivative of melt angle)	1.3	-
Fitting factor a_N (derivative of melt angle)	0	-
Fitting factor n_h (derivative of melt neck)	-0.9	-
Gain factor K_P of the inductor power	1	-
Time constant τ_P of the inductor power	20	s
Power loss constant ζ_{lost} of silicon	335.59	kWm$^{-\frac{3}{2}}$
Fitting factor a_{bo} (derivative of melt volume)	1.3	-
Fitting factor a_{fr} (derivative of melt volume)	1.3	-
Polynomial coefficient a_0 of melt bowl volume	16	mm
Polynomial coefficient a_1 of melt bowl volume	0	mm^2
Polynomial coefficient a_2 of melt bowl volume	32.48	mm
Polynomial coefficient a_3 of melt bowl volume	1.2	-
Polynomial coefficient d_0 of feed residual volume	5	mm
Polynomial coefficient d_1 of feed residual volume	0	mm^2
Polynomial coefficient d_2 of feed residual volume	18.07	mm
Polynomial coefficient d_3 of feed residual volume	-0.087	-
Fitting factor p_F of the power P_F	3.1504	-
Fitting factor e_F of the power P_F	2	-
Fitting factor r_F of the power P_F	1	-
Fitting factor f_0 of the power P_F	0.05	-
Fitting factor f_1 of the power P_F	1	-
Fitting factor p_C of the power P_C	0.127784	-
Fitting factor e_C of the power P_C	2	-
Fitting factor r_C of the power P_C	1.5	-
Fitting factor c_0 of the power P_C	0.05	-
Fitting factor c_1 of the power P_C	2	-
Difference quotients $\Delta\varphi_M/\Delta x_i$ (melt angle)	Table 4.1	-

Table A.9.: Cone phase: parameters of the low-order model

A.7. Controller Parameter

A.7.1. Feed Tip

Parameter	Values	Unit
K_p	0.022115	kV/mm
K_i	0.0012286	kV/mms
K_d	0	kVs/mm

Table A.10.: Parameters of the PI controller for regulating the zone height h_G (automatic forming of the feed tip)

Parameter	Values	Unit
K_p	0.006	$1/\text{mm}^2\text{min}$

Table A.11.: Parameters of the P controller for regulating the melt volume V_{vi} (automatic forming of the feed tip)

A.7.2. Thin Neck (Approach 1)

Parameter	Values	Unit
Loop time	1	s
H_p	36	s
H_u	36	s
$\Delta U_{gen,lb}$	-0.8	kV/min
$\Delta U_{gen,ub}$	$+0.8$	kV/min
$\boldsymbol{W}_u(U_{gen})$	0	-
$\boldsymbol{W}_x(h_G)$	1	$(1/\text{mm})^2$
$\boldsymbol{W}_s(h_G)$	0	$(1/\text{mm})^2$

Table A.12.: NMPC parameters for regulating the thin neck (approach 1)

segment	U_{gen}	
1	0 - 18 s	piecewise linear
2	18 - 36 s	piecewise linear

Table A.13.: Control points for regulating the thin neck (approach 1)

A.7.3. Thin Neck (Approach 2)

Parameter	Values	Unit
Loop time	1	s
H_p	30	s
H_u	30	s
$\Delta U_{gen,lb}$	-0.7	kV/min
$\Delta U_{gen,ub}$	$+0.7$	kV/min
$v_{F,lb}$	0.8	mm/min
$v_{F,ub}$	3.5	mm/min
$\boldsymbol{W}_u(U_{gen})$	0	-
$\boldsymbol{W}_u(v_F)$	0	-
$\boldsymbol{W}_x(h_G)$	1	$(1/\text{mm})^2$
$\boldsymbol{W}_x(V_{vi})$	0.1	$(1/\text{mm}^3)^2$
$\boldsymbol{W}_s(h_G)$	0	$(1/\text{mm})^2$
$\boldsymbol{W}_s(V_{vi})$	0	$(1/\text{mm}^3)^2$

Table A.14.: NMPC parameters for regulating the thin neck (approach 2)

segment	U_{gen}		v_F	
1	0 - 15 s	piecewise linear	0 - 30 s	piecewise constant
2	15 - 30 s	piecewise linear		

Table A.15.: Control points for regulating the thin neck (approach 2)

A.7.4. Cone Growth (Using Feedforward Component)

Parameter	Values	Unit
Loop time	2	s
H_p	50	s
H_u	50	s
$\Delta U_{gen,lb}$	0	kV/min
$\Delta U_{gen,ub}$	$+0.2$	kV/min
$\Delta v_{F,lb}$	-0.3	mm/min^2
$\Delta v_{F,ub}$	$+0.3$	mm/min^2
$\boldsymbol{W}_u(U_{gen})$	1000	$(1/\text{kV})^2$
$\boldsymbol{W}_u(v_F)$	500	$(\text{min/mm})^2$
$\boldsymbol{W}_x(\varphi_C)$	0.001	$(1/^\circ)^2$
$\boldsymbol{W}_s(\varphi_C)$	0	$(1/^\circ)^2$

Table A.16.: NMPC parameters for regulating the crystal cone

segment	U_{gen}		v_F	
1	0 - 25 s	piecewise linear	0 - 15 s	piecewise linear
2	25 - 50 s	piecewise linear		

Table A.17.: Control points for regulating the crystal cone. v_F is calculated based on the stationary mass balance. It is involved in the model prediction as piecewise linear evolution from the current value to the calculated one considering the lower (lb) and upper (ub) limits of the slope.

A.7.5. Cone Growth (Full Regulation)

Parameter	Values	Unit
Loop time	5	s
H_p	240	s
H_u	240	s
$\Delta U_{gen,lb}$	0	kV/min
$\Delta U_{gen,ub}$	+0.14	kV/min
$\Delta v_{F,lb}$	−0.05	mm/min^2
$\Delta v_{F,ub}$	+0.1	mm/min^2
$\boldsymbol{W}_u(U_{gen})$	0	(1/kV)^2
$\boldsymbol{W}_u(v_F)$	0	(min/mm)^2
$\boldsymbol{W}_x(\varphi_C)$	1	(1/°)^2
$\boldsymbol{W}_x(h_G)$	2	(1/mm)^2
$\boldsymbol{W}_s(\varphi_C)$	0	(1/°)^2
$\boldsymbol{W}_s(h_G)$	0.5	(1/mm)^2

Table A.18.: NMPC parameters for regulating the crystal cone

segment	U_{gen}		v_F	
1	0 - 240 s	piecewise linear	0 - 240 s	piecewise linear

Table A.19.: Control points for regulating the crystal cone

A.7.6. Landing

Parameter	Values	Unit
Loop time	5	s
H_p	240	s
H_u	240	s
$\Delta U_{gen,lb}$	-0.06	kV/min
$\Delta U_{gen,ub}$	$+0.06$	kV/min
$\Delta v_{F,lb}$	-0.1	mm/min^2
$\Delta v_{F,ub}$	$+0.1$	mm/min^2
$\boldsymbol{W}_u(U_{gen})$	0	(1/kV)^2
$\boldsymbol{W}_u(v_F)$	0	(min/mm)^2
$\boldsymbol{W}_x(h_G)$	2	(1/mm)^2
$\boldsymbol{W}_s(h_G)$	0.5	(1/mm)^2

Table A.20.: NMPC parameters for regulating the crystal cone

segment	U_{gen}		v_F	
1	0 - 240 s	piecewise linear	0 - 60 s	piecewise linear

Table A.21.: Control points for regulating the crystal cone. v_F is calculated based on the stationary mass balance. It is involved in the model prediction as piecewise linear evolution from the current value to the calculated one considering the lower (lb) and upper (ub) limits of the slope.

A.7.7. Crystal with 150 mm in Diameter

Parameter	Values	Unit
Loop time	4	s
H_p	240	s
H_u	240	s
$\boldsymbol{W}_u(U_{gen})$	0	-
$\boldsymbol{W}_u(v_F)$	0	-
$\boldsymbol{W}_x(D_C)$	1	$(1/\text{mm})^2$
$\boldsymbol{W}_x(h_G)$	1	$(1/\text{mm})^2$
$\boldsymbol{W}_s(D_C)$	0.2	$(1/\text{mm})^2$
$\boldsymbol{W}_s(h_G)$	0.2	$(1/\text{mm})^2$

Table A.22.: NMPC parameters for regulating the crystal with 150 mm in diameter

segment	U_{gen}		v_F	
1	0 - 90 s	piecewise linear	0 - 90 s	piecewise linear
2	90 - 240 s	piecewise linear	90 - 240 s	piecewise linear

Table A.23.: Control points for regulating the crystal with 150 mm in diameter

A.7.8. Avogadro Crystal

Parameter	Values	Unit
Loop time	4	s
H_p	240	s
H_u	240	s
$\boldsymbol{W}_u(U_{gen})$	0	-
$\boldsymbol{W}_u(v_F)$	0	-
$\boldsymbol{W}_x(D_C)$	1	$(1/\text{mm})^2$
$\boldsymbol{W}_x(h_G)$	1	$(1/\text{mm})^2$
$\boldsymbol{W}_s(D_C)$	0.2	$(1/\text{mm})^2$
$\boldsymbol{W}_s(h_G)$	0.2	$(1/\text{mm})^2$

Table A.24.: NMPC parameters for regulating the Avogadro crystal

segment	U_{gen}		v_F	
1	0 - 150 s	piecewise linear	0 - 150 s	piecewise linear
2	150 - 240 s	piecewise linear	150 - 240 s	piecewise linear

Table A.25.: Control points for regulating the Avogadro crystal

Bibliography

[Abr02] N. V. Abrosimov, A. Lüdge, H. Riemann and W. Schröder. Lateral photovoltage scanning (LPS) method for the visualization of the solid-liquid interface of Si(1-x)Ge(x) single crystals. Journal of Crystal Growth 237-239, 356–360 (2002).

[Ale75] V. Alex. Poster, Leibnitz Institute for Crystal Growth, 1975.

[Bec09] P. Becker, H. Friedrich, K. Fujii, W. Giardini, G. Mana, A. Picard, H.-J. Pohl, H. Riemann and S. Valkiers. The Avogadro constant determination via enriched silicon-28. Measurement Science and Technology 20, 092002 (20pp) (2009).

[Bec13] P. Becker and D. Schiel. The Avogadro constant and a new definition of the kilogram. International Journal of Mass Spectrometry 349-350, 219–226 (2013).

[Bil55] E. Billig. Growth of Monocrystals of Germanium from an Undercooled Melt. Proceedings of the Royal Society of London Series A 229, 346–363 (1955).

[Boh94] J. Bohm, A. Lüdge and W. Schröder. Handbook of crystal growth, vol. 2A. Bulk Crystal Growth. (North-Holland, Amsterdam [u.a.], 1994).

[Bor07] M. Borys, M. Gläser and M. Mecke. Mass determination of silicon spheres used for the Avogadro project. Measurement 40, 785–790 (2007).

[Cor77] S. R. Coriell and M. R. Cordes. Theory of molten zone shape and stability. Journal of Crystal Growth 42, 466–472 (1977).

[Das59] W. C. Dash. Growth of Silicon Crystals Free from Dislocations. Journal of Applied Physics 30, 459–474 (1959).

[Dor96] E. Dornberger, W. von Ammon, H. Ölkrug and F. Wasmeier. Verfahren und Vorrichtung zur Steuerung des Kristallwachstums. DE Patent 696 01 424 T2, 1996. Wacker Siltronic Gesellschaft für Halbleitermaterialien AG, Burghausen, Germany.

[Dor97] E. Dornberger, W. von Ammon, H. Ölkrug and F. Wasmeier. Process for controlling the growth of a crystal. US Patent 5,868,831, 1997. Wacker Siltronic Gesellschaft für Halbleitermaterialien AG, Burghausen, Germany.

[Duf10] T. Duffar. Crystal Growth Processes Based on Capillarity: Czochralski, Floating Zone, Shaping and Crucible Techniques. (Wiley-Blackwell, 2010).

[Fin02] R. Findeisen and F. Allgöwer. An Introduction to Nonlinear Model Predictive. In Control, 21st Benelux Meeting on Systems and Control, Veidhoven, 1–23, 2002.

[Hei04] T. Heine. Modellgestützte Überwachung und Führung von Fed-Batch-Prozessen zur Antibiotikaproduktion. Fortschritt-Berichte VDI: Reihe 8, Mess-, Steuerungs- und Regelungstechnik. (VDI-Verlag, 2004).

[Hey56] W. Heywang. Zur Stabilität senkrechter Schmelzzonen. Zeitschrift für Naturforscher 11a, 238–243 (1956).

[Hur94] D. J. T. Hurle. Handbook of crystal growth, vol. 2A. (Amsterdam Lausanne New York Elsevier, 1994).

[Ike87] Y. Ikeda, N. Ohara, K. Suzuki and M. Watanabe. Method of and Apparaturus for Controlling Floating Zone of Semiconductor Rod. US Patent 4,866,230, 1987. Shin-Etu Handotai Co. Ltd, Tokio, Japan.

[Kal60] R. E. Kalman. A New Approach to Linear Filtering and Prediction Problems. Transactions of the ASME–Journal of Basic Engineering 82, 35–45 (1960).

[Lan87] L. D. Landau and E. M. Lifshitz. Fluid Mechanics, Second Edition: Volume 6 (Course of Theoretical Physics). Course of theoretical physics / by L. D. Landau and E. M. Lifshitz, Vol. 6. (Butterworth-Heinemann, 2 edition, Januar 1987).

[Lan12] A. Lange. Anwendung einer nichtlinearen modellprädiktiven Mehrgrößenregelung auf die Floating Zone (FZ) Kristallzüchtung, 2012. Unpublished Master‘s thesis, Technische Universität Berlin, Supervised by R. King and N. Werner.

[Lüd97] A. Lüdge and H. Riemann. Doping Inhomogeneities in Silicon Crystals Detected by the Lateral Photovoltage Scanning (LPS) Method. Institut of Physics - Conference Series 160, 145–148 (1997).

[Lüd02] A. Lüdge, H. Riemann, B. Hallmann-Seifert, M. Renner, H. Wawra, L. Jensen, T. L. Larsen and A. Nielsen. High-Speed Growth of FZ Silicon for Photovoltaics. In 202nd Fall Meeting of the Electrochemical Society, number 598, 2002.

[Lüd10] A. Lüdge, H. Riemann, M. Wünscher, G. Behr, W. Löser and A. Muiznieks. Crystal Growth Processes Based on Capillarity: Czochralski, Floating Zone, Shaping and Crucible Techniques, chapter Floating Zone Crystal Growth, 203–276. (Wiley-Blackwell, 2010).

[Lev59] J. Levinson. Temperature control for crystal pulling, US Patent 2,908,004, 1959.

[Lue64] D.G. Luenberger. Observing the State of a Linear System. Military Electronics, IEEE Transactions on 8, 74–80 (1964).

[Mac02] J. M. Maciejowski. Predictive control with constraints. (Prentice Hall, Essex, England, 2002).

[Mah03] R. Mahadevan and F. J. Doyle III. Efficient optimization approaches to nonlinear model predictive control. International Journal of Robust and Nonlinear Control 13, 309–329 (2003).

[Men12] R. Menzel. Growth Conditions for Large Diameter FZ Si Single Crystals. PhD thesis, Technische Universität Berlin, 2012.

[Neu12] M. Neubert and J. Winkler. Nonlinear model-based control of the Czochralski process III: Proper choice of manipulated variables and controller parameter scheduling. Journal of Crystal Growth 360, 3–11 (2012).

[Rat07] G. Ratnieks. Modelling of the Floating Zone Growth of Silicon Single Crystals with Diameter up to 8 Inch. PhD thesis, Univerity of Latvia, 2007.

[Rie09] H. Riemann and A. Lüdge. Crystal Growth of Si for Solar Cells, chapter Floating Zone Crystal Growth, 41–53. (Springer, 2009).

[Ros12] H.-J. Rost, A. Lüdge, H. Riemann, F. Kirscht and F.-W. Schulze. Float zone (FZ) silicon: A potential material for advanced commercial solar cells? Crystal Research and Technology 47, 273–278 (2012).

[Sat10] G. A. Satunkin. Modelling the dynamics and control design for Czochralski, Liquid Encapsulated Czochralski and Floating Zone processes. Progress in Crystal Growth and Characterization of Materials 56, 1–121 (2010).

[Shi10] F. Y. Shih. Image Processing and Pattern Recognition: Fundamentals and Techniques. (Wiley, 2010).

[Sim06] D. Simon. Optimal State Estimation: Kalman, H Infinity, and Nonlinear Approaches. (Wiley-Interscience, 1 edition, August 2006).

[Tag88] K. Taguchi and M. Watanabe. Method of Controlling Floating Zone. US Patent 4,931,945, 1988. Shin-Etu Handotai Co. Ltd, Tokio, Japan.

[Thi11] E. Thiele. Application of the extended Kalman filter to data of the crucible-free floating zone process of silicon, 2011. Unpublished Bachelors‘s thesis, Technische Universität Berlin, Supervised by R. King and N. Werner.

[Vuk13] H. Vukman. Automatic generation of specified start conditions for the floating zone technique, 2013. Unpublished Bachelors's thesis, Technische Universität Berlin, Supervised by R. King and N. Werner.

[Wäc02] A. Wächter. An Interior Point Algorithm for Large-Scale Nonlinear Optimization with Applications in Process Engineering. PhD thesis, Carnegie Mellon University, January 2002.

[Wäc06] A. Wächter and L. T. Biegler. On the implementation of an interior-point filter line-search algorithm for large-scale nonlinear programming. Mathematical Programming 106, 25–57 (2006).

[Wat88] M. Watanabe, N. Ohhara and K. Taguchi. Control of the Power to the Heater and the Speed of Movement of a Crystal Rod by Control of the Crystal Rod Diameter. US Patent 4,876,438, 1988. Shin-Etu Handotai Co. Ltd, Tokio, Japan.

[Wel97] G. Welch and G. Bishop. An Introduction to the Kalman Filter. 1997. Updated July 24, 2006. Accessed February 28, 2013, URL `http://www.cs.unc.edu/~{}welch/kalman/kalmanIntro.html`.

[Wer12] N. Werner and M. Wünscher. Modellprädiktive Regelung des Zonenschmelz-Verfahrens, DE Patentanmeldung 10 2012 108 009.7, 2012.

[Wil88] K.-Th. Wilke. Kristallzüchtung. (VEB Deutscher Verlag der Wissenschaften, 1988).

[Win10a] J. Winkler, M. Neubert and J. Rudolph. Nonlinear model-based control of the Czochralski process I: Motivation, modeling and feedback controller design. Journal of Crystal Growth 312, 1005–1018 (2010).

[Win10b] J. Winkler, M. Neubert and J. Rudolph. Nonlinear model-based control of the Czochralski process II: Reconstruction of crystal radius and growth rate from the weighing signal. Journal of Crystal Growth 312, 1019–1028 (2010).

[Wün11a] M. Wünscher. Crucible-free Crystal Growth of Germanium - Experiments and Simulations. PhD thesis, Technische Universität Berlin, 2011.

[Wün11b] M. Wünscher, A. Lüdge and H. Riemann. Crucible-free pulling of germanium crystals. Journal of Crystal Growth 318, 1039–1042 (2011).

[Wün11c] M. Wünscher, A. Lüdge and H. Riemann. Growth angle and melt meniscus of the RF-heated floating zone in silicon crystal growth. Journal of Crystal Growth 314, 43–47 (2011).

[Zha01a] J. Zhao, A. Wang and M. A. Green. 24.5% efficiency PERT silicon solar cells on SEH MCZ substrates and cell performance on other SEH CZ and FZ substrates. Solar Energy Materials and Solar Cells 66, 27–36 (2001).

[Zha01b] J. Zhao, A. Wang and M. A. Green. High-efficiency PERL and PERT silicon solar cells on FZ and MCZ substrates. Solar Energy Materials and Solar Cells 65, 429–435 (2001).

[Zio98] D. Ziou and S. Tabbone. Edge Detection Techniques - An Overview. International Journal of Pattern Recognition and Image Analysis 8, 537–559 (1998).

[Zul00] W. Zulehner. Historical overview of silicon crystal pulling development. Materials Science and Engineering: B 73, 7–15 (2000).

Published work

The here presented concept of Floating Zone process control was registered for patent in the year 2012 by the Leibniz Institute of Crystal Growth [Wer12].

Supervised Work

Within the scope of this dissertation the following master's and bachelors's theses are supervised:

- Application of the extended Kalman filter to data of the crucible-free floating zone process of silicon (Bachelors's thesis. Technische Universität Berlin) [Thi11].
- Anwendung einer nichtlinearen modellprädiktiven Mehrgrößenregelung auf die Floating Zone (FZ) Kristallzüchtung (Masters's thesis. Technische Universität Berlin) [Lan12].
- Automatic generation of specified start conditions for the floating zone technique (Bachelors's thesis. Technische Universität Berlin) [Vuk13].